TUDelft

Delft University of Technology

To the root of vegetation-water interactions
Improving spatiotemporal variations in global models

van Oorschot, F.

DOI
Publication date
2024
Document Version
Final published version

Citation (APA)

Important note
To cite this publication, please use the final published version (if applicable).
Please check the document version above.

TO THE ROOT OF VEGETATION-WATER INTERACTIONS

IMPROVING SPATIOTEMPORAL VARIATIONS IN GLOBAL MODELS

TO THE ROOT OF VEGETATION-WATER INTERACTIONS

IMPROVING SPATIOTEMPORAL VARIATIONS IN GLOBAL MODELS

Dissertation

for the purpose of obtaining the degree of doctor
at Delft University of Technology
by the authority of the Rector Magnificus prof. dr. ir. T. H. J. J. van der Hagen,
chair of the Board for Doctorates
to be defended publicly on
Wednesday 13 November 2024 at 12:30

by

Fransje VAN OORSCHOT

Master of Science in Civil Engineering,
Delft University of Technology, Delft, the Netherlands,
born in Roosendaal, the Netherlands.

This dissertation has been approved by the promotors.

Composition of the doctoral committee:

Rector Magnificus	chairperson
Dr. M. Hrachowitz	Delft University of Technology, promotor
Dr. ir. R. J. van der Ent	Delft University of Technology, copromotor

Independent members:

Dr. ir. I. E. M. de Graaf	Wageningen University and Research
Prof. dr. A. Kleidon	Max Planck Institute for Biogeochemistry
Prof. dr. ir. S. C. Steele-Dunne	Delft University of Technology
Prof. dr. ir. R. Uijlenhoet	Delft University of Technology

Other members:

Dr. A. Alessandri	National Research Council of Italy, supervisor (external)

Dr. A. Alessandri has contributed to the preparation of this dissertation.

Per fare tutto ci vuole un fiore

Sergio Endrigo

Contents

1

INTRODUCTION

This chapter is based on:

van Oorschot, F., van der Ent, R. J., Hrachowitz, M., and Alessandri, A.: *Climate-controlled root zone parameters show potential to improve water flux simulations by land surface models*, Earth Syst. Dynam., 12, 725–743, 2021.

van Oorschot, F., van der Ent, R. J., Hrachowitz, M., Di Carlo, E., Catalano, F., Boussetta, S., Balsamo, G., and Alessandri, A.: *Interannual land cover and vegetation variability based on remote sensing data in the HTESSEL land surface model: implementation and effects on simulated water dynamics*, Earth Syst. Dynam., 14, 1239–1259, 2023.

van Oorschot, F., van der Ent, R. J., and Alessandri, A., Hrachowitz, M.: *Influence of irrigation on root zone storage capacity estimation*, Hydrol. Earth Syst. Sci., 28, 2313–2328, 2024.

van Oorschot, F., Hrachowitz, M., Viering, T., Alessandri, A., and van der Ent, R. J.: *Global patterns in vegetation accessible subsurface water storage emerge from spatially varying importance of individual drivers*, Environmental Research Letters, in review.

1

1.1 VEGETATION AND THE WATER CYCLE

Vegetation takes many shapes around the world, ranging from needleleaf forests and temperate deciduous forests, to savannas and tropical rainforests. Across the seasons, vegetation plays a key role in the water cycle, which involves the natural movement of water between the Earth's atmosphere, surface, and subsurface. Vegetation influences the water cycle by regulating the partitioning of precipitation into runoff and evaporation (Seneviratne et al., 2010). Simultaneously, vegetation also influences the energy cycle through the associated latent heat fluxes. Evaporation from land can be subdivided into interception evaporation from surfaces such as vegetation leaves, soil evaporation, and transpiration. From these three fluxes, transpiration, the process by which vegetation transports water from the subsurface through root water uptake to the atmosphere through evaporation from leaves' stomata, is on average the largest (Miralles et al., 2011; Schlesinger and Jasechko, 2014; Wei et al., 2017; Nelson et al., 2020). The amount of evaporation from an ecosystem is influenced by climatic factors such as precipitation, radiation and humidity, and by the physical characteristics (both aboveground and belowground) of the vegetation (e.g., Teuling et al., 2009; Zhang et al., 2017). Given vegetation's adaptability to prevailing climate and landscape characteristics (Fan et al., 2017), its appearance is dynamic across spatial (local, regional, and global) and temporal (seasonal, interannual, and decadal) scales (e.g., Kleidon, 2004; Méndez-Barroso et al., 2009; Pan et al., 2018; Holsinger et al., 2019).

1.2 VEGETATION IN LARGE SCALE MODELS

Considering its essential role in the Earth's water cycle, vegetation is a key component of large scale (i.e., regional to global) hydrological models and land surface models (LSMs), which represent the land component in models used for climate reanalyses and climate projections. In these models, the representations of both the aboveground and belowground vegetation characteristics determine the quantity and timing of modeled water and energy fluxes over land.

Information on aboveground vegetation characteristics, such as the type of vegetation, the amount of leaves in the canopy, or the greenness of the vegetation, is needed for modelling evaporation. However, direct in-situ observations of such properties are not straightforward and, if available, not representative for large scales. Therefore, satellite remote sensing data have been widely used in LSMs to represent the spatial and temporal variability of vegetation characteristics (Balsamo et al., 2018). For example, global satellite-derived maps of land cover and albedo have been directly used as boundary conditions in LSMs (Faroux et al., 2013; Alessandri et al., 2017; Boussetta et al., 2021). In addition, the spatial and temporal dynamics of leaf area index (LAI), which is a measure for the amount of leaf area of vegetation relative to the covered ground area, derived from satellite remote sensing have been assimilated in several LSMs for different spatial scales, generally leading to improved water, energy, and carbon fluxes (Albergel et al., 2017, 2018; Kumar et al., 2019; Ling et al., 2019; Rahman et al., 2020, 2022). Although remote sensing based vegetation characteristics have been extensively used in large scale models, the effects of the model representation of interannual variability of aboveground vegetation characteristics on the water cycle has remained understudied.

Besides the aboveground appearance of vegetation, belowground roots also regulate evaporation by facilitating transpiration through subsurface water uptake. The vegetation root zone is defined as the part of the subsurface where vegetation has developed roots and is characterized by parameters such as root depth and root density. Root zone characteristics vary across different regions and change over time, because vegetation shapes its roots in a way to provide both anchoring in the subsurface (Read and Stokes, 2006), as well as access to sufficient nutrients and water (Zhang et al., 2019; Oldroyd and Leyser, 2020; Maan et al., 2023). The importance of the root zone in hydrological and land surface modeling is widely acknowledged, with multiple studies highlighting the sensitivity of these models to the representation of the vegetation's root zone (Mahfouf et al., 1996; Desborough, 1997; de Rosnay and Polcher, 1998; Norby and Jackson, 2000; Feddes et al., 2001; Teuling et al., 2006a,b). However, direct observations of root zone characteristics at large scales (i.e., beyond lab-scale or individual plants) do not exist.

LSMs generally describe root zone characteristics (e.g., root depth, root density and root distribution) for different vegetation classes combined with soil type information and a model-dependent fixed soil depth. The generally shallow (< 2 m) (Pan et al., 2020) fixed soil depth limits the size of the model root zone representation and, as a consequence, also the moisture extraction by roots from deep soil layers (Kleidon and Heimann, 1998; Sakschewski et al., 2020). LSMs use lookup tables that prescribe the same root zone parameters worldwide for each combination of vegetation and soil class as obtained from a very limited number of point-scale observations of rooting structure (Canadell et al., 1996; Jackson et al., 1996; Zeng et al., 1998; Schenk and Jackson, 2002a,b). The spatial distribution of the root zone parameterization in LSMs is obtained by combining these lookup table values with maps of vegetation cover and soil texture. The limitations of this approach are as follows: the root observations (1) are uncertain due to the fact that they mostly vertically extrapolate root measurements while excavating only the first meter or less (Schenk and Jackson, 2002a,b); (2) do not adequately represent global distributions of root structures because observations are extremely scarce – e.g., the global Schenk and Jackson (2002b) dataset includes only 475 root profiles in 209 geographical locations; (3) are observations of individual plants that do not represent spatial variations in ecosystem composition at larger scales than the plot scale; and (4) are snapshots in time and, therefore, do not represent their evolution over time due to continuous adaptation of ecosystems to changing environmental conditions.

Alternative approaches for describing the vegetation's root zone on a large scale adopt a holistic perspective on ecosystems instead of the lookup tables based on point-scale root observations. These approaches address the challenge posed by the absence of direct observations of root characteristics at scales larger than plot scale. Instead, they focus on indirectly estimating root characteristics from observable ecosystem properties that are available at the scale of interest using optimality principles (Kleidon, 2004; Gao et al., 2014; Speich et al., 2018; Dralle et al., 2020a). These approaches are based on the evidence that the extent of vegetation root systems is primarily controlled by climate conditions, as vegetation tends to optimize its aboveground and belowground carbon investment in order to optimally function by avoiding water shortages and maintaining transpiration and productivity (Kleidon and Heimann, 1998; Collins and Bras, 2007; Guswa, 2008; Sivandran and Bras, 2013; Gao et al., 2014; De Boer-Euser et al., 2016; Kup-

pel et al., 2017; Singh et al., 2020).

Overall, the identified research gap is that the spatial and temporal variability of aboveground and belowground vegetation are not adequately captured in large scale (i.e., regional to global) hydrological models and land surface models. This limitation results in deficiencies in accurately modeling the variability of surface water and energy states and fluxes (e.g., Pitman, 2003; Seneviratne et al., 2006; Alessandri et al., 2007; Ukkola et al., 2016; Wartenburger et al., 2018; Gharari et al., 2019; Fisher and Koven, 2020; Hersbach et al., 2020). Consequently, it introduces uncertainties in predicting the global water budget and hydrological extremes such as droughts and floods (Brunner et al., 2021). Hence, it is essential to improve vegetation representation in large scale models, especially considering ongoing climate change and land-use changes.

1.3 THIS THESIS

This thesis addresses the limited spatial and temporal variability of both aboveground and belowground vegetation in large scale (i.e., regional to global) hydrological models and land surface models. The objective of this doctoral research is to develop more realistic model representations of spatial and temporal vegetation variability, and explore their potential for improving modeled water fluxes in these models. To achieve this objective, we use readily available data suitable to use at large scales (~5 to 100 km) to represent both aboveground and belowground vegetation variability. Specifically, we apply remote sensing data for representing aboveground vegetation, and we adopt a holistic, climate-controlled, approach for representing belowground vegetation. The effects of these developments are then evaluated through model simulations and comparison with observations and other modeling approaches.

This thesis is structured as follows: in Chapter 2, we integrate interannual variability of aboveground vegetation characteristics derived from remote sensing data in the Hydrology Tiled ECMWF Scheme for Surface Exchanges over Land (HTESSEL) land surface model, and evaluate the effects on modeled hydrology. Chapters 3-5 focus on belowground vegetation characteristics. In these chapters we use the concept of root zone storage capacity (S_r), which represents the hydrologically relevant magnitude of the vegetation's root zone. S_r (mm) is defined as the maximum subsurface moisture volume per unit area of subsurface moisture that is accessible to roots of vegetation for uptake (Gao et al., 2014). It is important to note that S_r is not necessarily proportional to the depth of roots. While root depth only describes the vertical root profile, S_r also accounts for lateral root extent and root density. For example, an ecosystem covered by deep-rooting vegetation with roots with low density likely has a smaller S_r than one covered by vegetation with shallow, high-density roots (Singh et al., 2020). Chapter 3 represents an explorative study on integrating a climate-controlled representation of S_r in the HTESSEL model at regional scale, and evaluating its effects on modeled water fluxes. In Chapter 4 we quantify the influence of irrigation on the estimation of root zone storage capacity in a global context. In Chapter 5 we explore the spatial variability of the influence of climatic, vegetation, and landscape characteristics on the magnitude of S_r globally, and based on these findings, we create a global estimate of S_r. Finally, Chapter 6 presents a synthesis of the main findings of this research on vegetation variability in large-scale models, including insights and implications, and an outlook for future research.

2

INTERANNUAL ABOVEGROUND VEGETATION VARIABILITY IN THE HTESSEL LAND SURFACE MODEL

Land surface models require information on aboveground characteristics of vegetation such as land cover type and leaf area index. Here we integrated interannual variability of vegetation characteristics based on remote sensing data into a land surface model, and we evaluated the effects on simulated water dynamics.

SUMMARY

Vegetation largely controls land surface–atmosphere interactions. Although vegetation is highly dynamic across spatial and temporal scales, most land surface models currently used for reanalyses and near-term climate predictions do not adequately represent these dynamics. This causes deficiencies in the variability of modeled water and energy states and fluxes from the land surface. In this study we evaluated the effects of integrating spatially and temporally varying land cover and vegetation characteristics derived from satellite observations on modeled evaporation and soil moisture in the Hydrology Tiled ECMWF Scheme for Surface Exchanges over Land (HTESSEL) land surface model. Specifically, we integrated interannually varying land cover from the European Space Agency Climate Change Initiative and interannually varying leaf area index (LAI) from the Copernicus Global Land Services (CGLS). Additionally, satellite data on the fraction of green vegetation cover (FCover) from CGLS were used to formulate and integrate a spatially and temporally varying effective vegetation cover parameterization. The effects of these three implementations on model evaporation fluxes and soil moisture were analyzed using historical offline (land-only) model experiments at the global scale, and model performances were quantified with global observational products of evaporation (E) and near-surface soil moisture (SM_s). The interannually varying land cover consistently altered the evaporation and soil moisture in regions with major land cover changes. The interannually varying LAI considerably improved the correlation of SM_s and E with respect to the reference data, with the largest improvements in semiarid regions with predominantly low vegetation during the dry season. These improvements are related to the activation of soil moisture–evaporation feedbacks during vegetation-water-stressed periods with interannually varying LAI in combination with interannually varying effective vegetation cover, defined as an exponential function of LAI. The further improved effective vegetation cover parameterization consistently reduced the errors of model effective vegetation cover, and it regionally improved SM_s and E. Overall, our study demonstrated that the enhanced vegetation variability consistently improved the near-surface soil moisture and evaporation variability, but the availability of reliable global observational data remains a limitation for complete understanding of the model response. To further explain the improvements found, we developed an interpretation framework for how the model development activates feedbacks between soil moisture, vegetation, and evaporation during vegetation water stress periods.

2.1 INTRODUCTION

Interactions between the land surface and the atmosphere in terms of water and energy are largely dependent on vegetation. To improve model representations of vegetation variability, and as a consequence, the modeled water dynamics, datasets representing aboveground vegetation characteristics based on satellite remote sensing data have been widely used in land surface models (LSMs) (Chapter 1). Recent studies have exploited the latest satellite campaigns to update land cover (LC) and leaf area index (LAI) representation into the land surface model Carbon-Hydrology ECMWF Tiled Scheme for Surface Exchanges over Land (CHTESSEL) (Johannsen et al., 2019; Nogueira et al., 2020, 2021; Boussetta et al., 2021) as part of the Integrated Forecasting System (IFS) of the European Centre for Medium-Range Weather Forecasts (ECMWF). These studies replaced the original fixed map of land cover from the Global Land Cover Characteristics (GLCC) dataset representing the early 1990s (Loveland et al., 2000) with an updated map obtained from the latest-generation estimates of land cover from the European Space Agency Climate Change Initiative (ESA-CCI) (Poulter et al., 2015). Similarly, the LAI climatology from the Moderate Resolution Imaging Spectroradiometer (MODIS) (Boussetta et al., 2013) was replaced with updated climatology from the recent Copernicus Global Land Service (CGLS) LAI dataset (Verger et al., 2014). The integration of these satellite-derived variables considerably reduced the bias of model land surface temperatures (Johannsen et al., 2019; Nogueira et al., 2020, 2021). In addition, Boussetta et al. (2021) showed an overall reduction of model annual mean evaporation bias when using the updated LC and LAI in CHTESSEL.

LAI in LSMs can be coupled to the effective vegetation cover (C_{eff}), which characterizes the density of the vegetated surface from a top view that effectively contributes to the water and energy balances. The organization structure of leaves inside the canopy is reported as vegetation clumping. In previous modeling studies, the seasonal variations in C_{eff} have been described as an exponential function of LAI considering vegetation clumping in (C)HTESSEL (Alessandri et al., 2017; Nogueira et al., 2020; Boussetta et al., 2021) and in other land modeling efforts (Anderson et al., 2005; Krinner et al., 2005; Le Moigne, 2012). The shape of the exponential relation between C_{eff} and LAI in state-of-the-art land surface models has, to our knowledge, been assumed to be constant in time and space so far (Krinner et al., 2005; Alessandri et al., 2017; Nogueira et al., 2020; Boussetta et al., 2021). However, studies have shown that the degree of vegetation clumping, and therefore the shape of this relation, actually varies for different vegetation types (Chen et al., 2005; Ryu et al., 2010; Zhang et al., 2014).

The research gap that we identified is that most previous LSM studies using HTESSEL aimed at improving the temporally fixed boundary condition of land cover and the monthly seasonal cycle of LAI, while not exploring the effects of interannual variations of LC and LAI. Moreover, these studies have generally used one spatially fixed relationship between effective vegetation cover and LAI, while there is considerable evidence that this relationship is vegetation-type-dependent (Chen et al., 2005; Ryu et al., 2010; Zhang et al., 2014).

The objective of this research is to evaluate the effects of integrating temporal and spatial variations of land cover and vegetation characteristics derived from satellite observations on modeled evaporation and soil moisture in the land surface model HTES-

SEL. Specifically, we will integrate annually varying LC from ESA-CCI as well as season-ally and interannually varying LAI from CGLS. Additionally, the CGLS fraction of green vegetation cover (FCover; Verger et al., 2014) is used to formulate and implement a spatially (i.e., vegetation-dependent) and temporally (i.e., interannually) variable effective vegetation cover parameterization in HTESSEL.

2.2 Methods

This section describes how we integrated temporal and spatial variations of land cover and vegetation characteristics in HTESSEL. In Sect. 2.2.1 we describe the land cover and vegetation data used, in Sect. 2.2.2 we describe the model characteristics with relevance to water dynamics, and in Sect. 2.2.3 the model developments performed in this study are reported. Finally, the model experiments and model evaluation are described in Sect. 2.2.4 and Sect. 2.2.5, respectively.

2.2.1 Land cover and vegetation data

Here we used yearly land cover maps at a 300 m spatial resolution from ESA-CCI for the time period 1993–2019 (Defourny et al., 2017; Copernicus Climate Change Service, 2019). In this dataset the land cover is classified into 22 classes based on the United Nations Land Cover Classification System (LCCS) (Di Gregorio and Jansen, 2005).

LAI and FCover data were obtained from CGLS for 1999–2019 (Copernicus Global Land Service, 2022). We used the 1 km version 2 collection in which both products were derived at a 10-daily resolution from the top-of-canopy reflectance measurements by the SPOT/VEGETATION (1999–2013) and PROBA-V (2014–2019) sensors (Verger et al., 2019). These two time series were homogenized using a cumulative distribution function (CDF) approach following Boussetta and Balsamo (2021). For model spin-up purposes, the CGLS LAI (1999–2019) was further extended backwards with former-generation LAI data from the Advanced Very-High-Resolution Radiometer (AVHRR) for 1993–1999 at a 0.05° resolution (Pacholczyk and Verger, 2020). The AVHRR LAI (1993–1999) was interpolated using conservative interpolation (Schulzweida, 2022) to the CGLS 1 km resolution and harmonized with CGLS (1999–2019) using CDF matching (Boussetta and Balsamo, 2021).

2.2.2 Relevant model components for water cycle representation

Here we used the HTESSEL land surface model (Balsamo et al., 2009) as it was developed and implemented for climate predictions with the EC-Earth3 Earth system model (Döscher et al., 2022). This version already implements a temporally, but not spatially, varying effective vegetation cover, which is further developed in this work (Alessandri et al., 2017). This section describes the relevant model representations of land cover (Sect. 2.2.2), leaf area index (Sect. 2.2.2), and effective vegetation cover (Sect. 2.2.2) in the current HTESSEL version as part of the EC-Earth3 Earth system model (ESM) and the role of these representations in the modeled water cycle. Section 2.2.3 describes the adaptations of these model components made in this study.
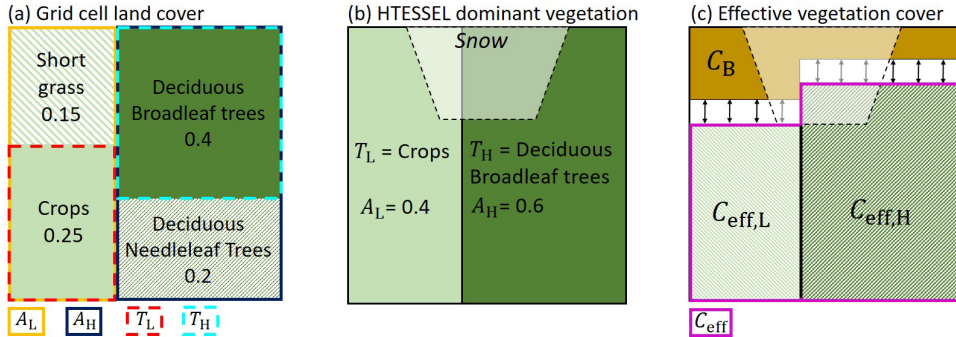
Figure 2.1: Vegetation representation in a grid cell with example vegetation types and cover fractions. **(a)** Grid cell vegetation type and cover fraction based on land cover dataset. **(b)** HTESSEL dominant low- and high-vegetation type (T_L and T_H) and cover fraction (A_L and A_H). **(c)** HTESSEL effective vegetation cover with $C_{eff,L}$ and $C_{eff,H}$ being the effective low- and high-vegetation cover fraction, C_B the bare soil fraction, and $C_{eff} = C_{eff,L} + C_{eff,H}$, with the arrows indicating the temporal variability of C_{eff} as discussed in Sect. 2.2.2.

LAND COVER REPRESENTATION

In HTESSEL the vegetated area of a grid cell is divided into high- and low-vegetation tiles. In the case of snow there are separate model tiles for snow on bare ground with low vegetation and snow beneath high vegetation (Balsamo et al., 2009). Figure 2.1a represents an example of the vegetation types and cover fractions for a single grid cell that were originally based on the GLCC land cover dataset (Loveland et al., 2000). The low-vegetation (L) and high-vegetation (H) types with the largest cover fraction in each grid cell (see example in Fig. 2.1a) are used in HTESSEL as dominant vegetation types T_L and T_H (Fig. 2.1b). The corresponding HTESSEL vegetation cover fractions A_L and A_H are based on the total low- and high-vegetation grid cell cover fractions.

T_L and T_H directly control surface water and energy fluxes because model parameters such as vegetation root distribution, minimum canopy resistance, and roughness lengths for momentum and heat are obtained from lookup tables based on the vegetation type (ECMWF, 2016). Surface fluxes are calculated separately for low- and high-vegetation tiles and combined based on the fractions A_L and A_H. Here we only focus on the surface evaporation flux that we define as the sum of transpiration, soil evaporation, interception evaporation, and, in the case of lakes, also open-water evaporation (Savenije, 2004; Miralles et al., 2020). The subsurface in HTESSEL consists of four soil layers with thicknesses of 7, 21, 72, and 189 cm, totaling a depth of 289 cm. In this study we differentiate between near-surface soil moisture (SM_s) in the top layer (0–7 cm) and the subsurface soil moisture (SM_{sb}) in the three deeper layers (7–289 cm).

LEAF AREA INDEX REPRESENTATION

LAI is defined separately for the high- and low-vegetation tiles (LAI_L and LAI_H). In the original HTESSEL model, LAI_L and LAI_H are prescribed as a seasonal cycle that is derived from a satellite-based climatology based on MODIS (Boussetta et al., 2013) and the vegetation cover fractions A_L and A_H. The LAI controls the canopy resistance r_c of the high-

and low-vegetation tiles through the following linear relation:

$$r_c = \frac{r_{s,min}}{LAI} f_1(R_s) f_2(D_a) f_3(\overline{SM}),$$

(2.1)

with $r_{s,min}$ being the prescribed vegetation-specific minimum canopy resistance that does not change in time and $f_1(R_s)$, $f_2(D_a)$, and $f_3(\overline{SM})$ being functions describing the dependencies on shortwave radiation (R_s), atmospheric water vapor deficit (D_a), and weighted average soil moisture based on the root distribution over the four soil layers ($\overline{SM}$), respectively. The effects of CO_2 changes on r_c are not explicitly taken into account in the present study. The root fractions are generally the largest in soil layers 2 and 3, and therefore transpiration mostly originates from the SM_{sb}. The transpiration is linearly related to r_c and atmospheric variables. Furthermore, the LAI controls the capacity of the model interception reservoir W_{1m} by

$$W_{1m} = W_{1max} \cdot (C_B + C_L \cdot LAI_L + C_H \cdot LAI_H),$$

(2.2)

with $W_{1max} = 0.0002$ m and C_B, C_L, and C_H being the fractions of bare soil, effective low vegetation, and effective high vegetation, respectively (Sect. 2.2.2). The interception evaporation per time step follows from the water content of the interception reservoir (calculated from precipitation), W_{1m}, and the potential evaporation.

EFFECTIVE VEGETATION COVER REPRESENTATION

The model effective low vegetation cover and high vegetation cover ($C_{eff,L}$ and $C_{eff,H}$) represent the part of the model vegetation cover fraction (A_L and A_H) that is actively contributing to the water balance through transpiration and interception evaporation (Fig. 2.1c). The fraction of the grid cell not covered by effective vegetation is treated as bare soil (C_B), where only soil evaporation takes place. Soil evaporation only occurs in the top soil layer (0–7 cm) and therefore originates only from SM_s. The model resistance to soil evaporation (r_{soil}) is described by

$$r_{soil} = r_{soil,min} f_3(SM_s),$$

(2.3)

with $r_{soil,min} = 50$ sm^{-1} and $f_3(SM_s)$ representing the dependency on the first layer soil moisture content. The effective vegetation cover fractions $C_{eff,L}$ and $C_{eff,H}$ as well as bare soil fraction C_B are described by

$$C_{eff,L} = c_{v,L} \cdot A_L,$$

(2.4)

$$C_{eff,H} = c_{v,H} \cdot A_H,$$

(2.5)

$$C_{eff} = C_{eff,L} + C_{eff,H},$$

(2.6)

$$C_B = 1 - C_{eff},$$

(2.7)

with $c_{v,L}$ and $c_{v,H}$ representing the low and high vegetation density. Originally, $c_{v,L}$ and $c_{v,H}$ were described by a lookup table with vegetation-specific values, allowing for spatial variation of the $C_{eff,L}$, $C_{eff,H}$, and C_B fractions. However, this approach does not represent temporal variations in vegetation density. To allow for temporal variability in C_{eff} (represented by the arrows in Fig. 2.1c), $c_{v,L}$ and $c_{v,H}$ were linked to the seasonal variability of

LAI by the following exponential relation (Alessandri et al., 2017):

$$c_{v,L} = 1 - e^{-k\,LAI_L}, \tag{2.8}$$

$$c_{v,H} = 1 - e^{-k\,LAI_H}, \tag{2.9}$$

with k being the canopy light extinction coefficient that represents the degree of vegetation clumping (Anderson et al., 2005). Previously k was generally set to constant values of 0.5 (Krinner et al., 2005; Alessandri et al., 2017) or 0.6 (Boussetta et al., 2021) for all vegetation types. As a consequence, the vegetation-dependent spatial variability in k was not accounted for.

2.2.3 MODEL DEVELOPMENTS

THE IMPLEMENTED LAND COVER VARIABILITY

Here we implemented the annually varying ESA-CCI land cover (LC) data for the 1993–2019 period (Sect. 2.2.1), as developed by Boussetta and Balsamo (2021), for the HTESSEL vegetation types and spatial resolution. For consistency with the other model adaptations and evaluations (Sect. 2.2.3, 2.2.3 and 2.2.5), our LC analyses were based on 1999–2018. The interannually varying LC from ESA-CCI introduced a change in T_L in 5 % and T_H in 4 % of the land grid cells between the first (1999) and the last (2018) year of the considered study period (Fig. 2.2). Figure 2.2c shows the fraction of land grid cells in which each vegetation type (dominant in 1999) is replaced by another type in 2018 (plain colors) and conversely how often each vegetation type replaces the 1999 dominant one in 2018 (hatched colors). The figure shows that crops and short grass relatively often replaced other low-vegetation types (relatively large hatched bars), while evergreen needleleaf (EN) and deciduous broadleaf (DB) trees were relatively often replaced by other high-vegetation types (relatively large plain bars). The low- and high-vegetation cover fractions changed in many regions according to the ESA-CCI LC dataset (Fig. 2.3). During the 1999–2018 period, low vegetation replaced high vegetation in the southern Amazon and northeastern Siberia. Conversely, high vegetation replaced low vegetation in the boreal regions of Lapland and northwestern Siberia. Moreover, arid regions such as central Asia and Australia experienced an expansion of low vegetation over the 1999–2018 period. In Fig. 2.3 we highlight the southern Amazon, Lapland, and central Asia where the vegetation cover fraction changed considerably. These regions are further analyzed in Sect. 2.3.1.

THE IMPLEMENTED LEAF AREA INDEX VARIABILITY

We used the monthly CGLS LAI data described in Sect. 2.2.1 to prescribe model LAI, representing both the seasonal cycle and interannual variability of LAI. The 1 km LAI data were interpolated using conservative interpolation to the HTESSEL grid (Schulzweida, 2022). Next, LAI was disaggregated into low and high LAI (LAI$_L$ and LAI$_H$) based on the low- and high-vegetation cover fractions (A_L and A_H) for use in the HTESSEL model setup with separate low- and high-vegetation tiles (Boussetta et al., 2021; Boussetta and Balsamo, 2021). Figure 2.4 shows the LAI interannual variability as integrated here in HTESSEL, quantified with the standard deviation. The effects of this added variability are presented in Sect. 2.3.2.

2
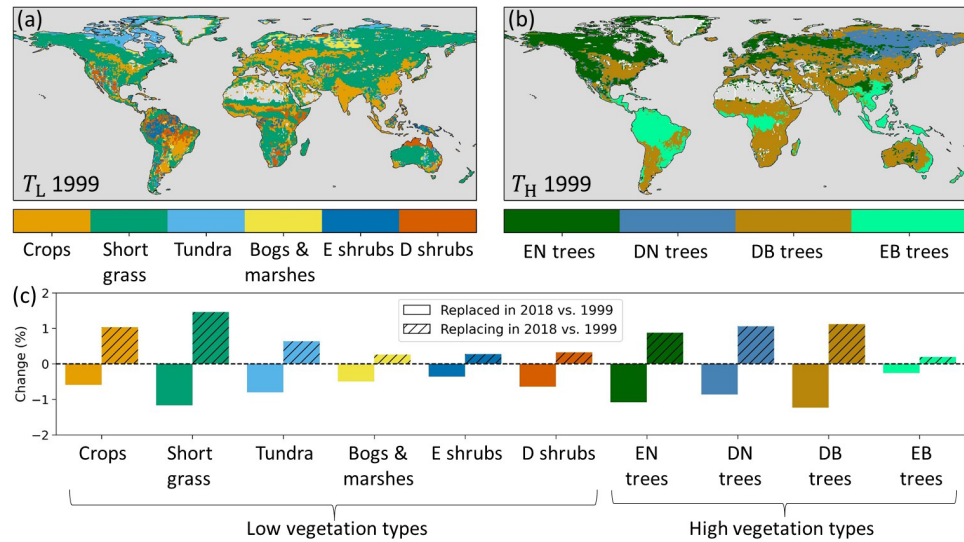
Figure 2.2: **(a)** Model low (T_L) and **(b)** high (T_H) dominant vegetation types in 1999 based on ESA-CCI land cover. **(c)** Changes in low- and high-vegetation type as a percent of the total land points, with plain colors indicating that the vegetation type was replaced in 2018 compared to 1999 and hatched colors that the vegetation replaced another type in 2018 compared to 1999. Note that low vegetation and high vegetation are treated separately and do not replace each other. E stands for evergreen, D for deciduous, N for needleleaf, and B for broadleaf.
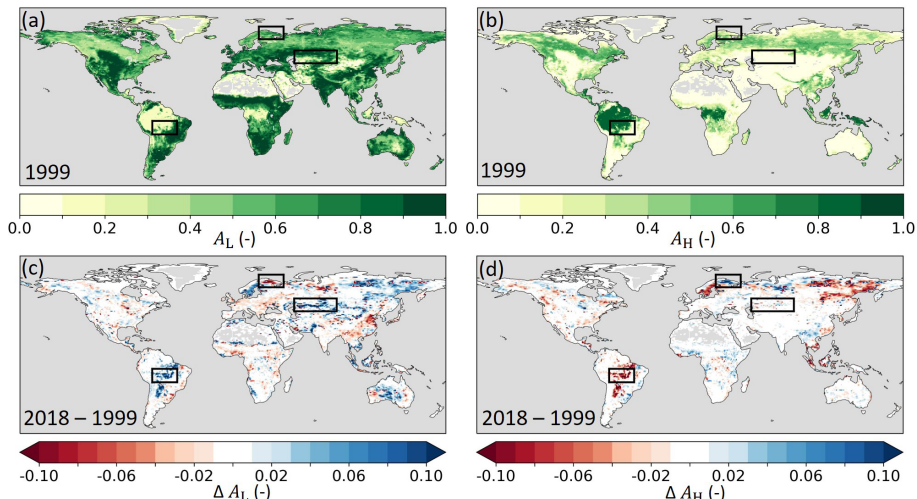
Figure 2.3: **(a)** Model low- (A_L) and **(b)** high-vegetation (A_H) cover fraction in 1999 as well as the absolute difference in **(c)** A_L and **(d)** A_H between 2018 and 1999 (2018–1999) based on ESA-CCI land cover. Blue (red) indicates an increased (reduced) cover in 2018. The black boxes highlight the three regions of the southern Amazon, Lapland, and central Asia that are further analyzed in Sect. 2.3.1.
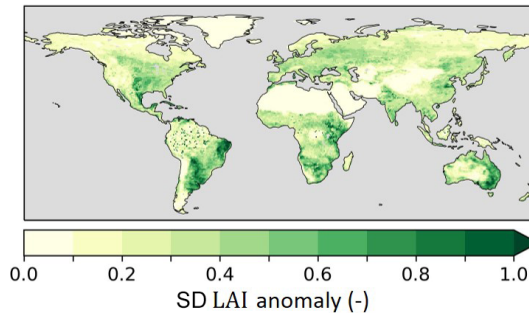
Figure 2.4: Standard deviation (SD) of monthly interannual anomaly CGLS LAI for 1999–2018 as implemented in experiment IAK5 (Table 2.1).

THE IMPLEMENTED VEGETATION-SPECIFIC EFFECTIVE VEGETATION COVER PARAMETERIZATION

The CGLS FCover and LAI data were used (Sect. 2.2.1) to further develop the model effective vegetation cover parameterization as described by Eqs. (2.4)–(2.9). The constant $k = 0.5$ parameter was replaced with a vegetation-specific k to improve spatial and temporal variability of the model C_{eff}. We assumed that the model C_{eff} is equivalent to the CGLS FCover data. Following the model C_{eff} parameterization, FCover is then described as follows:

$$\text{FCover} = 1 - e^{-k\,\text{LAI}}. \tag{2.10}$$

We estimated k for different HTESSEL vegetation types by solving the minimization problem in Eq. (2.11) using a nonlinear least-squares optimization at a 1 km spatial resolution.

$$\min \| 1 - e^{-k\,\text{LAI}} - \text{FCover} \|_2 \tag{2.11}$$

To discriminate vegetation types, the grid cells where each vegetation type maximizes its cover fraction based on the ESA-CCI LC developed in Boussetta and Balsamo (2021) were selected for each year. For each set of grid cells corresponding to each vegetation type, the FCover and LAI 10-daily 1 km data for 1999–2019 were extracted. Here we used a 1×1 km resolution for LAI, FCover, and LC in order to obtain the most representative discrimination of vegetation types and to minimize vegetation mixing within each resolved grid cell. For the optimization of k, a randomly selected subsample of 2000 grid points of the LAI and FCover time steps (10-daily) for each vegetation type was used to keep the analysis computationally feasible, while ensuring a representative sample with robust significance of the fit. In this way, we obtained a sample of 2000 grid cells times 36 time steps per year times 20 years, which equals 1 440 000 data points to be used for the optimization for each vegetation type. This optimization resulted in vegetation-specific k values that were implemented in the HTESSEL code as in Eqs. (2.4)–(2.9). The robustness of the optimization was verified by repeating the random selection procedure several times, which resulted in negligible changes in the k estimates.

2.2.4 Model experiments

We performed experiments with an offline, uncoupled version of HTESSEL to evaluate the effect of the implemented vegetation variability as described in Sect. 2.3. HTESSEL was forced with atmospheric hourly forcing from ECMWF Reanalysis v5 (ERA5) and simulations were performed from 1993–2019, with 1993–1999 as the spin-up period (details in Table S2.1 in the Supplementary material). The model spatial resolution is the n_{128} reduced Gaussian grid corresponding to grid cells of $\sim 75 \times 75$ km. In total, four different model experiments were performed (Table 2.1). In the first experiment, as a benchmark and control experiment (CTR) the land cover of all years was set to the ESA-CCI land cover of 1993, the LAI of all years was set to the 1993–2019 climatology, and the C_{eff} parameterization with $k = 0.5$ was used. This reflects standard settings of the EC-Earth3 version of HTESSEL. In the second experiment (IALC) the interannually varying ESA-CCI LC was included, while in the third experiment (IAK5) we further added interannually varying CGLS LAI. Finally, the model sensitivity to the vegetation-specific C_{eff} parameterization (see Sect. 2.2.2) was evaluated in the fourth experiment (IAKV). The model experiments were evaluated for 1999–2018, which is the longest period to consistently assess all three model implementations with the available evaluation data described in Sect. 2.2.5.

Table 2.1: Details of model experiments.

Experiment	Land cover	Leaf area index	Effective vegetation cover
CTR	ESA-CCI fixed	CGLS climatology	$k = 0.5$
IALC	ESA-CCI interannual	CGLS climatology	$k = 0.5$
IAK5	ESA-CCI interannual	CGLS interannual	$k = 0.5$
IAKV	ESA-CCI interannual	CGLS interannual	k vegetation-specific

2.2.5 Model evaluation

Model variables

The effects of the vegetation-specific C_{eff} parameterization on the model C_{eff} were assessed in IAKV compared to IAK5. Furthermore, we analyzed the effects of the increasingly detailed model land cover and vegetation variability in the three experiments (IALC, IAK5, IAKV) on total evaporation (E) and the evaporation components, i.e., transpiration (E_{t}), soil evaporation (E_{s}), and interception evaporation (E_{i}). In addition, the effects on model near-surface soil moisture (SM_{s}) and subsurface soil moisture (SM_{sb}) were analyzed.

Reference data

The modeled C_{eff} was compared to the CGLS FCover data (Sect. 2.2.1) at the model spatial resolution. As a benchmark for total evaporation we used the Derived Optimal Linear Combination Evapotranspiration version 3 (DOLCEv3), which is a linear combination of estimates from ERA5-land, GLEAM v3.5a and v3.5b, and FLUXCOM-RSMETEO that was regionally weighted based on the performance in reproducing FLUXNET tower evaporation observations (Hobeichi et al., 2021). The associated uncertainty is spatially

and temporally varying based on the gridded evaporation and flux tower observations (Hobeichi et al., 2018). This dataset was selected because it is intended to better capture evaporation temporal variations compared to previous DOLCE versions (v1 and v2) and was therefore found to be suitable for evaluating the effects of the modified temporal and spatial variability of vegetation on evaporation (Hobeichi et al., 2021). Daily evaporation and associated uncertainty at a 0.25° resolution were used for 1999–2018 and were interpolated here using conservative interpolation (Schulzweida, 2022) to the model spatial resolution.

Model near-surface soil moisture (SM$_s$) (0–7 cm) was compared to the combined active–passive ESA-CCI soil moisture product (ESA-CCI SM v06.1), which is generated from satellite-based active and passive microwave products that are combined using the absolute values and dynamic range of the modeled soil moisture of the top 10 cm soil layer from the Global Land Data Assimilation System (GLDAS)-Noah LSM (Liu et al., 2012; Dorigo et al., 2017; Gruber et al., 2017). This dataset provides near-surface (∼ 0–5 cm) soil moisture at a daily resolution on a 0.25° grid. Here we used the combined active–passive product interpolated using conservative interpolation (Schulzweida, 2022) to the model spatial resolution (∼ 75 × 75 km) for 1999–2018 (European Space Agency, 2022). The uncertainty estimates for ESA-CCI SM were also considered as they were provided with the data product and based on error variance of the data used to generate the product (Dorigo et al., 2017). ESA-CCI SM contains spatial and temporal gaps due to densely vegetated areas (tropical forests) and snow coverage. Here only grid cells with a temporal coverage larger than 60 % were used, and, as a consequence, model performance metrics for SM$_s$ were only calculated for these grid cells.

EVALUATION METRICS

The hourly model output was first averaged to monthly values, based on which annual means, monthly climatology, and interannual anomalies were then calculated. To differentiate the seasons (June, July, and August: JJA; September, October and November: SON; December, January, and February: DJF; March, April, and May: MAM), the monthly values were averaged to seasonal means, and interannual seasonal anomalies were calculated. For the evaluation of E and SM$_s$ with respect to reference data, we used the Pearson correlation coefficients r of the interannual monthly and seasonal anomalies. To calculate r of the interannual monthly and seasonal anomalies, the anomalies were detrended assuming a linear trend. Detrending was not applied for the effects of the modified LC, as the interannually varying LC mostly influenced the trend. In addition, we quantified the effects of the improved vegetation variability with the root mean squared error (RMSE). For C_{eff} and E RMSE we used monthly values, while for SM$_s$ we used standardized interannual anomalies. Model SM$_s$ and reference ESA-CCI SM cannot be compared directly in absolute terms due to the different representative soil layers and the imposed dynamic range from the GLDAS-Noah model (Liu et al., 2012), potentially resulting in different temporal variability (Sect. 2.2.5). To overcome this limitation, we standardized the interannual anomalies for model and reference SM$_s$ by dividing the monthly SM$_s$ by the climatological standard deviation.

To test the significance of the r and RMSE differences between the experiments we used a bootstrap, in which 1000 data samples were randomly created by resampling the data of model 1 and model 2 with replacement for each time step. We tested the null

hypothesis that the r and RMSE of model 1 and model 2 with respect to the reference data are not significantly different from each other at the 10 % significance level.

2.3 RESULTS

2.3.1 LAND COVER INTERANNUAL VARIABILITY EFFECTS

The interannually varying land cover from ESA-CCI in experiment IALC resulted in a shift in mean evaporation components (i.e., E_t, E_s, and E_i) compared to the CTR experiment (Fig. 2.5). The last 5 years of the simulations (2014–2019) are considered because the effects of the interannually varying land cover mostly emerge in this period. In the southern Amazon, where A_H was reduced on average from 0.64 to 0.57 in IALC compared to CTR (Fig. 2.3), the mean E_t was reduced by 3 % from 633 to 615 mm yr^{-1} and E_i was reduced by 6 % from 384 to 363 mm yr^{-1}, while E_s increased by 17 % from 156 to 183 mm yr^{-1}. In this region, the total evaporation was reduced only by 1 % from 1174 to 1162 mm yr^{-1} in IALC compared to CTR because the reductions in E_t and E_i were partially compensated for by increased E_s. The reduced E in IALC is closer to the DOLCEv3 E, which in this region is 1160 mm yr^{-1}. We also found an evaporation compensation effect in Lapland, where A_H increased from 0.24 to 0.30, and central Asia, where A_L increased from 0.66 to 0.71 (Fig. 2.3). In Lapland and in central Asia E increased by 2 % and 0.1 %, respectively, moving closer to the DOLCEv3 E (Fig. 2.5b; Supplementary material Table S2.2). In contrast to the small changes in E, the individual E fluxes changed considerably in these two cases (Fig. 2.5d, f, h).

The changes in E_t and E_s also induced changes in soil moisture because E_s extracts water exclusively from the near-surface soil layer (SM$_s$), while E_t originates mostly from deeper soil layers (SM$_{sb}$). However, we observed only marginal differences between mean SM$_s$ and SM$_{sb}$ in IALC compared to CTR (Fig. 2.6), except for the southern Amazon SM$_s$. The increased E_s in the southern Amazon reduced the SM$_s$ by 2 %, as more near-surface soil moisture was extracted (Fig. 2.6b). Individual evaporation fluxes influence the timing of total evaporation and soil moisture differently. However, the overall minor magnitude of changes in total E and SM$_s$ in IALC compared to CTR led to marginal changes in RMSE and Pearson correlation coefficients with respect to the reference data in the three highlighted cases (Supplementary material Table S2.3, Figs. S2.1–S2.3).
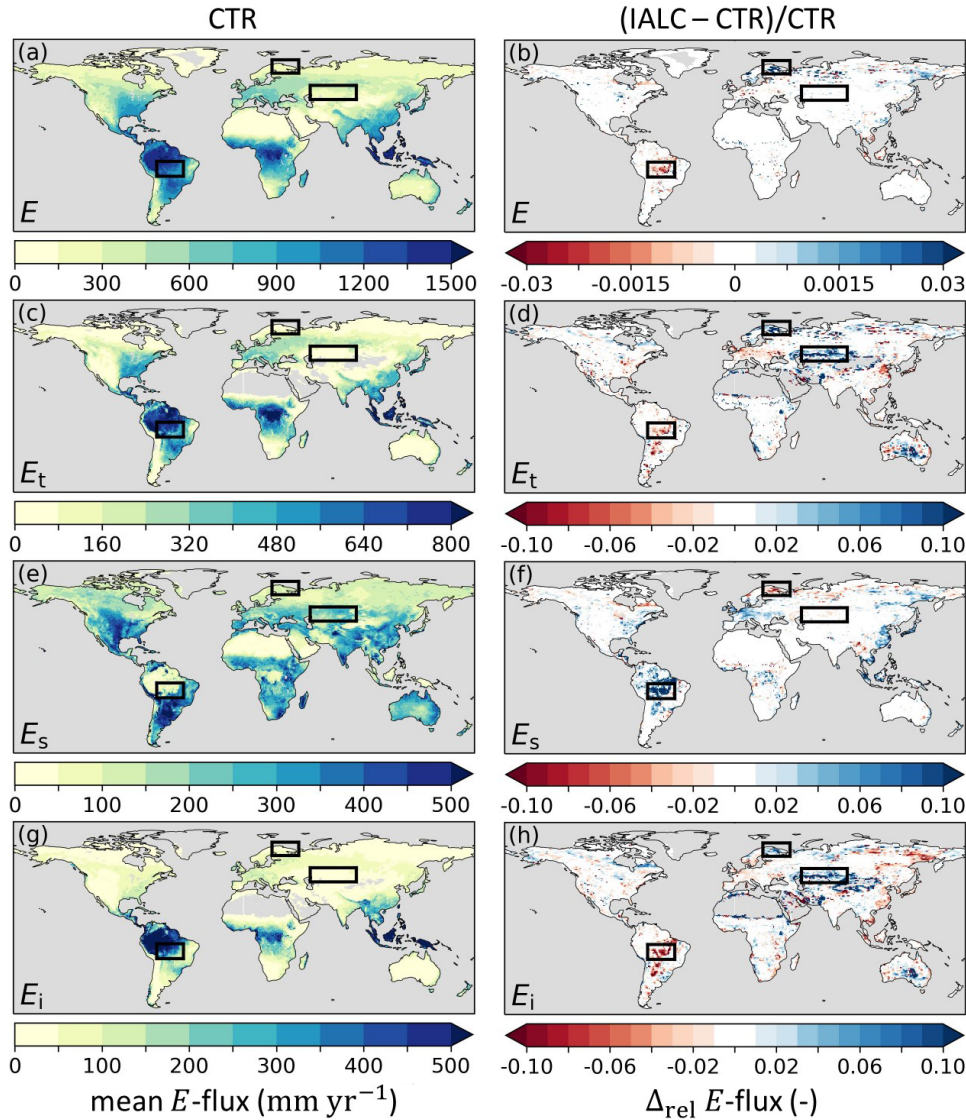
Figure 2.5: Annual mean evaporation fluxes (2014–2018) in experiment CTR with **(a)** total evaporation (E), **(c)** transpiration (E_t), **(e)** soil evaporation (E_s), and **(g)** interception evaporation (E_i), as well as the relative difference (Δ_{rel}) between annual mean evaporation fluxes in experiments IALC and CTR ((IALC−CTR)/CTR) for **(b)** E, **(d)** E_t, **(f)** E_s, and **(h)** E_i. Blue (red) indicates an increased (reduced) flux. Grey land areas indicate regions with annual mean E fluxes $< 0.1\,\mathrm{mm\,yr^{-1}}$. The boxes highlight the three regions of the southern Amazon, Lapland, and central Asia with major land cover changes (Fig. 2.3). Results with respect to DOLCEv3 E are presented in Supplementary material Fig. S2.1. See Table 2.1 for details of the experiments.
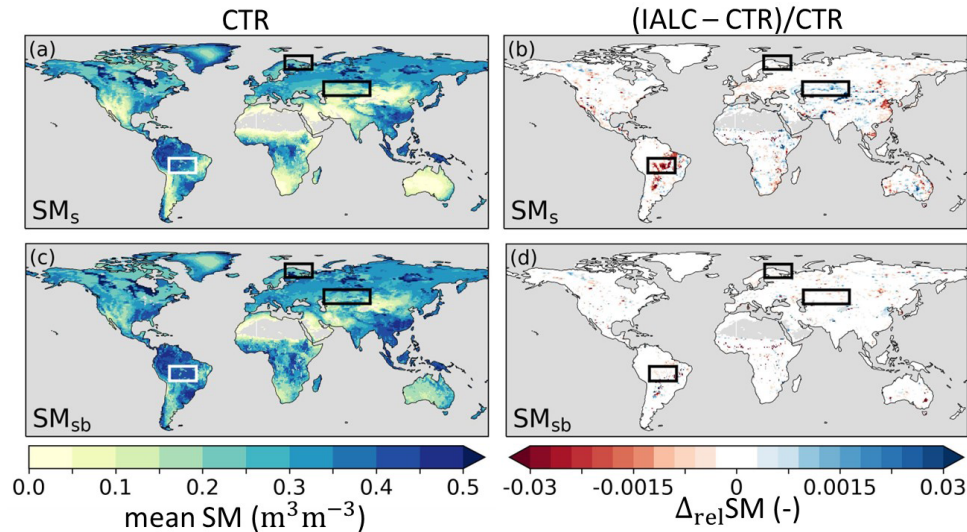
Figure 2.6: Annual mean soil moisture (2014–2018) (SM) in experiment CTR with **(a)** near-surface soil moisture (SM_s) and **(c)** subsurface soil moisture (SM_{sb}), as well as the relative difference (Δ_{rel}) between annual mean SM in experiments IALC and CTR ((IALC–CTR)/CTR) for **(b)** SM_s and **(d)** SM_{sb}. Blue (red) indicates increased (reduced) soil moisture. Grey land areas indicate regions with annual mean SM < 0.01 m³ m⁻³. The boxes highlight the three regions of the southern Amazon, Lapland, and central Asia with major land cover changes (Fig. 2.3). See Table 2.1 for details of the experiments.

2.3.2 LEAF AREA INDEX INTERANNUAL VARIABILITY EFFECTS

The inclusion of interannual LAI variability in IAK5 (Fig. 2.4) generally led to an increased anomaly standard deviation (i.e., variability) of E (Fig. 2.7a, b). This effect is mostly dominated by E_t (Fig. 2.7d), which, in the model, is linearly related to LAI (Eq. 2.1). Figure 2.7d and h show that the variability in E_t and E_i was mostly increased in semiarid regions such as the Great Plains region of the US, central Asia, and southern Africa, with a stronger effect for E_t than for E_i. In contrast, the E_s variability was reduced with the enhanced LAI variability in these semiarid regions but was increased in more temperate regions such as in Europe, the eastern US, and the La Plata Basin in South America (Fig. 2.7e, f). While the E_t anomaly variability considerably increased in IAK5 compared to IALC in semiarid regions, the anomaly variability in subsurface soil moisture (SM_{sb}) that acts as the main source of E_t was reduced in these regions (Fig. 2.8c, d). On the other hand, the anomaly variability of SM_s increased (Fig. 2.8a, b), while the E_s variability was reduced.

Figure 2.9 shows that the Pearson correlation coefficient (r) of anomaly E with respect to DOLCEv3 increased in IAK5 compared to IALC in 85 % of the land area in which the r was significantly different in IAK5 compared to IALC. Consistently, the r of anomaly SM_s with respect to ESA-CCI SM also improved in 85 % of the significantly changing land area. For both E and SM_s r increased mostly in semiarid regions with predominantly low vegetation (Fig. 2.3).
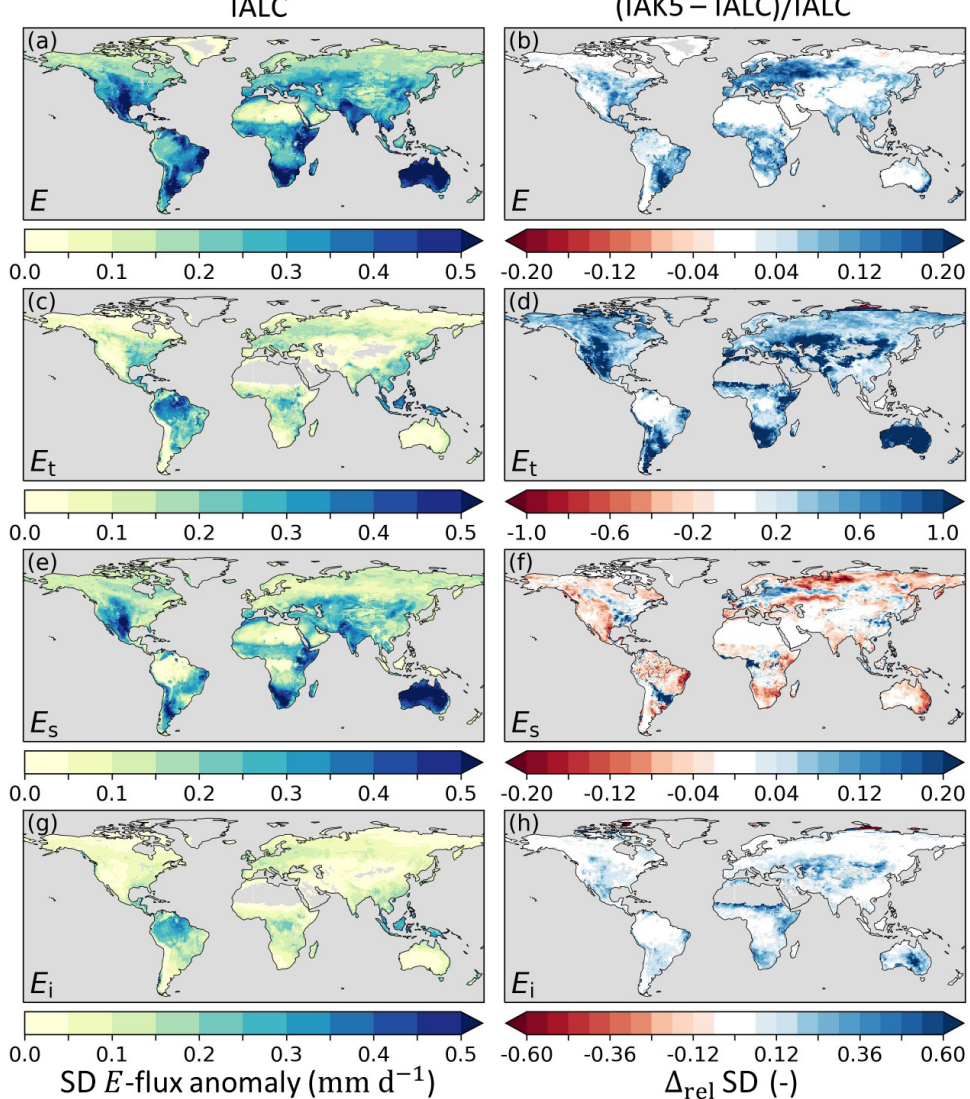
Figure 2.7: Standard deviation (SD) of anomaly evaporation fluxes in experiment IALC with **(a)** total evaporation (E), **(c)** transpiration (E_t), **(e)** soil evaporation (E_s), and **(g)** interception evaporation (E_i), as well as the relative difference (Δ_{rel}) between the anomaly E SD in experiments IAK5 and IALC ((IAK5−IALC)/IALC) for **(b)** E, **(d)** E_t, **(f)** E_s, and **(h)** E_i. Blue (red) indicates an increased (reduced) SD. See Table 2.1 for details of the experiments.

2
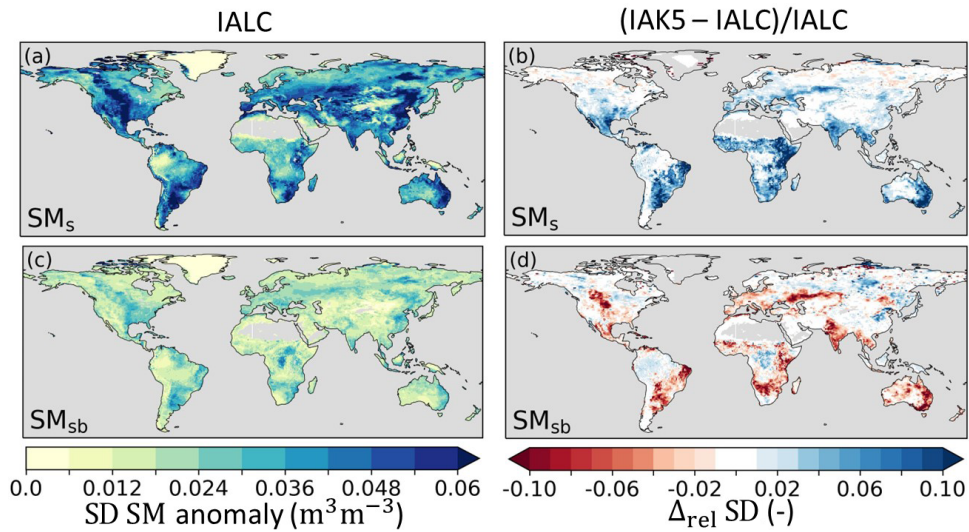
Figure 2.8: Standard deviation (SD) of anomaly soil moisture (SM) in experiment IALC with **(a)** near-surface soil moisture (SM_s) and **(c)** subsurface soil moisture (SM_{sb}), as well as the relative difference (Δ_{rel}) between the anomaly SM SD in experiments IAK5 and IALC ((IAK5–IALC)/IALC) for **(b)** SM_s and **(d)** SM_{sb}. Blue (red) indicates an increased (reduced) variability. See Table 2.1 for details of the experiments.
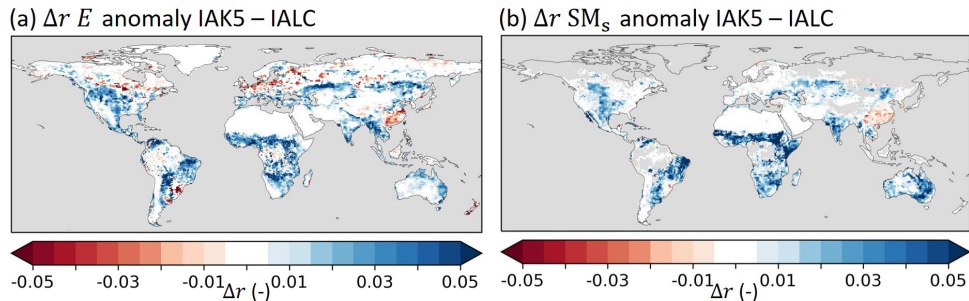
Figure 2.9: Pearson correlation difference (Δr) between experiments IALC and IAK5 (IAK5–IALC) for **(a)** monthly anomaly total evaporation (E) with respect to DOLCEv3 evaporation and **(b)** monthly anomaly near-surface soil moisture (SM_s) with respect to ESA-CCI SM. Blue (red) indicates an increased (reduced) correlation in IAK5 compared to IALC, white indicates small and/or insignificant Δr, and grey indicates no data points. See Table 2.1 for details of the experiments. Similar figures for seasonal anomalies are presented in Supplementary material Figs. S2.5–S2.6.

2.3.3 VEGETATION-SPECIFIC EFFECTIVE VEGETATION COVER PARAMETERI-ZATION EFFECTS

The observed relationship of LAI and FCover in Fig. 2.10 is broadly consistent with the shape of the exponential functions with the vegetation-specific k, with RMSEs between 0.018 and 0.053 for the individual vegetation types. All optimized LAI–FCover relations are characterized by k values that at 0.351–0.458 are consistently lower than the original $k = 0.5$, which has been used as the constant default value in most HTESSEL applications so far (Alessandri et al., 2017; Boussetta et al., 2021). We found that the k values for low-vegetation types (0.438–0.458) are higher than for high-vegetation types (0.351–0.396), except for tundra regions (0.375) (Fig. 2.10 and Supplementary material Table S2.4). These findings are in line with our expectations, as leaf organization of low vegetation is more regular (larger k) than leaf organization of high vegetation, where leaves are found more on top of each other (smaller k) (Chen et al., 2005, 2021).

The vegetation-specific C_{eff} parameterization (IAKV) generally reduced the k values compared to the $k = 0.5$ setup (IAK5), and as a consequence the associated vegetation densities $c_{v,L}$ and $c_{v,H}$ also decreased (Eqs. 2.8 and 2.9). On average, the global mean C_{eff} was reduced from 0.21 in IAK5 to 0.19 in IAKV (Fig. 2.11). The reduced C_{eff} considerably reduced the RMSE with respect to the FCover data in IAKV compared to IAK5 (Fig. 2.12), as expected from the parameterization optimization presented in Fig. 2.10. The RMSE was reduced the most over the boreal and tropical forests, with an average RMSE reduction from 0.12 to 0.06 for evergreen needleleaf trees and from 0.05 to 0.03 for evergreen broadleaf trees. On the other hand, the differences in regions with predominantly low vegetation were smaller because the fitted k value was closer to the original $k = 0.5$, with an average RMSE reduction from 0.06 in IAK5 to 0.05 in IAKV for crops and from 0.04 to 0.03 for short grass. For low vegetation, the effects were not consistent throughout the seasons, with RMSE increasing at high latitudes in JJA (Fig. 2.12d). Here the C_{eff} in IAK5 was smaller than the CGLS FCover and is further reduced in IAKV, increasing the RMSE. This was likely caused by a poor fit for short grass at LAI > 2 (Fig. 2.10b) and tundra at LAI > 1 (Fig. 2.10g).

The reduced model C_{eff} in IAKV compared to IAK5 led to a shift in individual evaporation fluxes. On average, E_s increased and E_t and E_i were reduced, while the total E was not very affected (Supplementary material Fig. S2.7). These shifts led to changes in the temporal distribution of the evaporation. Figure 2.13 shows quite mixed results of the vegetation-specific C_{eff} parameterization for the model E RMSE with respect to DOLCEv3. The RMSE was consistently reduced during summer months in temperate regions such as in Europe, the eastern US, and eastern China (JJA), as well as in southeastern Brazil and southern Africa (DJF). On the other hand, the results for tropical and boreal regions were less consistent throughout the seasons (Fig. 2.13). The effects of the vegetation-specific C_{eff} on SM_s RMSE with respect to ESA-CCI SM show consistent RMSE reductions in the JJA period for Canada and southeastern Brazil and in the DJF period for the Sahel (Fig. 2.14). Consistent with the C_{eff} RMSE increase in boreal regions in JJA (Fig. 2.12), the Pearson correlation coefficient for monthly anomaly E with respect to DOLCEv3 E was significantly reduced in these regions in IAKV compared to IAK5, while other regions were not very affected (Supplementary material Fig. S2.15). On the other hand, the correlation of monthly anomaly SM_s with respect to ESA-CCI SM did not con-

siderably change (Supplementary material Fig. S2.15).
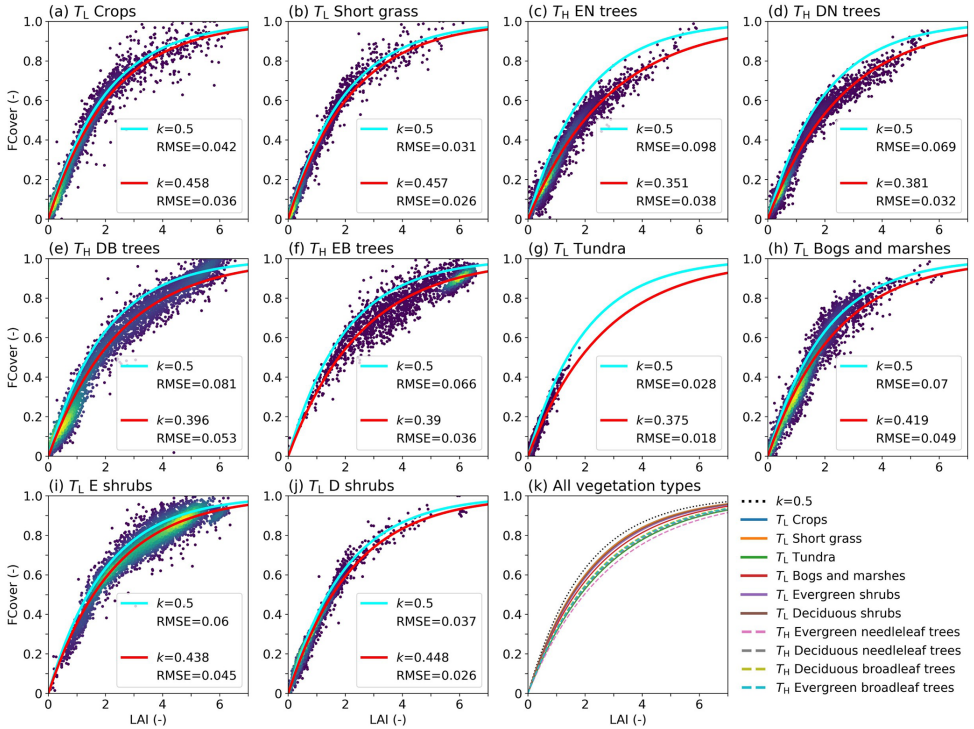
Figure 2.10: **(a–j)** LAI vs. FCover for a subsample (5000) of the selected points used for the least-squares optimization for all vegetation types with the optimized LAI–FCover relation in red (Eq. 2.10) and the $k = 0.5$ relation in light blue, with RMSE values of the data points with respect to the curve. The colors indicate the point density, with purple indicating low density and yellow high density. **(k)** The optimized LAI–FCover relation for all vegetation types. E stands for evergreen, D for deciduous, N for needleleaf, and B for broadleaf. Values of k and RMSE are also presented in Supplementary material Table S2.4.
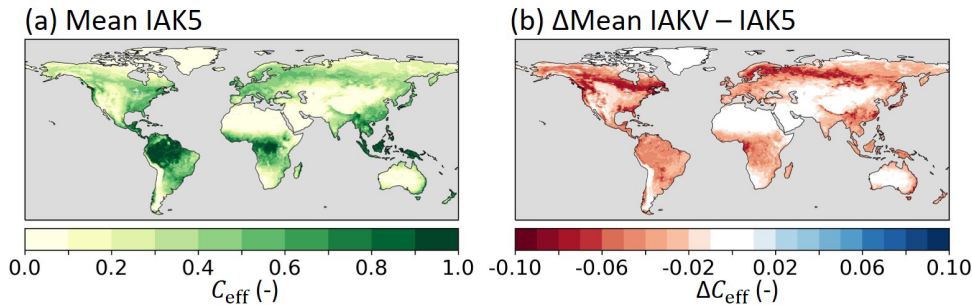
Figure 2.11: **(a)** Mean monthly model effective vegetation cover (C_{eff}) in experiment IAK5 and **(b)** the absolute difference between IAKV and IAK5 (IAKV−IAK5) mean monthly C_{eff}. Red (blue) indicates a reduced (increased) C_{eff} in IAKV compared to IAK5. Details of model experiments are in Table 2.1.
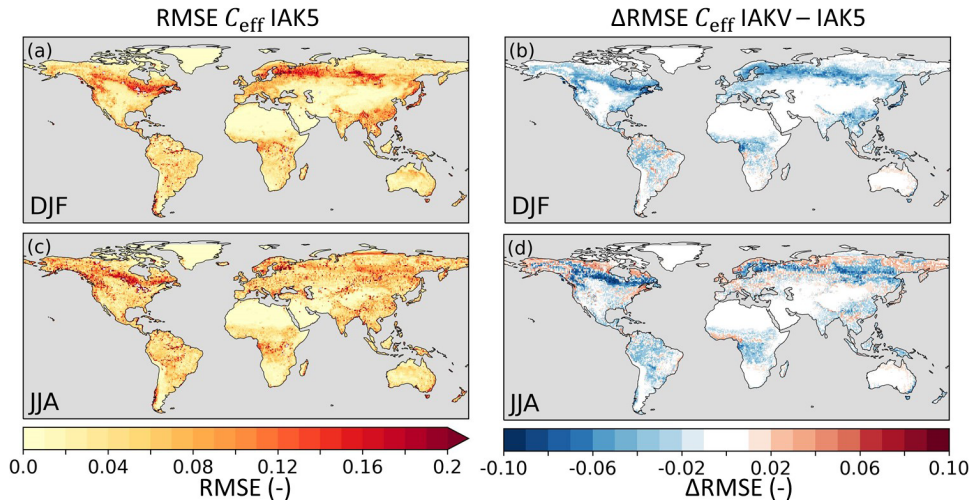
Figure 2.12: Root mean squared error (RMSE) of model seasonal C_{eff} in experiment IAK5 with respect to CGLS FCover for DJF **(a)** and JJA **(c)**, with red indicating a larger RMSE. The difference between RMSE in IAK5 and IAKV (IAKV–IAK5) for DJF **(b)** and JJA **(d)** with blue (red) indicating a reduced (increased) RMSE. White indicates small and/or insignificant ΔRMSE. See Table 2.1 for details of the experiments. Similar figures for monthly values and all the seasons are presented in Supplementary material Figs. S2.9–S2.10.

2
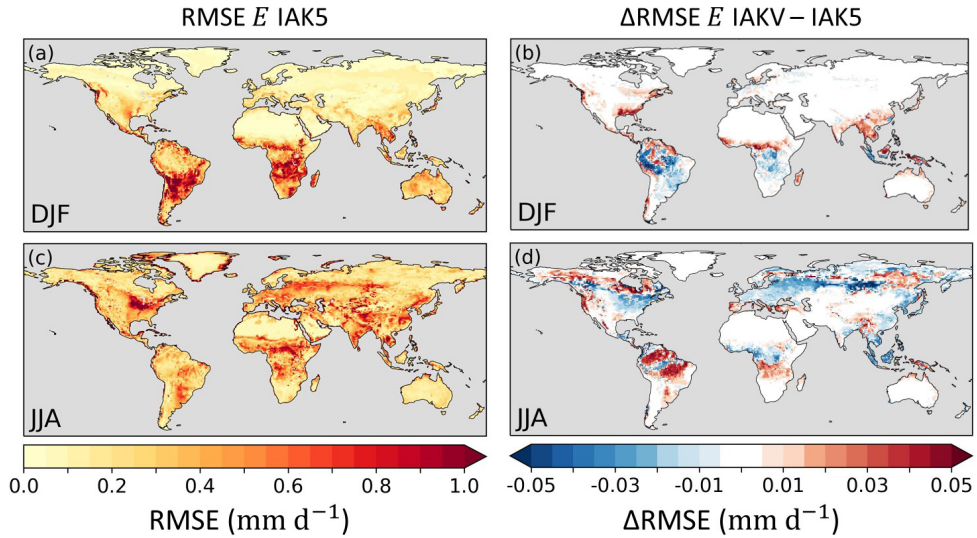
Figure 2.13: Root mean squared error (RMSE) of model seasonal E in experiment IAK5 with respect to DOLCEv3 E for DJF **(a)** and JJA **(c)**, with red indicating a larger RMSE. The difference between RMSE in IAK5 and IAKV (IAKV–IAK5) for DJF **(b)** and JJA **(d)** with blue (red) indicating a reduced (increased) RMSE. White indicates small and/or insignificant ΔRMSE. See Table 2.1 for details of the experiments. Similar figures for monthly values and all the seasons are presented in Supplementary material Figs. S2.11–S2.12.
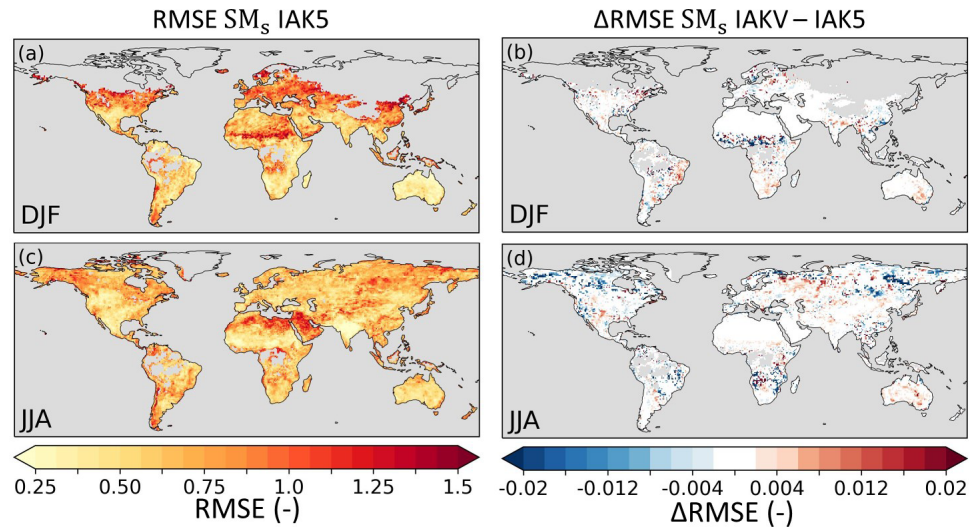
Figure 2.14: Root mean squared error (RMSE) of model standardized interannual seasonal anomaly SM_s in experiment IAK5 with respect to ESA-CCI SM for DJF **(a)** and JJA **(c)**. The difference between RMSE in IAK5 and IAKV (IAKV–IAK5) for DJF **(b)** and JJA **(d)** with blue (red) indicating a reduced (increased) RMSE. White indicates small and/or insignificant ΔRMSE, and grey indicates no data points. See Table 2.1 for details of the experiments. Similar figures for monthly values and all the seasons are presented in Supplementary material Figs. S2.13–S2.14.

2.3.4 COMBINED EFFECTS OF LAND COVER, LEAF AREA INDEX, AND EFFECTIVE VEGETATION COVER

The results presented in Sect. 2.3.2 demonstrate that the interannually varying LAI in experiment IAK5 considerably improved the correlation of E and SM_s with respect to reference data. On the other hand, the annually varying LC and vegetation-specific C_{eff} affected correlations merely to a minor degree (Sect. 2.3.1 and 2.3.3). Here, we further elaborate on the effects of combining the enhanced variability in LC, LAI, and C_{eff} on correlation of E and SM_s.

Figure 2.15 shows that the E correlation improved in 68 % (JJA) and 54 % (DJF) of the land area in which the r significantly changed in IAKV compared to CTR. Significant reduction of r is found over boreal regions, which is related to the effects of the effective vegetation cover parameterization, as discussed in Sect. 2.3.3 and shown in Fig. S2.14. Figures 2.15b and d show that the SM_s correlation consistently and significantly improved in 83 % (JJA) and 76 % (DJF) of the land area in which the r significantly changed in IAKV compared to CTR. The E and SM_s correlations got consistently stronger during dry periods in regions with a semiarid climate and predominantly low vegetation (Figs. 2.3 and 2.15). For example, in northeastern Brazil during the dry JJA season, the correlation coefficient for E increased from $r = 0.79$ in CTR to 0.84 in IAKV with respect to DOLCEv3 and for SM_s from $r = 0.57$ to 0.67 with respect to ESA-CCI SM. Similarly, in western India during the dry DJF season, the correlation coefficient for E increased from $r = 0.78$ to 0.85 and for SM_s from $r = 0.45$ to 0.73.
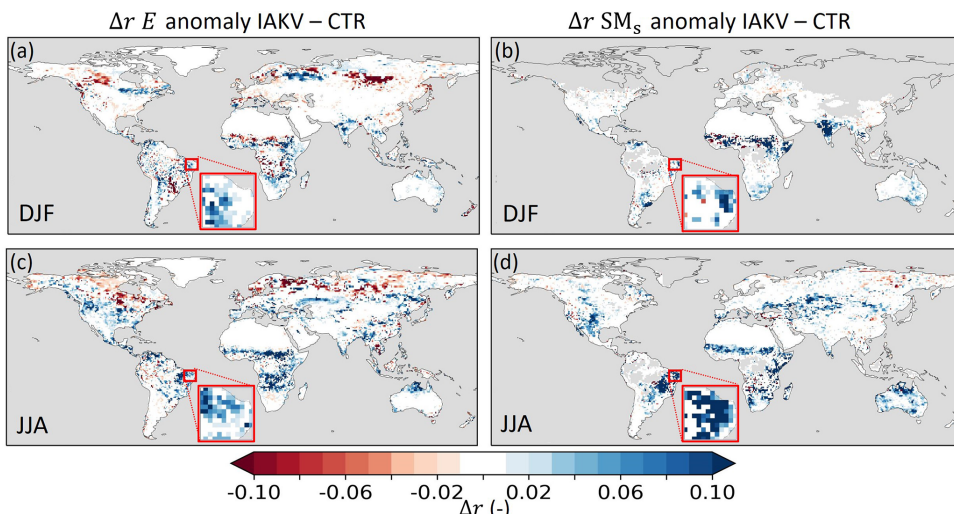
Figure 2.15: Pearson correlation coefficient difference (Δr) between experiment IAK5 and IAKV (IAKV−IAK5) for **(a, c)** seasonal anomaly total evaporation (E) with respect to DOLCEv3 evaporation for DJF and JJA and **(b, d)** seasonal anomaly near-surface soil moisture (SM_s) with respect to ESA-CCI SM for DJF and JJA. Blue (red) indicates an increased (reduced) correlation in IAKV compared to IAK5, white indicates small and/or insignificant Δr, and grey indicates no data points. The red box is highlighted in Fig. 2.16. See Table 2.1 for details of the experiments. Similar figures for all the seasons and monthly anomalies are presented in Supplementary material Figs. S2.18–S2.20.

2

To further explore the effects in these semiarid regions, we zoom in to northeastern Brazil for the 2010–2013 period (Fig. 2.16). This period is characterized by positive LAI and C_{eff} anomalies in JJA 2011 and negative LAI and C_{eff} anomalies in JJA 2012 (Fig. 2.16a, b). The negative LAI and C_{eff} anomalies in 2012 characterize a dry period in which the negative E anomaly was magnified in IAKV compared to CTR (Fig. 2.16c). During this dry period, E_t was reduced, while E_s increased. This is consistent with the soil moisture response presented in Fig. 2.16d, as the SM_s was reduced (due to more E_s) and the SM_{sb} increased (due to less E_t) during the 2012 dry period. Opposite effects were found for the 2011 period with positive LAI and C_{eff} anomalies. So in this specific case, the variability in E_t and SM_s anomalies was enhanced in IAKV compared to CTR, while the variability in E_s and SM_{sb} anomalies was dampened. This is consistent with the results presented in Figs. 2.7 and 2.8, in which the effects of the interannually varying LAI on the variability of E and SM are presented.

The opposing effects of the enhanced LAI variability on anomaly E_t and SM_{sb} can be explained by a negative feedback between vegetation and soil moisture schematized on the right side in Fig. 2.17a. During dry periods, the soil moisture is reduced; this lower soil water availability can result in vegetation water stress, consequently leading to lower vegetation activity in terms of transpiration and primary production, which is reflected, for example, in the typical dry season browning of grass species in low-vegetation regions and in the model represented by negative LAI and C_{eff} anomalies (Fig. 2.16a, b). As transpiration is reduced (Fig. 2.16c), the negative subsurface soil moisture anomaly is similarly reduced because less water is extracted (Fig. 2.16d). On the other hand, the enhanced vegetation variability activated a positive feedback between anomaly vegetation activity and anomaly SM_s, as illustrated on the left side of Fig. 2.17a. Reduced vegetation activity is reflected in the model by a reduced C_{eff} and an increased bare soil fraction (Sect. 2.7), which leads to an increased E_s (Fig. 2.16b) and, as a consequence, less SM_s during a dry period as long as soil moisture is available (Fig. 2.16d).

Figure 2.17b and c show that the positive feedback between E_s and SM_s, as introduced by the improved vegetation variability, is the strongest over semiarid regions with low vegetation, while the negative feedback between E_t and SM_{sb} is more pronounced for temperate regions with deciduous vegetation and crops, where the interannual LAI variability is larger (Fig. 2.4).
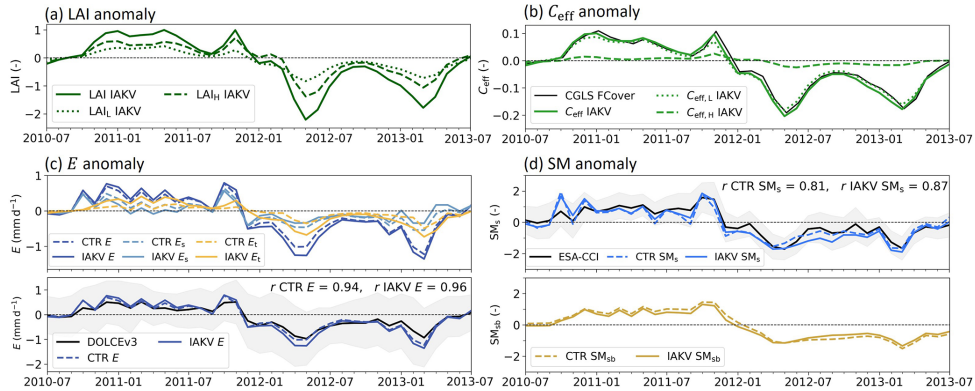
Figure 2.16: Time series of the northeastern Brazil case highlighted in Fig. 2.15 for **(a)** LAI anomalies. **(b)** Effective vegetation cover (C_{eff}) anomalies with the CGLS FCover data in black as a reference. **(c)** Evaporation anomalies with E total evaporation, E_t being transpiration, E_s soil evaporation, and E_i interception evaporation; DOLCEv3 E is in black as a reference. **(d)** Soil moisture standardized anomalies with SM_s near-surface soil moisture and SM_{sb} subsurface soil moisture; ESA-CCI SM is in black as a reference. Dashed lines in **(c)** and **(d)** represent experiment CTR and solid lines IAKV. The shading in **(c)** and **(d)** represents the uncertainty associated with the reference data. For this case T_L is short grass, T_H is deciduous broadleaf trees, $A_L = 0.84$, and $A_H = 0.16$.
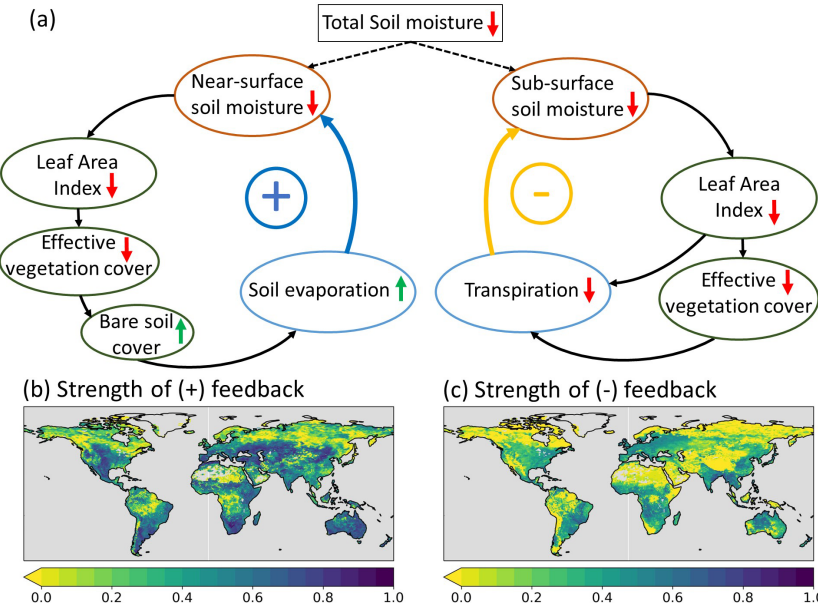
Figure 2.17: **(a)** Processes contributing to the anomaly vegetation–soil moisture feedback mechanisms as activated with the improved vegetation variability in IAKV compared to CTR. Upward (downward) arrows indicate positive (negative) change in the involved variables. Positive (blue) arrows indicate positive feedback and negative (yellow) arrows indicate negative feedback. The ± symbols refer to the resulting positive or negative feedback loop relative to the sign of the change in the involved variables. The strength of the feedbacks **(b, c)** is quantified as the absolute correlation between anomaly ΔE_s and ΔSM_s **(b)** and between ΔE_t and ΔSM_{sb} **(c)**, with Δ representing the difference between anomaly CTR and IAKV (IAKV–CTR).

2.4 Discussion

2.4.1 Synthesis and implications

The results presented in Sect. 2.3.4 indicate overall improvements of correlation coefficients of E and SM_s with all three aspects of vegetation variability implemented. We attribute these effects primarily to the implementation of interannually varying LAI, as the effects of the LC variability and vegetation-specific C_{eff} on E and SM_s were smaller (Sect. 2.3.1 and 2.3.3). The pronounced improvements in SM_s and E correlation in semi-arid regions (Fig. 2.15) are directly related to the feedback mechanisms typical of water-limited regions that were activated by the vegetation variability. Regions where the positive feedback is strong (Fig. 2.17b) coincide with the regions that exhibit a strengthening of the correlations. In the model setup with seasonally varying LAI only (experiments CTR and IALC), the feedbacks in Fig. 2.17 are not represented because the interaction between SM and LAI is activated by the interannually varying LAI. In particular, the interactions between LAI, C_{eff}, and bare soil cover are only captured if model C_{eff} is exponentially related to LAI (Sect. 2.2.2). This finding complements the arguments from previous studies for using the exponential LAI–C_{eff} relation instead of the lookup-table C_{eff} in HTESSEL (Alessandri et al., 2017; Johannsen et al., 2019; Nogueira et al., 2020, 2021).

Recent studies also applied data assimilation methods to integrate satellite-based LAI in LSMs. For example, Rahman et al. (2022) found improved anomaly correlations of transpiration in many areas when integrating satellite-based LAI in the LSM called Noah-MP (Noah Multi-Parameterization), with the largest effects in the regions where E and SM_s anomaly correlations consistently improved in our results (Fig. 2.9). However, this study also found limited sensitivity of model surface and root zone soil moisture when only LAI assimilation was applied (Rahman et al., 2022). Similarly, Albergel et al. (2017) concluded that LAI assimilation only affected deeper SM. In contrast, our results showed considerable changes in near-surface soil moisture when integrating CGLS LAI; this can be explained by the interplay between LAI, effective vegetation cover, soil evaporation, and near-surface soil moisture schematized in Fig. 2.17, which apparently differs from the interplay in Noah-MP (Rahman et al., 2022) and ISBA (Albergel et al., 2017).

The vegetation-specific effective vegetation cover parameterization presented in Sect. 2.3.3 generally resulted in an improved match of model C_{eff} and CGLS FCover (Fig. 2.12), which was expected because the FCover data were used for the estimation of the exponential coefficient k based on least-squares minimization (Sect. 2.2.3). CGLS FCover explicitly represents the fraction of green vegetation cover and therefore matches the model actively transpiring vegetation fraction C_{eff}. However, the non-green vegetated area cover also affects the atmosphere by, e.g., modifying albedo and roughness lengths, which is not considered in the model, as non-green vegetation is represented as bare soil. This is a limitation for the present implementation of the vegetation-specific effective vegetation cover parameterization. The results presented in Fig. 2.13 showed both increased and reduced RMSE for E with respect to the reference data in IAKV compared to IAK5. Consistent reductions of E RMSE in Europe and the eastern US in the JJA period were found. These regions coincide with regions with a high density of FLUXNET tower observations used for generation of the DOLCEv3 E (Hobeichi et al., 2021). The lack of tower observations in the tropics, in the Sahel, in southeastern Asia, and at high latitudes

may potentially explain the mixed RMSE results in these regions presented in Fig. 2.13. For high latitudes (e.g., northern Canada and eastern Siberia) the RMSE for both E as C_{eff} increased and the Pearson correlation was reduced (Supplementary material Fig. S2.15) in IAKV compared to IAK5 for the JJA period. This might be at least in part related to the poor fit of the parameterization for high LAI values for short grass and tundra, as explained in Sect. 2.3.3 (Fig. 2.10).

The interannually varying land cover locally affected the model E and SM as expected, with reduced (increased) E driven by corresponding reductions (increases) in high-vegetation cover fraction (Figs. 2.5 and 2.6). However, the effects on E and SM are likely underestimated due to the HTESSEL land cover structure in which the dominant vegetation type and cover fraction are used and vegetation mixing within high- or low-vegetation types is not represented (Fig. 2.1). With this, only major changes in the ESA-CCI vegetation types and fractions are captured by the model. In IALC we evaluated the effects of interannually varying LC individually, but for internal consistency LAI and LC interannual variations should ideally be used together as they are interdependent. The local effects of the interannually varying land cover on the total E were considerably smaller than on the individual E fluxes (Fig. 2.5). The reduced (increased) E_{t} and E_{i} were compensated for by increased (reduced) E_{s}. This compensation is related to the C_{eff} parameterization (Eq. 2.6) and also to the offline setup, which does not allow for couplings with the atmosphere. Reduced A_{H} in the Amazon (Fig. 2.3) led to a reduced C_{eff} and an increased bare soil fraction (Sects. 2.4–2.7) and therefore reduced E_{t} and E_{i} as well as increased E_{s} in order to fulfill the atmospheric evaporation demand defined by the prescribed atmospheric forcing. Similarly, the on average reduced C_{eff} with the vegetation-specific C_{eff} parameterization (Fig. 2.11) introduced in experiment IAKV led to a shift in annual mean individual E fluxes, with increased E_{s} and reduced E_{t} and E_{i} (Supplementary material Fig. S2.7).

It is important to note that the partitioning of evaporation into the three individual components E_{t}, E_{s}, and E_{i} in the model remains problematic to compare with observations. There is widespread consensus that, globally averaged, transpiration is the largest land evaporation flux component, followed by soil evaporation and interception evaporation (Miralles et al., 2011; Wei et al., 2017; Nelson et al., 2020). However, estimates of the average global E_{t} contribution to total terrestrial evaporation are subject to major uncertainties, with the global E_{t} contribution quantified in the range of 35 %–80 % (Schlesinger and Jasechko, 2014; Coenders-Gerrits et al., 2014). The global mean modeled partitioning of evaporation in our study is on the low end of these estimates with 39 % E_{t}, 38 % E_{s}, and 20 % E_{i} in CTR and 38 % E_{t}, 41 % E_{s}, and 20 % E_{i} in IAKV (the values do not add to 100 % due to open-water evaporation). Despite the consistent improvements in anomaly correlation coefficients of E and SM_{s} found in IAKV compared to CTR (Fig. 2.15), the apparently low contribution of E_{t} to total E needs further evaluation, which was out of scope in this study.

2.4.2 METHODOLOGICAL LIMITATIONS

Our model experiments were performed in an offline mode with prescribed atmospheric forcing, which allowed us to analyze individual hydrological processes in detail. However, the fixed atmospheric model input considerably constrains changes in model sur-

face fluxes. Moreover, the ERA5 forcing used here is based on an LSM that does not represent land cover and vegetation variability, which is partially corrected for by data assimilation of observations (Hersbach et al., 2020; Nogueira et al., 2021). The potential mismatch between our LSM and the ERA5 atmospheric forcing may have also influenced the observed model effects. Another possible limitation is the absence of recalibration of model parameters, such as roughness lengths and minimum stomatal resistances. Fixed model parameters were originally calibrated using the lookup-table C_{eff} parameterization, MODIS LAI, and GLCC LC, and they have not been adjusted for the three new model scenarios tested here (IALC, IAK5, and IAKV). This was also emphasized by Johannsen et al. (2019), Nogueira et al. (2020, 2021), and Boussetta et al. (2021), who concluded that model vegetation changes should be implemented in an integral context and recalibration of model parameters is needed.

This study emphasizes the importance of realistic representation of vegetation variability for modeling land surface–atmosphere interactions. However, for further applications exploring how the vegetation variability influences atmospheric variables in a coupled model setup is needed. The availability of reliable reference data is therefore fundamental to properly understand and model the processes of relevance for the land surface and interaction with the atmosphere. Here, the evaluation of model performance was limited to total evaporation and near-surface soil moisture. The evaluated performances of model E and SM_s need to be interpreted in a careful way, bearing in mind the uncertainties. For total evaporation we used the DOLCEv3 evaporation data that merge FLUXNET tower observations with evaporation from FLUXCOM-RSMETEO, GLEAM v3.5a and v3.5b, and ERA5-land, which all include very specific model assumptions on vegetation representations. Although these data are considered suitable for time series and trend analyses, the associated uncertainty estimates are large (Hobeichi et al., 2021) (Fig. 2.16). Figure 2.16c shows that the DOLCEv3 interannual variability is systematically smaller than the modeled variability. This limited interannual variability in DOLCEv3 could be at least in part related to the combination of several products because the averaging based on FLUXNET towers unavoidably dampens the anomalies, reducing the interannual variability. Evaluation of the modeled near-surface soil moisture was limited by missing data due to dense forests or snow cover and the lack of information on the representative soil depth. While the ESA-CCI combined active–passive SM product was generated using the absolute values and the dynamic range of GLDAS-Noah soil moisture, preserving the dynamics and trends of the original retrievals (Liu et al., 2012), it is important to note that during dry-downs the soil moisture dynamics can also be impacted to some extent, as highlighted by Raoult et al. (2022). However, we still find the ESA-CCI SM to be the best-suited globally available reference data for our study because they represent a direct product of remote sensing observations, without directly blending land surface model dynamics as done for DOLCEv3.

2.5 CONCLUSIONS

This study aimed to address the limitations of state-of-the-art land surface models in representing spatial and temporal vegetation dynamics. We evaluated the effects of improving the representation of land cover and vegetation variability based on satellite observational products in the HTESSEL land surface model. Specifically, we directly integrated satellite-based interannually varying land cover and seasonally and interannually varying LAI. In addition, we formulated and integrated an effective vegetation cover parameterization that can distinguish between different vegetation types. The effects of these three implementations were analyzed for soil moisture and evaporation in offline experiments forced with ERA5 atmospheric forcing.

The interannually varying land cover locally altered the model evaporation and soil moisture. In regions with major land cover changes, such as the Amazon, the model evaporation fluxes and soil moisture responded consistently, capturing the effects of increased or decreased high or low vegetation cover. The interannually varying LAI led to significant improvements of the correlation coefficients computed with the available reference data on near-surface soil moisture and evaporation. This was specifically true in semiarid regions with predominantly low vegetation during the dry season. The interannually varying LAI and effective vegetation cover allow for an adequate representation of soil moisture–evaporation feedback by activating the couplings with vegetation during vegetation-water-stressed periods (Fig. 2.17). From these results, we conclude that it is essential to realistically represent interannual variability of LAI and to include the exponential relation between LAI and effective vegetation cover to correctly capture land–atmospheric feedbacks during droughts in HTESSEL. The developments of the effective vegetation cover parameterization considerably improved the spatial and temporal variability of the model effective vegetation cover and regionally reduced the model errors of evaporation and near-surface soil moisture. Overall, our results emphasize the need to represent spatial and temporal vegetation variability in LSMs used for climate reanalyses and near-term climate predictions. In climate predictions, we obviously cannot rely on satellite retrievals, and therefore the development and validation of dynamical or statistical models able to reliably predict vegetation dynamics, from leaf to ecosystem scales, remain an important challenge for the future in the land surface modeling community.

3

CLIMATE-CONTROLLED ROOT ZONE PARAMETERS IN LAND SURFACE MODELS

In the previous chapter we focused on aboveground vegetation characteristics in a land surface model, and found considerable effects of interannual vegetation variability on the performance of modeled interannual water dynamics. This chapter focuses on the belowground part of the vegetation, of which spatial and temporal variability are also not adequately represented in most land surface models. Here, we investigate the potential for climate-controlled root zone parameters for improving modeled water dynamics in a land surface model.

This chapter is based on:

3

SUMMARY

The root zone storage capacity (S_r) is the maximum volume of water in the subsurface that can potentially be accessed by vegetation for transpiration. It influences the seasonality of transpiration as well as fast and slow runoff processes. Many studies have shown that S_r is heterogeneous as controlled by local climate conditions, which affect vegetation strategies in sizing their root system able to support plant growth and to prevent water shortages. Root zone parameterization in most land surface models does not account for this climate control on root development and is based on lookup tables that prescribe the same root zone parameters worldwide for each vegetation class. These lookup tables are obtained from measurements of rooting structure that are scarce and hardly representative of the ecosystem scale. The objective of this research is to quantify and evaluate the effects of a climate-controlled representation of S_r on the water fluxes modeled by the Hydrology Tiled ECMWF Scheme for Surface Exchanges over Land (HTESSEL) land surface model. Climate-controlled S_r is estimated here with the "memory method" (MM) in which S_r is derived from the vegetation's memory of past root zone water storage deficits. $S_{r,MM}$ is estimated for 15 river catchments over Australia across three contrasting climate regions: tropical, temperate and Mediterranean. Suitable representations of $S_{r,MM}$ are implemented in an improved version of HTESSEL (Moisture Depth – MD) by accordingly modifying the soil depths to obtain a model $S_{r,MD}$ that matches $S_{r,MM}$ in the 15 catchments. In the control version of HTESSEL (CTR), $S_{r,CTR}$ is larger than $S_{r,MM}$ in 14 out of 15 catchments. Furthermore, the variability among the individual catchments of $S_{r,MM}$ (117–722 mm) is considerably larger than of $S_{r,CTR}$ (491–725 mm). The climate-controlled representation of S_r in the MD version results in a significant and consistent improvement of the modeled monthly seasonal climatology (1975–2010) and interannual anomalies of river discharge compared with observations. However, the effects on biases in long-term annual mean river discharge are small and mixed. The modeled monthly seasonal climatology of the catchment discharge improved in MD compared to CTR: the correlation with observations increased significantly from 0.84 to 0.90 in tropical catchments, from 0.74 to 0.86 in temperate catchments and from 0.86 to 0.96 in Mediterranean catchments. Correspondingly, the correlations of the interannual discharge anomalies improve significantly in MD from 0.74 to 0.78 in tropical catchments, from 0.80 to 0.85 in temperate catchments and from 0.71 to 0.79 in Mediterranean catchments. The results indicate that the use of climate-controlled $S_{r,MM}$ can significantly improve the timing of modeled discharge and, by extension, also evaporation fluxes in land surface models. On the other hand, the method has not been shown to significantly reduce long-term climatological model biases over the catchments considered for this study.

3.1 INTRODUCTION

Root zone storage capacity S_r is an essential component of land surface hydrology as it controls the amount and timing of vegetation transpiration. However, most LSMs rely on a inadequate representation of the vegetation's root zone (Chapter 1), resulting in uncertainties in modeled water fluxes. Direct observations of S_r at scales larger than plot scale do not exist and, therefore, several indirect methods have been developed to estimate S_r from other observable ecosystem characteristics considering optimality principles (Kleidon, 2004; Gao et al., 2014; Speich et al., 2018; Dralle et al., 2020a). One of these methods is the memory method, a term coined in this thesis, but also referred to as water balance method (Nijzink et al., 2016; Hrachowitz et al., 2021) or mass curve technique (Gao et al., 2014; Zhao et al., 2016). This method allows to estimate S_r based on root zone water deficits arising from the phase shift between the seasonal signals of precipitation and evaporation, here defined as the total of transpiration, soil evaporation, and interception evaporation, following the terminology proposed by Savenije (2004) and Miralles et al. (2020). This approach is based on evidence that root systems of present-day vegetation are a legacy that reflects the memory of past water deficits during dry spells. Vegetation has efficiently adapted the extent of its root system to past water deficits with a specific memory (i.e. the dry spell return period) to guarantee continuous access to water to satisfy canopy water demand, but no more than that (Savenije and Hrachowitz, 2017). Numerous studies have successfully demonstrated the potential of the memory method to provide estimates of climate controlled S_r for river catchments based on discharge data (Gao et al., 2014; De Boer-Euser et al., 2016), as well as on larger scales based on remotely sensed estimates of evaporation (Wang-Erlandsson et al., 2016; Singh et al., 2020; McCormick et al., 2021; Stocker et al., 2023). In addition, the method proved valuable to track the temporal evolution of S_r due to changing hydro-climatic conditions (Bouaziz et al., 2022) and human interventions, such as forest management (Nijzink et al., 2016; Hrachowitz et al., 2021).

However, climate-controlled root zone parameters have not yet been widely incorporated in LSMs. The only LSM to our knowledge in which climate-controlled root zone parameters are used is the JSBACH3.2 model (Hagemann and Stacke, 2015) in which rooting depths are based on the optimization model of net primary production from Kleidon (2004).

The objective of this study is to quantify and evaluate the effects of a climate-controlled representation of S_r on the water fluxes modeled by the Hydrology Tiled ECMWF Scheme for Surface Exchanges over Land (HTESSEL) land surface model. Specifically, we will test the hypothesis that implementing the memory method S_r ($S_{r,MM}$) in HTESSEL can improve the modeled magnitude and timing of catchment discharge and evaporation fluxes. By applying the memory method for estimating ecosystem-scale S_r for use in LSMs, the first three limitations of using sparse root observations mentioned above can be overcome, but it should be acknowledged that, although the memory method in principle allows for adaptively updating S_r, in this work we use a fixed value in time. In this study, $S_{r,MM}$ values representative for the 1973–2010 time period are estimated for 15 Australian catchments across different climate regions (Sect. 3.2.3 and Appendix A). The $S_{r,MM}$ estimates are then used to constrain the S_r in HTESSEL (Sect. 3.2.5). Section 3.3 evaluates the effects on discharge and evaporation in HTESSEL by performing offline

simulations with and without the improved representation of S_r. Finally, in Sects. 3.4 and 3.5 the potential for a wider application of climate-controlled root zone parameters is discussed.

3.2 METHODS

3.2.1 STUDY AREA

Australia is characterized by large spatial differences in precipitation (Fig. 3.1), vegetation coverage and temperatures, varying from hot and dry deserts in the interior to tropical forests with a monsoon season in the north. We have selected 15 Australian river catchments with station observations of river discharge at the outlet of the catchment to estimate S_r by applying the memory method (Fig. 3.1; Supplementary material Table S3.1) (Australian Government Bureau of Meteorology, 2019). The catchments are selected based on available discharge data (at least 30 years of station observations), size (at least one-third of the land surface model grid cell area of approximately $5500\,\text{km}^2$ in order to spatially extrapolate catchment characteristics to grid cells) and differences in climate (spatial spread of the catchments across Australia for the analysis of different climate zones). The catchments are classified in three climate regions based on their hydrological characteristics (Table 3.1; Fig. 3.2; Supplementary material Table S3.2). The tropical catchments are characterized by pronounced seasonality of rainfall with a seasonality index of precipitation (I_S) of 0.7 or higher, while temperate and Mediterranean catchments have year-round rainfall ($I_S < 0.7$). The Mediterranean catchments are characterized by a time lag ϕ between long-term mean maximum monthly potential evaporation E_p and precipitation P of 5 or 6 months, while in tropical and temperate catchments mean maximum monthly E_p and P occur within 3 months.

Table 3.1: Average hydrological characteristics of the catchments in the three climate regions for the time period 1973–2010 with long-term mean annual discharge $\overline{Q}$, long-term mean annual precipitation $\overline{P}$, long-term mean annual potential evaporation $\overline{E}_p$, aridity index $I_A = \overline{E}_p/\overline{P}$, and the seasonality index of precipitation $I_S = \frac{1}{P_a}\sum_{m=1}^{m=12}|\overline{P_m} - \frac{\overline{P_a}}{12}|$, where $\overline{P_a}$ is the annual mean precipitation and $\overline{P_m}$ the monthly mean precipitation in month m (Gao et al., 2014); ϕ is the time lag between long-term mean maximum monthly precipitation (P) and potential evaporation (E_p). Values for all individual catchments are provided in Supplementary material Table S3.2.

Climate region	$\overline{Q}$ (mm yr^{-1})	$\overline{P}$ (mm yr^{-1})	$\overline{E}_p$ (mm yr^{-1})	I_A (–)	I_S (–)	ϕ (months)
Tropical (seven catchments)	302	1101	1869	2	0.9	2.3
Temperate (five catchments)	57	651	1488	2.5	0.2	0.6
Mediterranean (three catchments)	53	879	1276	1.7	0.3	5.7

3.2.2 DATA

For this study we use daily discharge data from station observations in the catchments for the time period 1973–2010 (Australian Government Bureau of Meteorology, 2019). For the same time period we use daily precipitation and daily mean temperature data from the GSWP-3 dataset on a regular 0.5°grid (Kim, 2017). Daily E_p is calculated by applying the Hargreaves and Samani formulation based on temperature and radiation
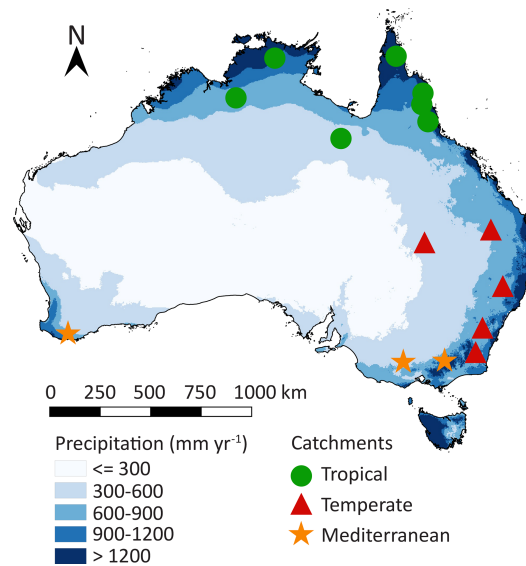
Figure 3.1: Location of the 15 study catchments within Australia. The green, red and orange markers indicate the climate region, and the blue shades indicate long-term mean annual precipitation (Australian Government Bureau of Meteorology, 2019). A list of the catchments and their characteristics is provided in Supplementary material Table S3.1.
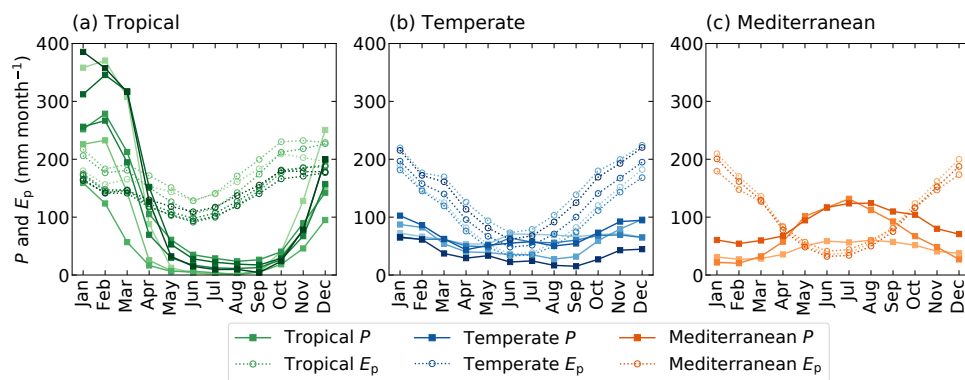

Figure 3.2: Monthly seasonal climatology of precipitation (P) and potential evaporation (E_p) for the **(a)** tropical, **(b)** temperate and **(c)** Mediterranean catchments, with the solid lines representing P and the dashed lines E_p, for the time series 1973–2010. The different shades indicate the 15 individual study catchments.

(Hargreaves and Samani, 1982; Mines ParisTech Solar radiation Data, 2016). The FLUX-COM RS + METEO dataset is used as a reference dataset to benchmark modeled actual evaporation. FLUXCOM provides a gridded product of interpolated monthly evaporation as a fusion of FLUXNET eddy covariance towers, satellite observations and meteorological data (GSWP-3) for the time period 1975–2010 (Jung et al., 2019). This dataset has shown plausible estimates of mean annual and seasonal evaporation and is generally

considered a suitable tool for global land model evaluations (Jung et al., 2019; Ma et al., 2020). However, we found considerable differences between the long-term annual mean evaporation $\overline{E}_{\text{FLUXCOM}}$ and $\overline{E}$ derived from the catchment water balance ($\overline{E}_{\text{WB}}$) based on observed Q and GSWP-3 P ($\overline{E}_{\text{WB}} = \overline{P} - \overline{Q}$) (Fig. 3.3). Figure 3.3 clearly illustrates that the $\overline{E}_{\text{FLUXCOM}}$ is consistently lower than $\overline{E}_{\text{WB}}$, with an average difference of 150 mm yr^{-1}, which is equivalent to about 20 % of the long-term water balances. $\overline{E}_{\text{WB}}$ is likely to be more reliable than $\overline{E}_{\text{FLUXCOM}}$ because $\overline{E}_{\text{WB}}$ provides an integrated catchment-scale estimate as it is derived from observations of Q assuming that the catchments are large enough to neglect deep groundwater drainage to or from other catchments (Bouaziz et al., 2018; Condon et al., 2020). In addition, $\overline{E}_{\text{FLUXCOM}}$ is based on point-scale estimates of FLUXNET stations that do not coincide with and are mostly located far from the study catchments (Pastorello et al., 2020). The discrepancy between the FLUXCOM and catchment water balance is addressed by scaling the monthly FLUXCOM evaporation:

$$E_{\text{FLUXCOM-WB}} = E_{\text{FLUXCOM}} \frac{\overline{E}_{\text{WB}}}{\overline{E}_{\text{FLUXCOM}}}, \tag{3.1}$$

with $E_{\text{FLUXCOM-WB}}$ as the monthly reference evaporation representative for the catchment scale, E_{FLUXCOM} from Jung et al. (2019) in the catchment corresponding grid cells and $\frac{\overline{E}_{\text{WB}}}{\overline{E}_{\text{FLUXCOM}}}$ the catchment-specific scaling factor.

We use gridded data on vegetation type and coverage derived from the GLCC1.2 (ECMWF, 2016) and soil texture data from the FAO/UNESCO Digital Soil Map of the World (FAO, 2003). Characteristics of the different soil textures are based on the Van Genuchten soil parameters (Van Genuchten, 1980). These data are needed as input to the HTESSEL model and for the estimation of S_{r}.
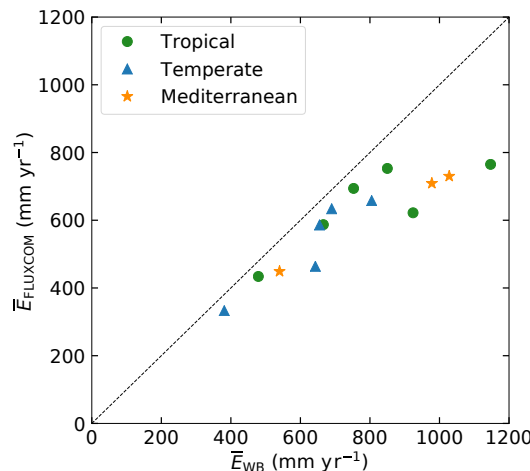

Figure 3.3: Long-term mean annual evaporation ($\overline{E}$) as estimated from long-term water balance data ($\overline{E}_{\text{WB}}$) compared to the FLUXCOM dataset ($\overline{E}_{\text{FLUXCOM}}$) for the 1975–2010 period.

3.2.3 MEMORY METHOD FOR ESTIMATING ROOT ZONE STORAGE CAPACITY

$S_{r,MM}$ is estimated based on catchment hydrometeorological data according to the methodology described in the studies of De Boer-Euser et al. (2016), Nijzink et al. (2016) and Wang-Erlandsson et al. (2016). $S_{r,MM}$ is based on an extreme value analysis of the annual maximum water storage deficits in the vegetation's root zone (S_d). S_d maximizes during dry periods, and therefore S_r represents an upper limit of root zone storage assuming that vegetation has sufficient access to water to overcome these dry periods. The cumulative water storage deficit S_d (mm) in the root zone is based on daily time series of effective precipitation P_e (mm d^{-1}) and transpiration E_t (mm d^{-1}) for the time period 1973–2010 and is described by

$$S_d(t) = \max\left(0, -\int_{t_0}^{\tau}(P_e - E_t)\mathrm{d}t\right),\tag{3.2}$$

with an integration from t_0 that corresponds to the first day in the hydrological year 1973 to τ that corresponds to the daily time steps ending on the last day of the hydrological year 2010. P_e (mm d^{-1}) is derived from the water balance of the interception storage S_i:

$$\frac{\mathrm{d}S_i}{\mathrm{d}t} = P - E_i - P_e,\tag{3.3}$$

with P representing the precipitation (mm d^{-1}) and E_i the interception evaporation (mm d^{-1}). Equation (3.3) can be solved by Eqs. (3.4)–(3.6). Herein, for the sum of fluxes between two time steps the following notation is used: $F_t = \int_{t-1}^{t} F\mathrm{d}t$, where F is either P, E_i, P_e or E_p (potential evaporation, mm d^{-1}). The numerical solution was then thus obtained as follows using daily time steps.

$$P_{e,t} = \begin{cases} 0 & \text{if } P_t + S_{i,t-1} \leq S_{i,max} \\ P_t + S_{i,t-1} - S_{i,max} & \text{if } P_t + S_{i,t-1} > S_{i,max} \end{cases}\tag{3.4}$$

$$S_{i,t}^* = S_{i,t-1} + P_t - P_{e,t}\tag{3.5}$$

$$E_{i,t} = \begin{cases} E_{p,t} & \text{if } E_{p,t} < S_{i,t}^* \\ S_{i,t}^* & \text{if } E_{p,t} \geq S_{i,t}^* \end{cases}\tag{3.6}$$

Here, $S_{i,max}$ is the maximum interception storage (mm) that depends on the land cover and is estimated between 2–8 mm for a tropical forest (Herwitz, 1985) and between 0–3 mm for a temperate forest (Gerrits et al., 2010). However, De Boer-Euser et al. (2016) found that the sensitivity of S_r to the value of $S_{i,max}$ is small, and therefore a value of 2.5 mm is used here in all catchments for simplicity.

Daily E_t (mm d^{-1}) in Eq. (3.2) was calculated by

$$E_t = c\,E_p,\tag{3.7}$$

where c (–) is a coefficient that represents the ratio between transpiration and potential evaporation $c = \overline{E_t}/\overline{E_p}$. $\overline{E_t}$ (mm yr^{-1}) is the long-term mean transpiration derived from the water balance ($\overline{E_t} = \overline{P_e} - \overline{Q}$) and $\overline{E_p}$ (mm yr^{-1}) the long-term mean potential evaporation. E_t considered here includes both transpiration and soil evaporation, but as the

latter is much smaller, we use the term transpiration for simplicity. The subtle inter-actions between atmospheric water demand and vegetation-available water supply can lead to interannual variability in c. The above-described approach that provided constant estimates of c is therefore extended by an iterative procedure to estimate annually varying values of the coefficient c as described in Appendix 3.A.

Catchment $S_{r,MM}$ (mm) is estimated based on the assumption that a catchment's ecosystem designs its rooting system while keeping memory of water stress events with certain return periods. Previous studies provide evidence that these return periods are likely to be longer for high vegetation (e.g., forest) than for low vegetation (e.g., grass). Based on the results of Gao et al. (2014), De Boer-Euser et al. (2016) and Wang-Erlandsson et al. (2016) drought return periods (RP) for high and low vegetation are set to 40 and 2 years, respectively. The $S_{r,MM}$ corresponding to these drought return periods is calculated by applying the Gumbel extreme value distribution (Gumbel, 1935) to annual maximum storage deficits. Theoretically we could treat S_r separately for high and low vegetation in HTESSEL. However, this would require changing the root distributions (see Sect. 2.4), which we decided not to do as we did not want to change multiple parameters at the same time. Therefore, for the implementation of $S_{r,MM}$ in HTESSEL, catchment $S_{r,MM}$ is estimated as a weighted sum of the high and low vegetation S_r based on the coverage fraction of high (C_H) and low (C_L) vegetation in the corresponding grid cell of that specific catchment, described by

$$S_{r,MM} = C_L\, S_{r,L,2yr} + C_H\, S_{r,H,40yr}. \tag{3.8}$$

3.2.4 HTESSEL MODEL DESCRIPTION

In this study we use the Hydrology Tiled ECMWF Scheme for Surface Exchanges over Land (HTESSEL) land surface model (Balsamo et al., 2009). This section presents the model parameterization of vegetated areas in the HTESSEL control model version (here-inafter CTR) based on the IFS documentation of cycle CY43R1 and the model code itself (ECMWF, 2016). The core structure of this model is described by van den Hurk et al. (2000), and major changes in the hydrology parameterization were made by Balsamo et al. (2009) with the implementation of a global soil texture map instead of a single soil type and a runoff scheme accounting for sub-grid variability, which resulted in improvements in global water budget simulations (Balsamo et al., 2011).

Figure 3.4a represents a simplified 3D view of a single grid cell. The HTESSEL model describes eight different surface fractions within a grid cell (ECMWF, 2016), but we only considered the vegetation-covered fractions (high and low vegetation) because of the presence of roots. Considering exclusively vegetated areas, the grid cell surface is sub-divided into high and low vegetation-covered area (C_H and C_L) with a dominant type of vegetation (T_H and T_L) based on the GLCC1.2 vegetation database. This database distinguishes 18 different vegetation types (e.g., evergreen broadleaf, tall grass, crops), each described with vegetation-specific parameters based on experiments and literature (e.g., minimum canopy resistance, root distribution). The subsurface has a single soil texture based on FAO (2003) and is subdivided into four model layers with a total depth z of 2.89 m that is kept uniformly constant in the global domain.

Figure 3.4b presents the connection of the subsurface with the surface through roots and transpiration fluxes (E_t) in more detail. S_r is not explicitly described in the model pa-
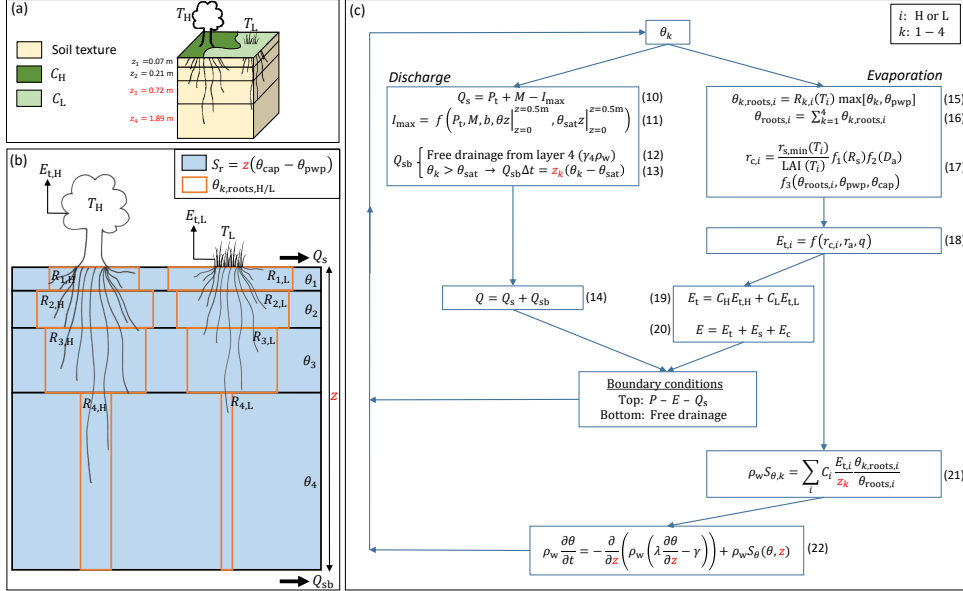
Figure 3.4: Root zone parameterization in the HTESSEL CTR version with the directly changed parameters in the HTESSEL MD version highlighted in red. **(a)** 3D overview of a single grid cell. **(b)** Schematic image of the four-layer subsurface. **(c)** Scheme of equations for the calculation of soil moisture, discharge and evaporation. The symbols in this figure are as follows, with i representing high (H) and low (L) vegetation and k layers 1–4: C (–) vegetation coverage, T dominant vegetation type, z (m) layer depth, P (m s^{-1}) precipitation, P_t (m s^{-1}) precipitation through-fall, M (m s^{-1}) snowmelt, Q (m s^{-1}) total discharge, Q_s (m s^{-1}) surface runoff, Q_{sb} (m s^{-1}) subsurface runoff, I_{max} (m s^{-1}) maximum infiltration rate, b (–) variable representing sub-grid orography, E (m s^{-1}) total evaporation, E_t (m s^{-1}) transpiration, E_s (m s^{-1}) soil evaporation, E_c (m s^{-1}) canopy evaporation, R (%) root distribution, θ (m^3 m^{-3}) unfrozen soil moisture, θ_{pwp} (m^3 m^{-3}) soil moisture at permanent wilting point, θ_{cap} (m^3 m^{-3}) soil moisture at field capacity, θ_{sat} (m^3 m^{-3}) soil moisture at saturation, S_r (m) the root zone storage capacity, θ_{roots} (m^3 m^{-3}) the root extraction efficiency, r_c (s m^{-1}) canopy resistance, r_a (s m^{-1}) atmospheric resistance, R_s (W m^{-2}) downward shortwave radiation, D_a (hPa) atmospheric water vapor deficit, q specific humidity (kg kg^{-1}), $r_{s,min}$ (s m^{-1}) minimum canopy resistance, LAI (–) leaf area index, S_θ (m^3 m^{-3} s^{-1}) root extraction rate, γ (m s^{-1}) hydraulic conductivity, λ (m^2 s^{-1}) hydraulic diffusivity and ρ_w (kg m^{-3}) density of water.

rameterization, and therefore it is formulated based on our own understanding of its relation to the HTESSEL vegetation and root zone parameterizations (Eq. 3.9). Vegetation has roots in all four model soil layers (except for the vegetation types desert and tundra that can only access the upper layer and the upper three layers, respectively; ECMWF, 2016). There is a variable root distribution across the layers that is different for each vegetation type. The vegetation-specific root distribution (R_k) describes the root fraction with respect to the total amount of roots in each model soil layer. At a single time step, the capability of roots to extract soil moisture ($\theta_{k,roots}$, represented by the brown boxes in 3.4b) is a function of R_k and the layer of unfrozen soil moisture content (θ_k). Thus, the more roots we have in a soil layer, the more moisture can be extracted at each time step. In the long term, however, the vegetation is able to extract all the plant-available soil moisture in the layers where roots are present. Therefore, $S_{r,CTR}$, represented in blue

in Fig. 3.4b, is described by

$$S_{r,CTR} = z(\theta_{cap} - \theta_{pwp}), \tag{3.9}$$

with z representing the hydrologically active depth, which corresponds to the combined depth of all soil layers with roots ($z = 2.89$ m is a default value in HTESSEL for all vegetation types except for desert and tundra), and $\theta_{cap} - \theta_{pwp}$ the plant-available moisture, which is constant over the four soil layers. The plant-available moisture is bounded by the soil-texture-specific moisture contents at field capacity (θ_{cap}), above which soil moisture drains by gravity, and at the wilting point (θ_{pwp}), below which soil moisture is not accessible to roots. It should be noted that we aimed for a physical definition of $S_{r,CTR}$ but that the effective water used by vegetation may be different. We come back to this point more elaborately in the Discussion section (Sect. 3.4.3).

Figure 3.4c presents the equation scheme of HTESSEL for calculating soil moisture as well as discharge and evaporation fluxes, with i representing high (H) or low vegetation cover (L) and k the four soil layers. The relative soil moisture content θ controls the calculations of discharge and evaporation fluxes. The surface runoff (Q_s) is defined by the precipitation through-fall (P_t), snowmelt (M) and maximum infiltration rate (I_{max}) (Eq. 10). I_{max} is a function of P_t, M, a spatially variable parameter (b) that is defined by the standard deviation in sub-grid orography, and the vertically integrated (top 0.5 m) soil moisture (θ) and saturation soil moisture (θ_{sat}) (Eq. 11) (Dümenil and Todini, 1992; van den Hurk and Viterbo, 2003). The subsurface runoff (Q_{sb}) consists of two components: free drainage from layer 4, which is a function of hydraulic conductivity in this layer (γ_4) and water density (ρ_w) (Eq. 12), and the excess absolute soil moisture when $\theta_k > \theta_{sat}$ (Eq. 13). Total discharge (Q) is the sum of Q_s and Q_{sb} (Eq. 14), and as typical in-stream travel times through the catchments are about 1 d at most, we did not consider routing to be important at the monthly timescale for which we analyze the results. The average root extraction efficiency in all layers (θ_{roots}) is described by Eqs. (15) and (16) as the weighted sum of the vegetation-specific R_k and θ_k. The canopy resistance (r_c) (Eq. 17) describes the resistance of vegetation to transpiration and is a function of vegetation-specific values for minimum canopy resistance ($r_{s,min}$) and LAI, a function of shortwave radiation ($f_1(R_s)$), a function of atmospheric water vapor deficit ($f_2(D_a)$) and a function of the root extraction efficiency ($f_3(\theta_{roots,i}, \theta_{pwp}, \theta_{cap})$). The canopy resistance defines $E_{t,i}$ together with specific humidity (q) and an atmospheric resistance term (r_a) (Eq. 18). Total E_t is a weighted sum of the separate transpiration products based on the sub-grid coverage C_L and C_H (Eq. 19), and total evaporation (E) is a sum of transpiration (E_t), soil evaporation (E_s) and canopy evaporation (E_c) fluxes (Eq. 20). The detailed formulations of the latter two fluxes are not relevant in this study and are therefore not included in this model description. $E_{t,i}$ is attributed to the different soil layers in the calculation of the root extraction (S_θ) based on the layer depth (z_k) and $\theta_{k,roots}$ (Eq. 21). The change in soil moisture over time ($\partial\theta/\partial t$) is calculated by applying the Darcy–Richards equation with γ and λ representing hydraulic conductivity and diffusivity (Eq. 22). This equation is solved with a top soil boundary condition of $P - E - Q_s$ and a bottom soil boundary condition of free drainage.

3.2.5 IMPLEMENTATION OF MEMORY METHOD ROOT ZONE STORAGE CAPACITY ESTIMATES IN HTESSEL

Here we develop an approach to implement the climate-controlled $S_{r,MM}$ (results in Sect. 3.3.1) in HTESSEL, while maintaining the modeling framework of the CTR model described in Sect. 3.2.4. We found that $S_{r,CTR}$ is exclusively defined by the soil type and the hydrologically active model soil depth (z) (Eq. 3.9). In our modified version of HTESSEL, hereafter referred to as the Moisture Depth (MD) model, the soil depth for moisture calculations is changed to satisfy the following equation:

$$S_{r,MM} = z_{MD}(\theta_{cap} - \theta_{pwp}), \tag{3.23}$$

with z_{MD} as the total soil depth in the MD model modified to satisfy $S_{r,MD} = S_{r,MM}$. This depth change is achieved by changing model layer 4, except in the case that this would cause the model depth of layer 4 to approach zero ($z_4 \approx 0$). In this case a minimum threshold (0.2 m) is set for z_4, and the depth of layer 3 is further changed to obtain $S_{r,MD} = S_{r,MM}$ as required in Eq. (3.23). This is necessary because $z_4 \approx 0$ in the moisture calculation would cause inconsistencies in the thermal diffusion calculations as the layer soil temperature is a function of the layer soil moisture. The layer depths for thermal diffusion calculations are not modified in the MD model, and we found that the soil layer temperatures are insensitive to depth changes in MD. The directly changed parameters in MD are highlighted in red in Fig. 3.4. Also, the root distribution is not modified in MD because we aimed for a physical representation of S_r (Eq. 3.23) and we did not want to change multiple model parameters at the same time. Furthermore, we would like to reiterate that the soil depth in the model should be interpreted neither as actual soil depth nor rooting depth, but merely as a way to represent the plant-accessible water volume.

3.2.6 MODEL SIMULATIONS

Simulations are performed in a stand-alone version of HTESSEL (Balsamo et al., 2009) as it was implemented in the framework of version 3 of the EC-EARTH Earth system model (http://www.ec-earth.org, last access: August 2020) for both the CTR (Sect. 3.2.4) and MD (Sect. 3.2.5) model versions. The model is forced with 3-hourly GSWP-3 atmospheric boundary conditions (Kim, 2017) for the historical time series 1970–2010, with the first 5 years used for spin-up. The spatial resolution of the HTESSEL model is a reduced Gaussian grid (N128), with the grid cells over Australia being approximately 5500 km^2.

3.2.7 MODEL EVALUATION

Most study catchments are smaller than single HTESSEL grid cells (Supplementary material Table S3.1). For catchments completely falling within a single HTESSEL grid cell, this cell is selected for analysis. In the case that a catchment falls within more than one grid cell, the average of the model output in the separate grid cells is used for analysis. The model performances of CTR and MD are compared based on modeled monthly discharge and evaporation fluxes for 1975–2010: long-term annual means, monthly seasonal climatology and interannual anomalies of monthly fluxes (monthly fluxes minus monthly climatology) are evaluated. Modeled Q is compared to station observations and

modeled E to the FLUXCOM-WB evaporation (Sect. 3.2.2 and Eq. 3.1). For long-term annual means, the percent bias between the reference and modeled fluxes is calculated (evaporation p bias $= (\overline{E}_{\mathrm{mod}} - \overline{E}_{\mathrm{ref}})/\overline{E}_{\mathrm{ref}}$). For the monthly seasonal climatology and interannual anomalies, the model performance is quantified by using the Pearson correlation coefficient (r) and a variability performance metric ($\nu = (1 - \alpha)^2$) that depends on the ratio of modeled and reference standard deviation ($\alpha = \sigma_{\mathrm{mod}}/\sigma_{\mathrm{ref}}$). These performance metrics are calculated for the individual catchments and then averaged to evaluate model performance over tropical, temperate and Mediterranean climate regions.

To test the significance of the improvement in model performance of MD compared to CTR, a Monte Carlo bootstrap method (1000 repetitions) is employed. The 1000 samples are taken by randomly resampling with replacement among CTR and MD values at each time step. The null hypothesis of getting as high or higher performance parameters simply by chance is tested at the 5 % and 10 % significance levels for the individual catchments as well as for the performance averages over the tropical, temperate and Mediterranean climate regions. P values of the model improvements are provided in Supplementary material Tables S3.5-S3.8.

3.3 RESULTS

3.3.1 ROOT ZONE STORAGE CAPACITY ESTIMATES

Figure 3.5 shows that there is no relation between $S_{\mathrm{r,MM}}$ and $S_{\mathrm{r,CTR}}$. The range of $S_{\mathrm{r,MM}}$ (125–722 mm) in the study catchments is much larger than the range of $S_{\mathrm{r,CTR}}$ (491–725 mm), indicating that HTESSEL may not adequately represent the spatial heterogeneity of S_{r} (Supplementary material Table S3.2). The range of $S_{\mathrm{r,MM}}$ in the catchments is consistent with Wang-Erlandsson et al. (2016), who found similar ranges of S_{r} (approximately 100–600 mm) over Australia by using gridded products of S_{r} based on rooting depths from observations and optimized inverse modeling, and they also found similar ranges of global $S_{\mathrm{r,MM}}$ estimated based on satellite evaporation products. $S_{\mathrm{r,MM}}$ estimates are on average smaller in the five temperate (194 mm) catchments than in the three Mediterranean (321 mm) and the seven tropical (437 mm) catchments. In the tropical and Mediterranean regions vegetation needs to bridge extensive dry seasons as rainfall seasonality is high (Fig. 3.2, Table 3.1), resulting in larger $S_{\mathrm{r,MM}}$ than in temperate regions with year-round precipitation. In the Mediterranean, the average time lag between P and E_{p} of 5.7 months results in large root zone storage deficits in the hot and dry summers and therefore larger $S_{\mathrm{r,MM}}$ than in the temperate catchments.
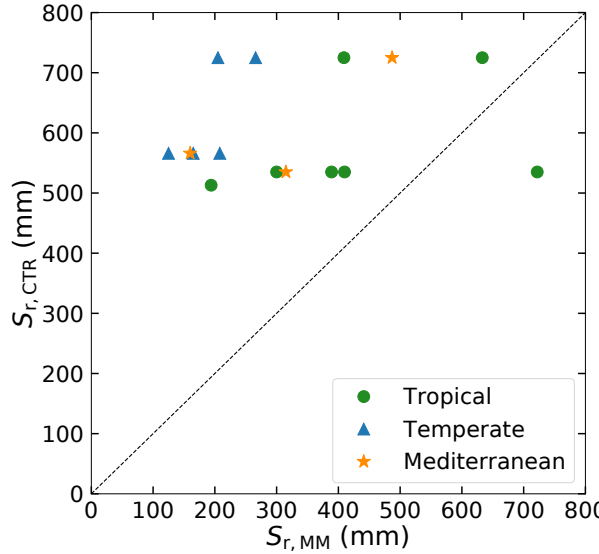
Figure 3.5: Catchment S_r as estimated from the memory method ($S_{r,MM}$) compared to the HTESSEL CTR parameterization ($S_{r,CTR}$) in the catchment corresponding grid cells.

3.3.2 LONG-TERM MEAN ANNUAL CLIMATOLOGY

The HTESSEL CTR version overestimates observed $\overline{Q}$ in 9 out of 15 catchments with on average 40 mm yr^{-1} (tropical), 3 mm yr^{-1} (temperate) and 122 mm yr^{-1} (Mediterranean) (Tables 3.2, Supplementary material Tables S3.3 and S3.4). This overestimation of observed Q goes together with an average underestimation of $\overline{E}_{WB}$ by CTR. As $S_{r,MM}$ is generally smaller than $S_{r,CTR}$ (Fig. 3.5), the MD version results in reduced $\overline{E}$ and increased $\overline{Q}$ compared to CTR, but the changes are quite small (Table 3.2). The MD increase in modeled $\overline{Q}$ compared to CTR results on average in larger p biases in tropical (+16.9 % vs. +13.7 %), temperate (+24.4 % vs. +4.9 %) and Mediterranean (+263.8 % vs. +249.9 %) catchments, but the results are largely variable among the individual catchments (Supplementary material Table S3.4).

Table 3.2: Long-term annual mean modeled discharge ($\overline{Q}$) and evaporation ($\overline{E}$) in the HTESSEL CTR and MD versions for the tropical, temperate and Mediterranean climate regions (catchment averages) as well as reference $\overline{Q}$ (station observations) and $\overline{E}$ ($\overline{E}_{WB}$, Sect. 3.2.2). The p biases of the modeled climate region average $\overline{Q}$ and $\overline{E}$ are presented between brackets. Similar values for the individual catchments are shown in Supplementary material Tables S3.3 and S3.4.

Climate region	Observations	$\overline{Q}$ (mm yr^{-1}) HTESSEL CTR	HTESSEL MD	WB	$\overline{E}$ (mm yr^{-1}) HTESSEL CTR	HTESSEL MD
Tropical	291	331 (+13.7 %)	345 (+18.6 %)	834	790 (−5.3 %)	776 (−7.1 %)
Temperate	56	59 (+4.9 %)	70 (+24.4 %)	626	624 (−0.4 %)	611 (−2.4 %)
Mediterranean	49	171 (+249.9 %)	177 (+263.8 %)	836	717 (−14.2 %)	709 (−15.2 %)

3.3.3 MONTHLY SEASONAL CLIMATOLOGY

Although $\overline{Q}$ does not considerably change in MD compared to CTR (Sect. 3.3.2), MD reproduces the seasonal variations in Q considerably better than CTR (Fig. 3.6a–c and Table 3.3). In the tropical and Mediterranean catchments, MD increases Q in the wet months, while it decreases Q in the dry months compared to CTR and hence improves the seasonal timing of observed Q (Fig. 3.6a, c and Table 3.3). In the temperate catchments, MD increases Q in the wet months (July–September) compared to CTR in accordance with observations, although in the other months the changes in MD compared to CTR are mixed (Fig. 3.6b). In terms of the correlation between modeled and observed monthly seasonal climatology, Q improved in MD compared to CTR in 12 out of 15 catchments, with 7 catchments passing the 5 % significance level for improvement (Supplementary material Table S3.5). For the climate region averages, the correlation significantly improved in MD from 0.84 to 0.90 (tropical), from 0.74 to 0.86 (temperate) and from 0.86 to 0.96 (Mediterranean) compared to CTR (Table 3.3). On average, MD resulted in larger variations in monthly Q than CTR (Fig. 3.6a–c). The variability term $\nu = (1 - \sigma_{\mathrm{mod}}/\sigma_{\mathrm{obs}})^2$ improved from 0.17 to 0.06 (tropical) and from 0.17 to 0.10 (temperate) in MD compared to CTR, but in the Mediterranean catchments the models strongly overestimate the observed variations in Q (Fig. 3.6c), with the variability term increasing from 2.80 in CTR to 8.73 in MD (Tables 3.3 and Supplementary material Table S3.5).

In contrast to the improvement in the monthly seasonal climatology of Q in MD, the monthly seasonal cycle of E appears not to be significantly affected, as shown in Fig. 3.6d–f and Table 3.3.

Table 3.3: Model performance parameters of monthly seasonal discharge (Q) and evaporation (E) climatologies (1975–2010), with r representing Pearson correlation and $\nu = (1 - \alpha)^2$ variability (where $\alpha = \sigma_{\mathrm{mod}}/\sigma_{\mathrm{obs}}$), in tropical, temperate and Mediterranean climate regions for the HTESSEL CTR and MD versions (catchment averages). Modeled Q is compared to station observations and modeled E to FLUXCOM-WB (Eq. 3.1). For r, a value of 1 represents a perfect model; for ν a value of 0 represents a perfect model. The significance test of the MD improvements compared to CTR is represented by ** (passing the 5 % level) and * (passing the 10 % level). Values of r and α for the individual catchments and p values of improvement are shown in Supplementary material Tables S3.6 (Q) and S3.8 (E).

| Climate region	HTESSEL version	Discharge		Evaporation	
		r (–)	ν (–)	r (–)	ν (–)
Tropical	CTR	0.84	0.17	0.98	0.07
	MD	0.90**	0.05**	0.98	0.07
Temperate	CTR	0.74	0.17	0.99	0.04
	MD	0.86**	0.10**	0.98	0.05
Mediterranean	CTR	0.86	2.80	0.81	0.08
	MD	0.96*	8.73	0.80	0.07
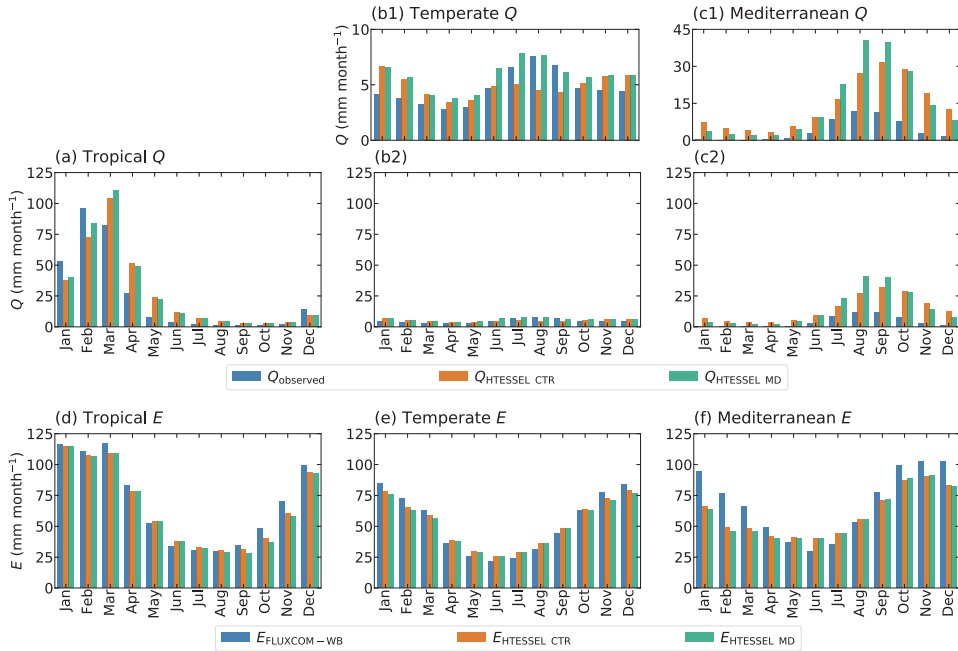
Figure 3.6: Monthly seasonal climatology of observed discharge (Q) **(a–c)** and FLUXCOM-WB evaporation ($E_{\text{FLUXCOM-WB}}$) **(d–f)** as well as modeled values in the HTESSEL CTR and MD versions, averaged for the tropical **(a, d)**, temperate **(b, e)** and Mediterranean **(c, f)** catchments for the time series 1975–2010. Labels **(b1)** and **(c1)** represent the same data as in **(b2)** and **(c2)**, but with a different y axis. Similar illustrations for the individual catchments are shown in Supplementary material Figs. S3.1 (Q) and S3.2 (E).

3.3.4 INTERANNUAL MONTHLY ANOMALIES

Figure 3.7a and c show that MD is better in capturing the variations in interannual Q anomalies than CTR in the presented tropical and temperate catchments, while in the Mediterranean catchment both models strongly overestimate the interannual Q anomalies compared to observations (Fig. 3.7e). In 14 out of 15 catchments, the variability in the interannual Q anomalies increases in MD compared to CTR (Supplementary material Fig. S3.1 and Table S3.6). This results in an average improvement in the interannual anomaly variability (v) from 0.12 to 0.11 (tropical) and from 0.09 to 0.06 (temperate) in MD compared to CTR (Table 3.4). However, in the Mediterranean catchments, the increased variability in the Q anomalies leads to a strong overestimation of Q anomalies with respect to observations (Figs. 3.7e and S1m–o), with v increasing from 0.99 in CTR to 4.26 in MD. Figure 3.7a, c and e also show that the timing of the Q anomalies improves in MD compared to CTR; in particular, the improved timing of the falling limbs is clearly visible in Fig. 3.7a and e. The interannual Q anomaly correlation (corresponding to the timing) improves in 14 out of 15 catchments, with 9 catchments passing the 5 % significance level for improvement (Table S3.5). On average, the correlation (r) increases from 0.74 to 0.78 (tropical), from 0.80 to 0.85 (temperate) and from 0.71 to 0.79 (Mediterranean) in MD compared to CTR. In contrast to the improvement in the interannual Q

anomalies in MD, the interannual E anomalies do not considerably change compared to CTR (Fig. 3.7b, d and f; Tables 3.4 and Supplementary material S3.8).
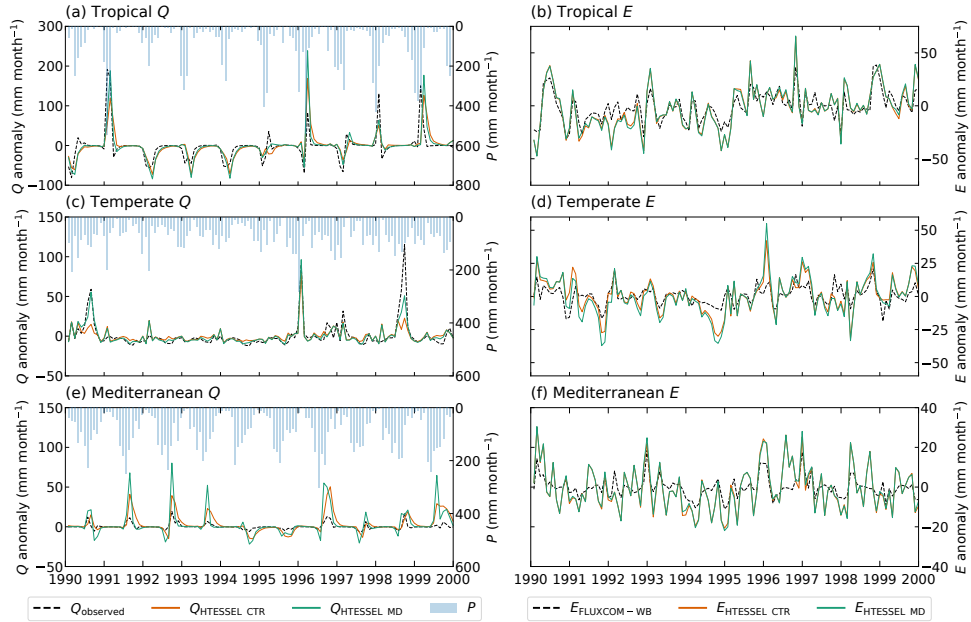

Figure 3.7: Interannual monthly anomalies of observed discharge (Q) **(a, c, e)** and FLUXCOM-WB evaporation (E) **(b, d, f)** fluxes as well as modeled values in the HTESSEL CTR and MD versions in an individual representative tropical (catchment Mi) **(a, b)**, temperate (catchment Na) **(c, d)** and Mediterranean (catchment K) **(e, f)** catchment based on the time series for 1975–2010. Similar illustrations for the individual catchments are shown in Supplementary material Figs. S3.1 (Q) and S3.2 (E).

Table 3.4: Model performance parameters of interannual monthly discharge (Q) and evaporation (E) anomalies (1975–2010), with r representing Pearson correlation and $\nu = (1 - \alpha)^2$ variability (where $\alpha = \sigma_{\mathrm{mod}}/\sigma_{\mathrm{obs}}$), in tropical, temperate and Mediterranean climate regions for the HTESSEL CTR and MD versions (catchment averages). Modeled Q is compared to station observations and modeled E to FLUXCOM-WB (Eq. 3.1). For r, a value of 1 represents a perfect model; for ν a value of 0 represents a perfect model. The significance test of the MD improvements compared to CTR is represented by $**$ (passing the 5 % level) and $*$ (passing the 10 % level). Values of r and α for the individual catchments and p values of improvement are shown in Supplementary material Tables S3.6 (Q) and S3.8 (E).

Climate region	HTESSEL version	Discharge		Evaporation	
		r (–)	ν (–)	r (–)	ν (–)
Tropical	CTR	0.74	0.12	0.79	1.39
	MD	0.78**	0.11	0.80**	1.52
Temperate	CTR	0.80	0.09	0.81	1.12
	MD	0.85**	0.06*	0.82**	1.46
Mediterranean	CTR	0.71	0.99	0.78	1.17
	MD	0.79**	4.26	0.78	1.31

3.4 DISCUSSION

3.4.1 SYNTHESIS OF RESULTS

$S_{r,MM}$ is lower than $S_{r,CTR}$ in 14 out of 15 catchments (Fig. 3.5). This is seemingly in contrast to literature suggesting that the root depth in land surface models is too low and that the absence of deep roots is a cause for uncertainties in simulated evaporation (Kleidon and Heimann, 1998; Pan et al., 2020; Sakschewski et al., 2020). However, S_r represents a conceptual water volume that is accessible to roots without defining where this volume is in reality. Therefore, it is not necessarily proportional to root depth as a small S_r does not preclude the presence of deep roots, as illustrated in Fig. 4 in Singh et al. (2020).

The modeling results show that the difference in long-term mean $\overline{Q}$ and $\overline{E}$ fluxes between CTR and MD are small (Table 3.2), whereas the differences between monthly (climatological and interannual) variations are clearly visible (Figs. 3.6 and 3.7). This corresponds to other studies on catchment hydrology that suggest that the root zone storage mainly affects the fast hydrological response of a catchment (Oudin et al., 2004; Euser et al., 2015; Nijzink et al., 2016; De Boer-Euser et al., 2016). Furthermore, previous studies found larger improvements in modeled discharge using $S_{r,MM}$ in humid regions with large rainfall seasonality (De Boer-Euser et al., 2016; Wang-Erlandsson et al., 2016). This is not found in our study, as we obtain slightly smaller improvements in the discharge correlation for the tropical catchments than for the temperate and Mediterranean ones. This is at least partly related to the smaller difference between $S_{r,MM}$ and $S_{r,CTR}$ in the tropical catchments than in temperate and Mediterranean ones (Fig. 3.5). The Mediterranean catchments have large climatological biases and overly large discharge variability in the seasonal cycle and interannual anomalies in CTR, and MD further degrades the performance with respect to bias and variability (Tables 3.2–3.4). On the other hand, the correlation of seasonal climatology and interannual anomalies consistently improves in all climate regions with the implementation of $S_{r,MM}$. Therefore, it is suggested that aspects of the hydrology parameterization other than S_r (e.g., the lack of a groundwater layer) could be primarily leading to the large climatological biases and overly large discharge variability in the seasonal cycle and interannual anomalies in the Mediterranean. On the other hand, uncertainties in the GSWP-3 forcing could also partly cause the large biases in the Mediterranean. In this climate region, it is found that GSWP-3 $\overline{P}$ (0.5°grid) is considerably larger than $\overline{P}$ from the SILO dataset, which provides P on a 0.05°grid directly derived from ground-based observational data (Jeffrey et al., 2001).

Although we found significant differences in modeled Q between CTR and MD, the discrepancy in E was very limited in all climate regions (Tables 3.3, 3.4 and Supplementary material S3.7-3.8; Supplementary material Fig. S3.2). As stated before, the reliability of the FLUXCOM E is questionable in our study catchments (Fig. 3.3). Although the model performance with respect to E fluxes is uncertain, the lack of evaporation sensitivity to S_r was unexpected and requires more in-depth evaluation of the results in view of the HTESSEL model parameterization.

In order to further explain the evaporation (in)sensitivity, we analyzed the modeled soil moisture and specifically looked at a wet period (mid-1990) and a dry period (beginning of 1991) in a temperate catchment, as shown in Fig. 3.8b. During the wet period, soil moisture in the upper three layers is above or close to θ_{cap} for both MD and CTR, while in the fourth layer MD has larger soil moisture than CTR. In this case evaporation

is not moisture-limited and controlled by the top three layers because of the larger root distribution in these layers (Eqs. 14 and 15). Therefore, the modeled transpiration is not sensitive to the increase in layer 4 soil moisture in MD compared to CTR. During the transition from wet to dry periods, the upper three layers dry out first as there is a reduction in precipitation input. As these layers are relatively dry, evaporation is controlled by the fourth layer in which θ is reduced to values close to θ_{pwp} in MD, while it remains relatively wet in CTR. It is this difference in θ_4 that causes the sensitivity of transpiration in MD during the wet-to-dry transition. However, most of the time the modeled soil moisture is in the wet and insensitive regime, and therefore the overall effect of MD on modeled evaporation tends to be small in the catchments considered in this study. To further analyze the evaporation sensitivity to S_{r} changes, it would be useful to evaluate to what extent it is model-dependent and compare HTESSEL behavior with other LSMs in a multi-model context (e.g., van den Hurk et al., 2016; Ardilouze et al., 2017). On the other hand, we also expect the evaporation sensitivity to S_{r} to be related to the methodology applied, which will be further discussed in Sect. 3.4.3.

3.4.2 METHODOLOGICAL LIMITATIONS

Although the catchments were selected carefully, their location and sizes do not completely match the HTESSEL grid cells. Thus, assuming a one-to-one relation between precipitation, evaporation, river discharge and root zone storage capacities at the catchment and the grid cell is a potential source of error. However, this configures as ran-
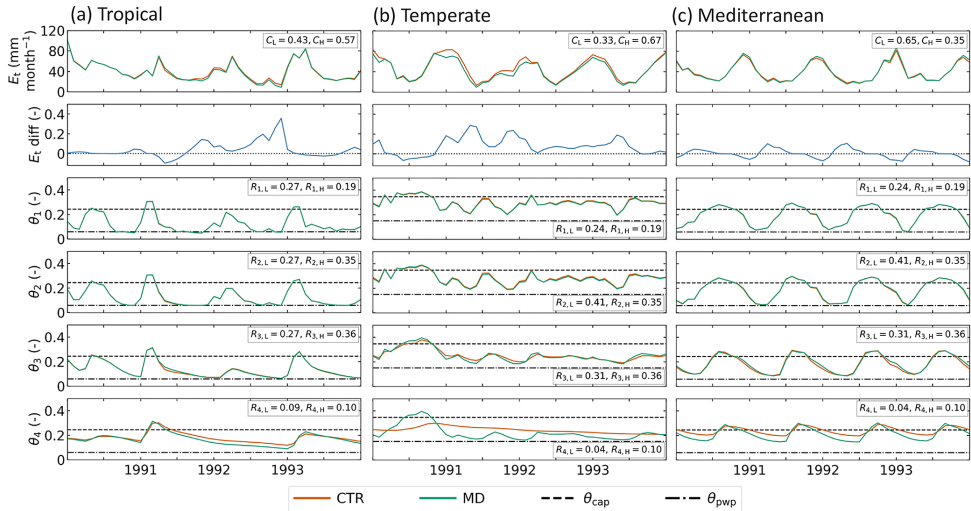
Figure 3.8: Modeled transpiration and soil moisture content in the HTESSEL CTR and MD versions in an individual representative tropical (catchment Mi) **(a)**, temperate (catchment Na) **(b)** and Mediterranean (catchment K) **(c)** catchment. From top to bottom: transpiration, relative difference between CTR and MD transpiration ($\frac{E_{\mathrm{t,CTR}}-E_{\mathrm{t,MD}}}{E_{\mathrm{t,CTR}}}$), soil moisture layer 1, soil moisture layer 2, soil moisture layer 3, soil moisture layer 4. Additionally, the vegetation coverage (C_{L} and C_{H}) and the relative rooting distribution (R_k) for the dominant high and low vegetation types are presented.

dom error and is therefore likely to cancel out in multiple catchment settings as is done in this study. Another source of uncertainty is the parameterization of the memory method for estimating catchment S_r. This method requires estimations of maximum interception storage, seasonal and interannual transpiration signals, and return periods, which lead to differences in $S_{r,MM}$ when other values are chosen. A sensitivity analysis of $S_{r,MM}$ with a high $S_{r,MM}$ ($S_{i,max}$ = 1.5 mm, RP_{low} = 3 years, RP_{high} = 60 years, f = 0.15; see Appendix A) and a low $S_{r,MM}$ ($S_{i,max}$ = 3.5 mm, RP_{low} = 1.5 years, RP_{high} = 20 years, f = 0.35) on average deviated 45 mm from the average $S_{r,MM}$ estimates used in this study ($S_{i,max}$ = 2.5 mm, RP_{low} = 2 years, RP_{high} = 40 years, f = 0.25). This deviation is small considering the average $S_{r,MM}$ of 319 mm. In addition, irrigation, as a possible external water source in catchments with crops (Supplementary material Table S3.1), and deep groundwater, as a water source for deep-rooting vegetation, are not accounted for in the approach. However, we think that the estimation of transpiration is the main uncertainty in the approach. The assumption that the seasonal variations in E_t and E_p are in phase may not hold in Mediterranean regions where E_p and P, and thereby the water available for transpiration, tend to be out of phase. Applying the seasonal pattern of transpiration modeled by CTR to the memory method in Mediterranean catchments results in smaller $S_{r,MM}$ estimates in these catchments (average: 292 mm) than with the initial approach whereby the seasonality of E_t was based on E_p (average: 321 mm). The relatively low deviation for both the parameter uncertainty and the uncertainty in the timing of E_t leads us to conclude that these assumptions have a small impact on the general finding that $S_{r,MM}$ is lower than $S_{r,CTR}$ and that HTESSEL does not represent the spatial heterogeneity of S_r. Station observations of river discharge are used in both the $S_{r,MM}$ estimation and the model evaluation. However, because the memory method is only based on observations of long-term annual mean discharge ($\overline{Q}$) and the model evaluation is mainly based on the monthly seasonal and interannual variations in Q, we consider model evaluation based on these data appropriate.

3.4.3 ROOT ZONE STORAGE CAPACITY IMPLEMENTATION

The HTESSEL CTR version does not explicitly formulate S_r, and therefore we formulate $S_{r,CTR}$ based on the root zone parameterization as presented in Sect. 3.2.4 in order to modify the model parameters in a way to make the model consistent with the $S_{r,MM}$ estimates. This formulation represents the theoretical $S_{r,CTR}$, but it may not fully correspond to the soil moisture in the four layers that is actually used by the modeled vegetation. The effective S_r ($S_{r,CTR,eff}$) can be derived a posteriori from the modeled soil moisture storage deficits and an extreme value analyses as done in the memory method (Sect. 3.2.3). $S_{r,CTR,eff}$ is smaller than $S_{r,CTR}$ based on depths (Supplementary material Fig. S3.3c), which is likely related to the relatively small root percentage in layer 4 compared to the other layers for most vegetation types (ECMWF, 2016). On the other hand, the $S_{r,MM}$ we implemented in MD by changing soil depths is close the $S_{r,MD,eff}$ based on modeled soil moisture deficits in MD (Supplementary material Fig. S3.3d).

In MD the depths for soil moisture calculations are changed, directly resulting in changes in absolute soil moisture and thereby in indirect changes in discharge and transpiration. This modification is relatively simple and flexible, and there is no limitation on the possible range of soil depths for moisture calculations, so it could therefore sim-

ilarly be implemented in other land surface models. However, it should be noted that this strategy chosen for changing the HTESSEL S_r is not the only one possible. As follows from Eq. (3.9), the plant-available soil moisture ($\theta_{cap} - \theta_{pwp}$) also defines the S_r. However, modifications in the model's θ_{cap} or θ_{pwp} are not desired as these parameters are soil-texture-specific properties. Moreover, modifications in the formulations of the root-available moisture for each time step (θ_{roots}) appear not to be conceptually meaningful.

There are several alternative hypotheses that may potentially explain the limited sensitivity of modeled E to the modified S_r. First, the resistance of vegetation to transpiration is a function of the moisture supply (soil moisture) and the moisture demand (atmospheric condition) (Eqs. 14–16). The atmospheric conditions, which define moisture demand and thereby constrain transpiration, are similar in both CTR and MD because the models are run in an offline version. Therefore, the soil moisture–atmosphere feedback is not represented and the moisture demand side dominates the moisture supply side in the evaporation calculations. This issue could be overcome by using coupled climate simulations. Second, although S_r is changed in MD compared to CTR, the parameterization of the vegetation water stress is kept constant. Ferguson et al. (2016) found that different formulations of root water uptake considerably influence modeled water budgets, and therefore it is likely that changes in evaporation in MD compared to CTR are constrained by the vegetation water stress formulations (Eqs. 14–16). Third, the insensitivity of evaporation to the changes in model soil depth is probably also related to the fact that the resistance of vegetation to transpiration is a function of the relative soil moisture (θ), which is not directly affected by changing the soil depth. On the other hand, soil depth changes directly affect the modeled Q, as modeled surface (Q_s) and subsurface runoff (Q_{sb}) directly depend on the absolute moisture storage capacity of the soil (see Eqs. 10 and 12), with Q_s being a function of the absolute moisture in the top 50 cm of soil and Q_{sb} a function of the total excess soil moisture when the layer's moisture content exceeds saturation moisture content. Fourth, monthly fluxes of Q are often a full order of magnitude smaller than E. Hence, small changes in the partitioning simply add up to larger relative changes for Q.

3.5 CONCLUSIONS

This study is an attempt to overcome major limitations in the representation of the vegetation's root zone in land surface models. Specifically, we looked at the HTESSEL land surface model and found that the root zone storage capacity S_r is only a function of soil texture and soil depth, the latter being kept constant over the modeled global domain (in HTESSEL $z = 2.89$ m), while from the state-of-the-art literature (e.g., Collins and Bras, 2007; Guswa, 2008; Gentine et al., 2012; Gao et al., 2014) it is indicated that S_r is, to a large extent, climate-controlled. We found that the HTESSEL control version (CTR) indeed does not adequately represent the spatial heterogeneity of S_r, with the range of $S_{r,CTR}$ (491–725 mm) much narrower than the range obtained for the climate-controlled estimate $S_{r,MM}$ (125–722 mm) in 15 Australian catchments with contrasting climate characteristics considered in this study. Furthermore, $S_{r,CTR}$ was found to be considerably larger than the climate-controlled estimate $S_{r,MM}$ in 14 out of 15 catchments. It is noted that these findings could be different for other LSMs when they have shallower soil depths.

We developed a new version of HTESSEL by suitably modifying the soil depths (MD) to obtain modeled $S_{r,MD}$ that matches $S_{r,MM}$ over the 15 catchments considered over Australia, while maintaining the overall HTESSEL model setup (Fig. 3.4). This strategy to modify the model's S_r is relatively simple and could similarly be implemented in other land surface models. Moreover, the applied methodology could allow for a time-varying S_r in LSMs, and hence all four limitations of using sparse root observations mentioned in Chapter 1 could be overcome.

The comparison of the offline simulations with original (CTR) and modified (MD) versions of HTESSEL shows that the difference of the biases in the modeled long-term mean climatology of discharge and evaporation fluxes is generally small. On the other hand, the seasonal timing of the discharge flux is significantly improved in MD, indicating the beneficial effect of the climate-controlled representation of S_r. Consistently, MD improves the correlation with observations for the monthly seasonal climatology of discharge fluxes in 12 out of 15 catchments (with 7 catchments passing the 5 % significance level) and for the interannual monthly discharge anomalies in 14 out of 15 catchments (with 9 catchments passing the 5 % significance level) (Supplementary material Tables S3.5-S3.6). Considering the climate region averages, the correlations of monthly seasonal climatology significantly improve in MD compared to CTR from 0.843 to 0.902 (tropical), from 0.741 to 0.855 (temperate) and from 0.860 to 0.951 (Mediterranean). The averaged correlations of the interannual monthly anomalies significantly improve in MD compared to CTR from 0.741 to 0.778 (tropical), from 0.795 to 0.847 (temperate) and from 0.705 to 0.785 (Mediterranean). Surprisingly, the modeled evaporation is shown to be relatively insensitive to changes in S_r. In HTESSEL evaporation only depends on the relative moisture content in each soil layer, which in the model is not directly affected by the depth of the soil. Investigation of this insensitivity showed that it is only sensitive during dry periods when evaporation is dominated by transpiration from the fourth layer (Fig. 3.8). On the other hand, surface runoff and subsurface runoff in HTESSEL depend on the total moisture content of the soil at any given time. Other than the relative moisture content this depends on the absolute moisture storage capacity of the soil that will vary together with the change in soil depth. Moreover, small changes in absolute fluxes translated to larger relative changes for runoff compared to evaporation (Fig. 3.6). As a final conclusion, we believe that a global application of climate-controlled root zone parameters has the potential to improve the timing of modeled water fluxes by land surface models, but from the results of this study a significant reduction of annual mean climatological biases cannot be expected. More work will be needed in the future to improve long-term mean simulations of discharge and evaporation fluxes by exploiting station-based and latest-generation satellite observations. Toward this aim the use of coordinated multi-model frameworks for the intercomparison of state-of-the-art LSMs could be fundamental.

3

3.A Iterative procedure for transpiration estimation

Daily transpiration is estimated by Eq. (3.7) with c, a coefficient that represents the ratio between transpiration and potential evaporation (Sect. 3.2.3). With $c = \overline{E_t}/\overline{E_p}$ as a constant value, we do not account for interannual variability in transpiration caused by the interplay between atmospheric water demand and vegetation-available water supply. Therefore, we add an iterative procedure to estimate annually varying values for c, which is described here.

Steps 1 to 6 describe the procedure used to estimate c, with step 1 providing the initial estimates and steps 2 to 6 executed iteratively. i represents the iterations (0–9) and a the hydrological years (1973–2010). P_e, E_t, E_p and S_d are daily values. After 10 iterations ($i = 9$) the resulting annual transpiration estimates stabilized and the corresponding storage deficits were used for the Gumbel S_r analysis as described in Sect. 3.2.3.

1. Create initial estimates ($i = 0$) of E_t and S_d with a constant $c_{0,a} = \overline{E_t}/\overline{E_p}$ for $a = 1973$–2010.

$$E_{t,0} = c_{0,a} E_p \tag{3.24}$$

$$S_{d,0} = \max\left(0, -\int_{1973}^{2010} (P_e - E_{t,0})\mathrm{d}t\right) \tag{3.25}$$

2. Calculate the annual change in storage in the root zone (S) with t_0 and t_1 representing the start and end of a hydrological year.

$$\Delta S_{i,a} = S_{d,i}(t_0) - S_{d,i}(t_1) \tag{3.26}$$

3. Calculate annual transpiration following the water balance.

$$\overline{E}_{t,i,a} = \overline{P}_{e,i,a} - \overline{Q}_{i,a} - \frac{\Delta S_{i,a}}{t_1 - t_0} \tag{3.27}$$

4. Calculate c_a for each hydrological year based on the annual E_t estimate from step 3 and calculate daily E_t.

$$c_{i,a} = \frac{\overline{E}_{t,i,a}}{\overline{E}_{p,a}} \tag{3.28}$$

$$E_{t,i} = c_{i,a} E_p \tag{3.29}$$

5. Calculate storage deficits based on daily E_t from step 4.

$$S_{d,i} = \max\left(0, -\int_{1973}^{2010} (P_e - E_{t,i})\mathrm{d}t\right) \tag{3.30}$$

6. The input storage deficit of iteration $i + 1$ in step 2 is the average of iteration i and $i - 1$.

$$S_{d,i+1} = \frac{S_{d,i} + S_{d,i-1}}{2} \tag{3.31}$$

The following three constraints are set to the iterations.

- The long-term water balance closes $(\overline{P}_e - \overline{Q} - \overline{E}_t \approx 0)$.

- Annual transpiration is always larger than zero and smaller than the annual potential evaporation.

- Variations in c are limited by $c_{0,a} - f\,c_{0,a} < c_{i,a} < c_{0,a} + f\,c_{0,a}$, with f as a coefficient set to 0.25.

Figure 3.9 illustrates the iterative approach for storage deficit calculations. Daily P, E_p and E_t based on Eq. (3.24) are presented in Fig. 3.9a. Figure 3.9b shows annual variations of P_e and E_t. During the years 1980–1984, P_e is clearly less than average, and the $E_{t,0}$ estimate is likely too high in these years because vegetation has less water available for transpiration. The final iteration $E_{t,9}$ provides a more realistic interannual pattern of transpiration. Initial and final iteration storage deficits are presented in Fig. 3.9c.
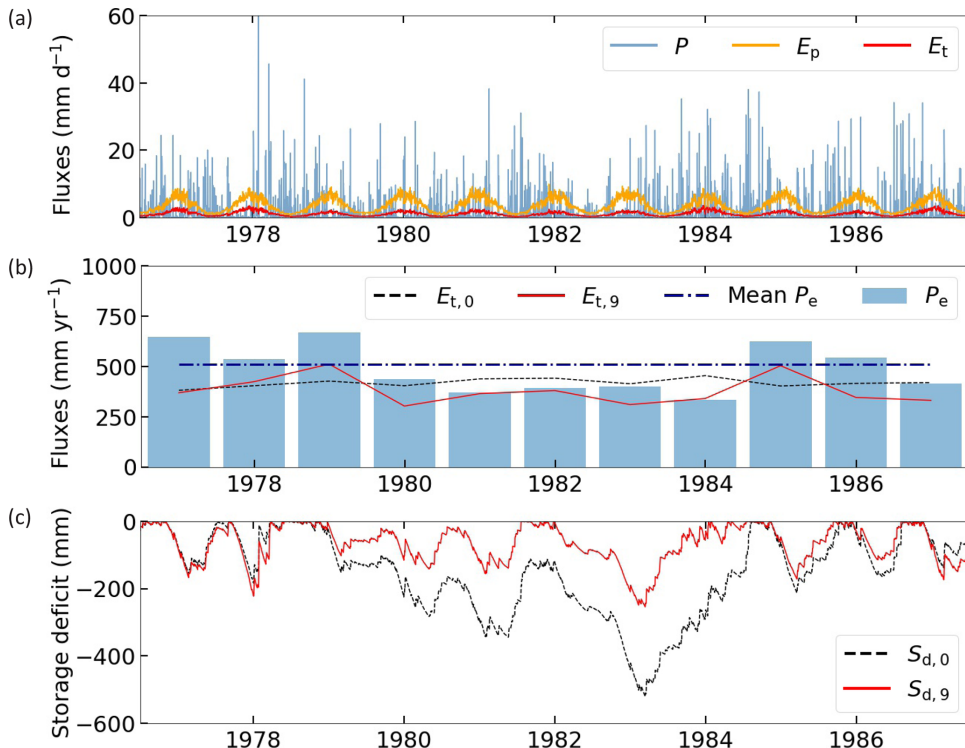
Figure 3.9: Storage deficit iteration approach in a temperate catchment for the time period 1977–1987. **(a)** Daily water fluxes with P representing precipitation, E_p potential evaporation and E_t the initial transpiration calculation based on Eq. (3.7). **(b)** Annual water fluxes with P_e representing effective precipitation, $E_{t,0}$ the initial transpiration estimate and $E_{t,9}$ the final iteration transpiration estimate. Mean P_e is based on the full time period (1973–2010). **(c)** Daily storage deficit with $S_{d,0}$ representing the initial calculation and $S_{d,9}$ the final iteration.

4

INFLUENCE OF IRRIGATION ON ROOT ZONE STORAGE CAPACITY ESTIMATION

In the previous chapter we have shown that climate-controlled root zone parameters based on the memory method have potential to improve water flux simulations by land surface models. One limitation of this method as it was used in Chapter 3, is the lack of consideration of irrigation as an external water source to the vegetation. This chapter addresses this issue by evaluating the influence of irrigation on root zone storage capacity estimation with the memory method for a large sample of catchments globally.

SUMMARY

Vegetation plays a crucial role in regulating the water cycle through transpiration, which is the water flux from the subsurface to the atmosphere via vegetation roots. The amount and timing of transpiration is controlled by the interplay of seasonal energy and water supply. The latter strongly depends on the size of the root zone storage capacity (S_r) which represents the maximum accessible volume of water that vegetation can use for transpiration. S_r is primarily influenced by hydro-climatic conditions as vegetation optimizes its root system in a way it can guarantee water uptake and overcome dry periods. S_r estimates are commonly derived from root zone water deficits that result from the phase shift between the seasonal signals of root zone water inflow (i.e., precipitation) and outflow (i.e., evaporation). In irrigated croplands, irrigation water serves as an additional input into the root zone. However, this aspect has been ignored in many studies, and the extent to which irrigation influences S_r estimates was never comprehensively quantified. In this study, our objective is to quantify the influence of irrigation on S_r and identify the regional differences therein. To this aim, we integrated two irrigation methods, based on irrigation water use and irrigated area fractions, respectively, into the S_r estimation. We evaluated the effects in comparison to S_r estimates that do not consider irrigation for a sample of 4856 catchments globally with varying degrees of irrigation activities. Our results show that S_r consistently decreased when considering irrigation with a larger effect in catchments with a larger irrigated area. For catchments with an irrigated area fraction exceeding 10 %, the median decrease of S_r was 19 mm and 23 mm for the two methods, corresponding to 12 % and 15 %, respectively. S_r decreased the most for catchments in tropical climates. However, the relative decrease was the largest in catchments in temperate climates. Our results demonstrate, for the first time, that irrigation has a considerable influence on S_r estimates over irrigated croplands. This effect is as strong as the effects of snow melt that were previously documented in catchments that have a considerable amount of precipitation falling as snow.

4.1 INTRODUCTION

Root zone storage capacity (S_r (mm)) can be estimated with the memory method (Chapter 3). In this method S_r is derived from water storage deficit calculations in the root zone at the catchment scale, assuming vegetation is able to keep memory of past deficit conditions to size roots in such a way to guarantee continuous access to water (Gentine et al., 2012; Gao et al., 2014). It is important to note that the memory method is based on liquid water input to the root zone. As such, solid phase precipitation and storage as transient, seasonal or perennial snow packs introduces time lags between the moment of precipitation and the release of liquid water (i.e., melt water) into the sub-surface. These time lags can lead to considerable temporal shifts in liquid water supply, thereby affecting the development of seasonal water deficits and the associated magnitudes of S_r. Various models with different levels of complexity have previously been integrated into the memory method to account for the time lags due to snow accumulation and melt dynamics (de Boer-Euser et al., 2018; Dralle et al., 2021; Stocker et al., 2023). Dralle et al. (2021) have recently shown that explicitly accounting for snow accumulation and associated time lags in melt water release in the memory method does generally lead to lower values of S_r in regions where significant fraction of precipitation occurs in the form of snow.

Irrigation similarly affects the timing of water input to the soil. Besides its effect on timing, irrigation during the growing season leads to input of additional water next to precipitation that otherwise would not be accessible for roots and thus not be available for vegetation uptake. Irrigation thereby also affects the magnitude of water input and actively shapes the root development of crops. Irrigation leads to shallower roots and higher root densities in the upper soil compared to non-irrigated vegetation, as it reduces the need for resource allocation for root growth, and instead allows increased resource allocation for above-surface growth (Klepper, 1991; Engels et al., 1994; Bakker et al., 2009; Maan et al., 2023). The strength of this signal is variable and depends on the irrigation method applied (Lv et al., 2010; Jha et al., 2017; Wang et al., 2020). Currently, approximately 20 % of global croplands are irrigated (FAO, 2022) and with the increasing demand for crop production, irrigation requirements are expected to increase in the future (Alexandratos and Bruinsma, 2012). In spite of some exceptions (e.g. Roodari et al. (2021)), irrigation is rarely systematically represented in hydrological and biogeophysical models (McDermid et al., 2023), mostly due to a lack of sufficient data (e.g., Meier et al. (2018)). This also holds for the memory method, as most studies using the memory method for S_r estimation did not account for irrigation, which likely led to an overestimation of S_r in irrigated areas (Gao et al., 2014; De Boer-Euser et al., 2016; Stocker et al., 2023). To our knowledge, only Wang-Erlandsson et al. (2016) explicitly accounted for irrigation when estimating S_r by adding irrigation estimates simulated by the LPJmL dynamic global vegetation model to the precipitation input (Jägermeyr et al., 2015). However, it remains unknown to which extent irrigation influences the magnitudes of S_r estimates and in which regions globally it is most relevant to take into account.

Our objective here is to quantify the influence of irrigation on the root zone storage capacity estimated with the memory method and to identify the regional differences therein. We do so by using a sample of 4856 catchments globally with varying degrees of irrigation activities. Specifically, we test the hypothesis that irrigation considerably

reduces root zone storage capacities S_r and therefore needs to be accounted for in the estimation of S_r. To this aim, we introduce two methods that represent irrigation based on catchment water balances to the memory method using irrigation data from two different sources. The first method explicitly uses estimates of irrigation water use from Zhang et al. (2022) in the S_r calculation with the memory method. The second method is a simpler parameterization based on the irrigated area fraction (Siebert et al., 2015).

4.2 Methods

4.2.1 Data

For this study we used station based discharge (Q) data from the following sources: the Global Streamflow Indices and Metadata Archive (GSIM) (Do et al., 2018; Gudmundsson et al., 2018), the Australian edition of the Catchment Attributes and Meteorology for Large-sample Studies (CAMELS-AUS) dataset (Fowler et al., 2021), the LArge-SaMple DAta for Hydrology and Environmental Sciences for Central Europe (LamaH-CE) (Klingler et al., 2021) and the Italian Hydrological Portal (Lendvai, 2020). We used annual mean discharge ($\overline{Q}$) for the catchment specific available time period. For the period 1981-2010, we obtained catchment average daily precipitation (P) and daily mean temperature (T_a) from the Global Soil Wetness Project Phase 3 (GSWP3) (Dirmeyer et al., 2006) and daily potential evaporation (E_p) from the Global Land Evaporation Amsterdam Model version 3.5a (GLEAMv3.5a), which is based on the Priestley-Taylor approach (Martens et al., 2017; Miralles et al., 2011). We selected 4856 catchments based on the following criteria: (1) at least 10 years of Q data during the 1981–2010 period; (2) catchment area $< 10000\,\mathrm{km^2}$ to limit the heterogeneity within catchments; (3) annual mean discharge ($\overline{Q}$) smaller than annual mean precipitation ($\overline{P}$) for the specific catchment.

For each catchment we obtained irrigation estimates from two different data sources. Firstly, we used the average irrigated area fraction I_a (-), which is the areal fraction of land equipped with infrastructure for irrigation. I_a was obtained from the "AEI_HYDE_FINAL_IR" dataset developed by Siebert et al. (2015), which is representative for the irrigation extent in the year 2005 (Fig. 4.1a). This dataset was based on sub-national irrigation statistics and the History Database of the Global Environment (HYDE) version 3.1 land use data (Klein Goldewijk et al., 2011; Siebert et al., 2015). Secondly, we used estimates of annual mean irrigation water use representative for the 2011-2018 period ($\overline{I_w}$ (mm year^{-1})) from Zhang et al. (2022), who developed an algorithm to estimate irrigation from multiple satellite-based products and the Priestley-Taylor Jet Propulsion Laboratory (PT-JPL) model (Fig. 4.1b).

To identify the effects of irrigation for different regions, we used the Köppen-Geiger climate classes as a climate indicator. We selected for each catchment the predominant Köppen-Geiger climate class based on a global map at a 1 km resolution representing the 1980-2016 period (Beck et al., 2018). The gridded data products for P, E_p, I_a and $\overline{I_w}$ were converted to catchment estimates using area weighted averages of the grid cells that lie for more than 50 % inside the catchment. Before area weighting, the gridded products were resampled to a spatial resolution of 0.05°using nearest neighbour interpolation. This way, all gridded products were treated similarly and problems with small catchments with no matching grid cells were avoided.
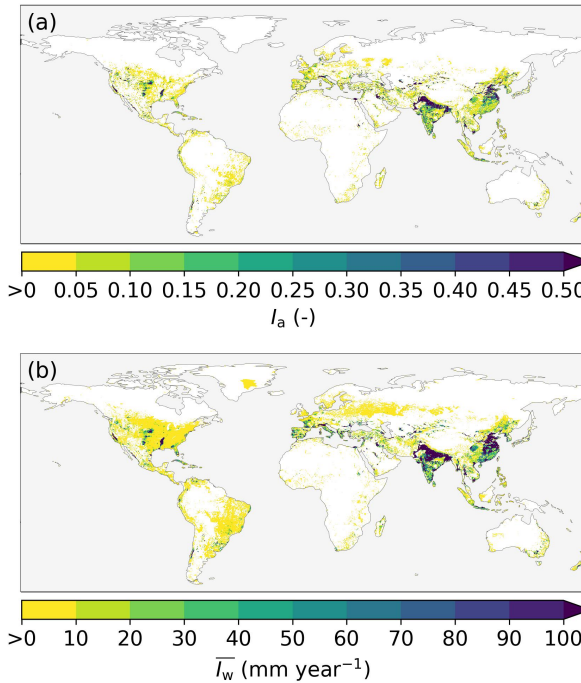
Figure 4.1: Global irrigation characteristics. (a) Irrigated area fraction (I_a (-)) representative for 2005 based on sub-national irrigation statistics and the HYDE 3.1 land use data (Siebert et al., 2015). (b) Annual mean irrigation water use ($\overline{I_w}$ (mm year^{-1})) for the period 2011-2018 based on multiple satellite-based products and the PT-JPL model (Zhang et al., 2022). White areas indicate I_a or $\overline{I_w}$ equal to zero.

4.2.2 MEMORY METHOD WITH IRRIGATION METHODS

Figure 4.2a shows a conceptualization of the memory method based on four storage components (mm): interception storage S_i, snow storage S_{sn}, "surplus" storage S_s, and storage deficit S_d. S_d is initially conceptualized as an infinite deficit storage volume and its temporal evolution can be described by:

$$S_d(t) = \int_{t_0}^{\tau} (P_e - E_t + I - P_s) \mathrm{d}t \qquad (4.1)$$

where P_e represents effective precipitation (mm day^{-1}), E_t is transpiration (mm day^{-1}), I is irrigation (mm day^{-1}), and P_s is surplus precipitation (mm day^{-1}) (Fig. 4.2a). In Eq. (4.1) t_0 corresponds to the first day of the first hydrological year and τ to the daily time steps ending on the last day of the last hydrological year. Our hydrological year starts the first day of the month after the wettest month, which is defined as the month with on average the largest positive difference between monthly mean P and E_p. At t_0, the starting point of the analysis, S_d=0. In Eq. (4.1), P_e (mm day^{-1}) is calculated from the water balance of the interception storage S_i (Fig. 4.2a), and E_t (mm day^{-1}) is described as a fraction of daily potential evaporation E_p (mm day^{-1}) based on the catchment water
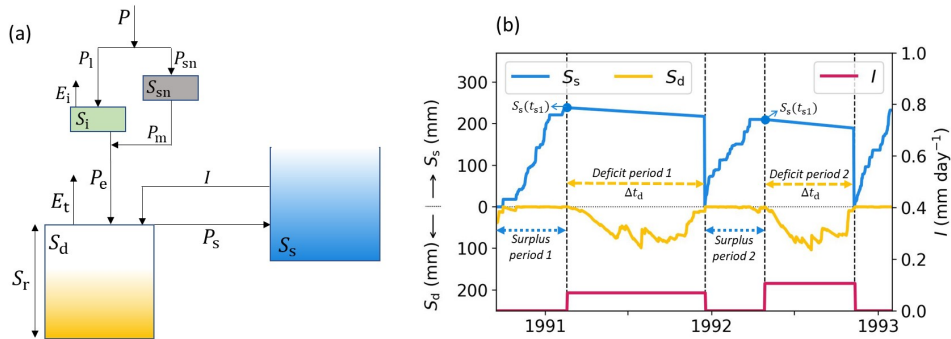
Figure 4.2: (a) Schematic bucket model representation of the memory method including an irrigation model with the following storages (mm): interception storage (S_i), snow storage (S_{sn}), storage deficit (S_d), surplus storage (S_s), and root zone storage capacity (S_r); and fluxes (mm day^{-1}): total precipitation (P), liquid precipitation (P_l), precipitation falling as snow (P_{sn}), snow melt (P_m), interception evaporation (E_i), effective precipitation (P_e), transpiration (E_t), precipitation surplus (P_s) and irrigation (I). (b) An example time series of S_s, S_d and I based on Eqs. (4.1–4.6), with Δt_d the length of the deficit period (days), and $S_s(t_{s1})$ the surplus storage at the end of the surplus period. Note that this time series represents only two years to illustrate the method, while all catchments have at least ten years of data.

balance. We used a simple snow model based on the degree-day method (e.g. Bergstrom, 1975; Gao et al., 2017) to account for the delay in liquid water input to the soil by describing liquid precipitation (P_l (mm day^{-1})), precipitation falling as snow (P_{sn} (mm day^{-1})), and snow melt (P_m (mm day^{-1})). The equations for the interception storage, snow storage, and transpiration calculation are described in Appendix 4.A.

Surplus precipitation P_s (mm day^{-1}) in Eq. (4.1) is described by Eq. (4.2), in which we used the following notation for the sum of the fluxes between two time steps: $F_t = \int_{t-1}^{t} F \, dt$, where F is either P_e, E_t, I or P_s. Thus $P_{s,t}$ is described by:

$$P_{s,t} = \max(0, S_d + P_{e,t} - E_{t,t} + I_t), \tag{4.2}$$

with S_d and I_t approaching zero during periods of abundant precipitation, and thus it then holds that $P_{s,t} \approx P_{e,t} - E_{t,t}$.

For the computation of applied irrigation I we split the timeseries into surplus and deficit periods (Fig. 4.2b). For each hydrological year, we defined one deficit period, which is the longest deficit period with the largest S_d in the hydrological year. Surplus periods were defined as the periods in between the deficit periods. For each surplus period, the surplus precipitation P_s (Eq. (4.2)) accumulates in the surplus store S_s:

$$S_s(t) = \max(0, \int_{t_{s0}}^{t_{s1}} (P_s - I) \, dt) \tag{4.3}$$

with t_{s0} the first day of the surplus period and t_{s1} the last day of the surplus period (Fig. 4.2b). S_s does not have a maximum storage capacity, but it is reset to zero each year, after each deficit period. This storage conceptualizes any water buffers that can be used for irrigation in the consecutive deficit period and may encompass ditches, lakes and

aquifers. This method assumes that irrigated water only originates from water inside the catchment boundaries and that it is sustainably extracted so that the long term water balance is closed. During a deficit period, the fraction of S_s that is used for irrigation is defined by irrigation factor f (-), which determines how much of the surplus water stored during the surplus period is used for irrigation during the consecutive deficit period. f represents both the water evaporated or discharged during the irrigation process before recharging the soil, and the spatial extent of the irrigation. It is assumed that daily irrigation I is equally distributed over the deficit period (Fig. 4.2b), so that I (mm day^{-1}) is defined as:

$$I(t) = \frac{f S_s(t_{s1})}{\Delta t_d} \tag{4.4}$$

with Δt_d the length of the deficit period $(t_{d1} - t_{d0})$ in days (Fig. 4.2b). Based on the two irrigation data sources used (Sect. 4.2.1), we have here developed two methods to estimate f in Eq. (4.4):

1. Irrigation Water Use method (IWU)

   $f_{d,\text{IWU}}$ (-) is defined for each deficit period d for each catchment by:

   $$f_{d,\text{IWU}} = \max(1, \frac{\overline{I_w}\,dt}{S_s(t_{s,1})}), \text{ so that } I(t) = \frac{\overline{I_w}\,dt}{\Delta t_d} \text{ if sufficient water is available in } S_s, \tag{4.5}$$

   with $\overline{I_w}$ (mm year^{-1}) the catchment annual mean irrigation water use, $dt = 1$ year, and $S_s(t_{s,1})$ (mm) the surplus storage at the end of the surplus storage accumulation period, i.e. the amount of water stored in S_s at the start of the deficit period. In this method, $f_{d,\text{IWU}}$ is different for each deficit period d, as S_s also varies. For each catchment, f_{IWU} is defined as the average $f_{d,\text{IWU}}$.

2. Irrigated Area Fraction method (IAF)

   f_{IAF} (-) is temporally non-varying, and is defined for each catchment by:

   $$f_{\text{IAF}} = \beta I_a \tag{4.6}$$

   with I_a (-) the catchment irrigated area fraction and β (-) a correction factor that is constant in space and time for all catchments. β was chosen as a constant to create a relatively simple approach that does not directly rely on irrigation water use data, which is beneficial for application in time periods (both historical and future), without irrigation water use data, as well as for regions where no reliable irrigation water use data is available. We estimated β by minimizing the difference between f_{IAF} and f_{IWU} in terms of Root Mean Squared Error (RMSE). We generated 1000 linearly spaced values for β between 0 and 2.5, and computed f_{IAF} for all the catchments. For all these cases, the RMSE of catchment f_{IAF} and f_{IWU} was computed (Fig. 4.3). The RMSE minimized for $\beta = 0.9$ (RMSE = 0.042), which is applied for all catchments in Eq. (4.6).

To evaluate the effect of these methods on estimated S_r we tested a third case, referred to as No Irrigation (NI), in which $f_{\text{NI}} = 0$. A priori we cannot and do not consider

any of the two methods, i.e., the IWU or the IAF method to be more representative than the other. While the IWU method uses the irrigation data more directly than the IAF method, the latter directly takes the inter-annual variability of surplus water into account.
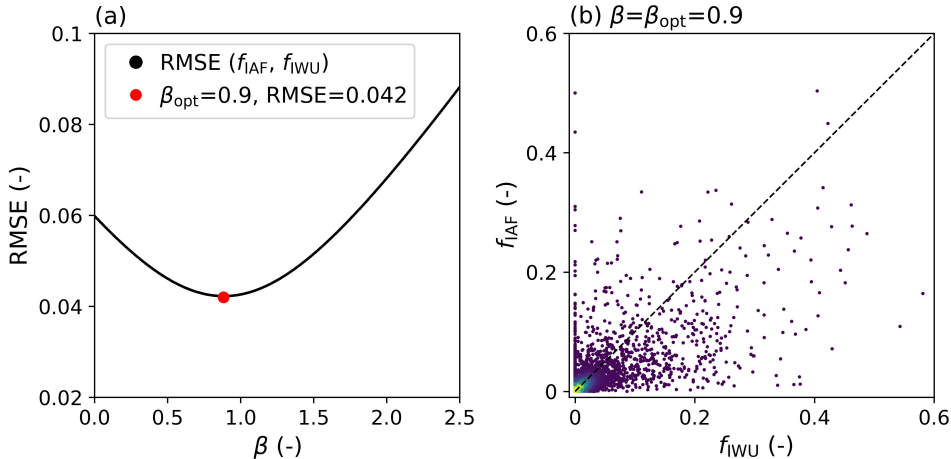

Figure 4.3: Root Mean Squared Error (RMSE) between the catchment irrigation factors f_{IWU} (Eq. 4.5) and f_{IAF} (Eq. 4.6) for 4856 catchments for 1000 linearly spaced values of β between 0 and 2.5. β_{opt} represents the value for β where the RMSE minimizes. (b) Scatter of f_{IWU} (Eq. 4.5) and f_{IAF} (Eq. 4.6) for $\beta=\beta_{opt}=0.9$ with lighter colours a higher point density.

ROOT ZONE STORAGE CAPACITY CALCULATION

Catchment-scale root zone storage capacity S_r was here derived from the catchment-scale storage deficit S_d timeseries for the three different irrigation cases NI, IWU, and IAF (Table 4.1). For each catchment, the annual maximum storage deficits ($S_{d,M}$) were defined for each hydrological year as:

$$S_{d,M} = \max(S_d(t)) - \min(S_d(t)) \tag{4.7}$$

with the $\min(S_d)$ occurring earlier in the hydrological year than the $\max(S_d)$. Previous studies (e.g. Gao et al., 2014; Wang-Erlandsson et al., 2016) applied a Gumbel distribution on the $S_{d,M}$ values to estimate S_r for different return periods T. Wang-Erlandsson et al. (2016) found that for croplands, and thus irrigated land, the best evaporation simulations with a global hydrological model were achieved with an S_r based on a return period of 2 years, as croplands adapt to survive droughts with relatively short return periods. Here, we directly used the observed $S_{d,M}$ values with occurrences closest to $T = 2$ years instead of a fitted extreme value distribution, because fitting an extreme value distribution is ambiguous for return periods of interest (here: 2 years) much smaller than the timeseries length (here: >10 years). For all catchments, for each irrigation case separately, the S_r was estimated as the mean of the three observed $S_{d,M}$-values with occurrences closest to $T = 2$ years, as represented by the cross-markers closest to the vertical dashed line at $T = 2$ years in in Fig. 4.5b,d,f and h.

EVALUATION

To visualize the effects of irrigation on S_d and S_r, we selected four example catchments with different irrigation magnitudes (i.e., I_a and $\overline{I_w}$) in four different continents and climate zones. For quantification of the effects of irrigation on S_r, we computed absolute (Δ) and relative (Δ_r) differences between the S_r estimates for the NI, IWU and IAF cases (Table 4.1). Catchments were stratified based on (1) four different ranges of irrigated area I_a: $I_a \leq 0.01$; $0.01 < I_a \leq 0.05$; $0.05 < I_a \leq 0.1$; and $I_a > 0.1$ (Supplementary material Fig. S4.1); (2) regions, i.e., South-America, North-America, Europe and Asia; and (3) climate zones based on Köppen-Geiger, subdivided into Tropical (Af, Am, Aw), Arid (BWh, BWk, BSh, BSk), Temperate (Cfa, Cfb, Cfc), Mediterranean (Csa, Csb), and Continental (Dfa, Dfb, Dfc, Dfd) climates, with the abbrevations of the Köppen-Geiger climate classification (Beck et al., 2018) (Supplementary material Fig. S4.2). Uncertainty of the differences in S_r were represented by the interquartile range (IQR).

Table 4.1: Details of the irrigation cases considered in this study.

Irrigation case	Details	Irrigation factor f (Eq. (4.4))
NI	No irrigation	$f_{NI} = 0$
IWU	Irrigation based on Irrigation Water Use (Fig. 4.1b)	$f_{IWU} = \max(1, \frac{\overline{I_w}\,dt}{S_s(t_{s,1})})$ (Eq. (4.5))
IAF	Irrigation based on Irrigated Area Fraction I_a (Fig. 4.1a)	$f_{IAF} = \beta I_a$ (Eq. (4.6))
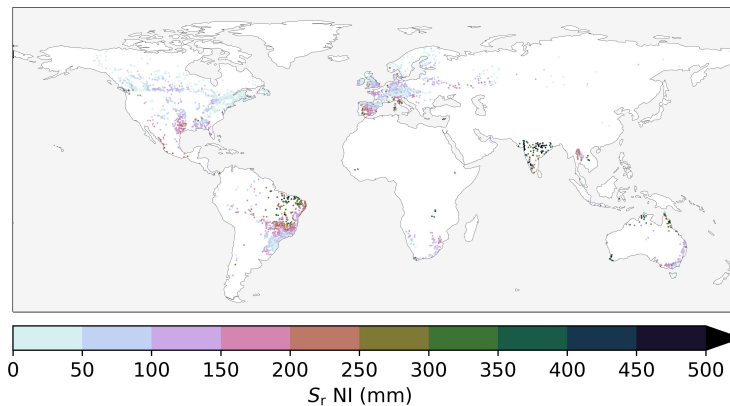
Figure 4.4: Catchment S_r for the No Irrigation (NI) case, with dots representing catchment outlets. Similar figures for the IWU and IAF cases are presented in Supplementary material Fig. S4.3.

4.3 RESULTS

4.3.1 IRRIGATION INFLUENCE ON ROOT ZONE STORAGE CAPACITY

Globally, the S_r estimates without accounting for irrigation ranged from 0–800 mm, with larger values in semi-arid regions with high rainfall seasonality such as North-Eastern Brazil (median $S_r \approx 250$ mm) or monsoon regions such as North-Eastern Indian (median $S_r \approx 450$ mm), than in regions with temperate climates with year-round rainfall such as Western Europe (median $S_r \approx 70$ mm) or continental, colder, climates such as Canada (median $S_r \approx 40$ mm) (Fig. 4.4).

The storage deficits S_d (Eq. 4.1) in general reduced when accounting for irrigation effects according to the IWU and IAF cases as compared to the case without irrigation
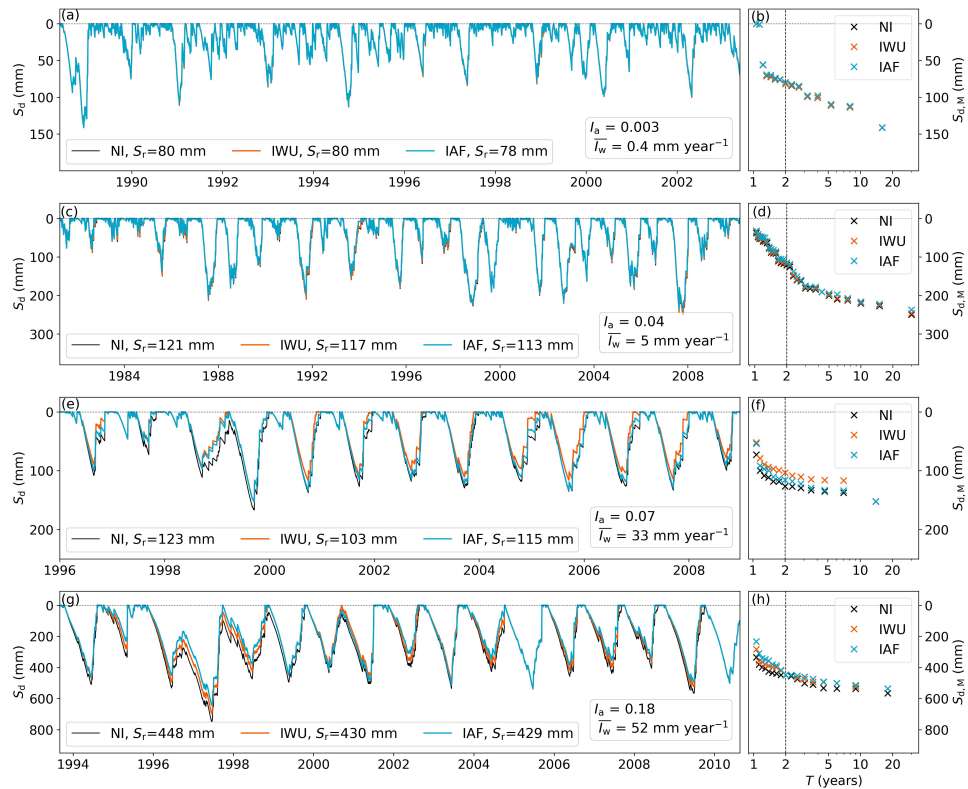
Figure 4.5: (a, c, e, g) Timeseries of storage deficits S_d (mm) (Eq. 4.1) for four illustrative catchments with increasing irrigation from top to bottom for the three irrigation cases NI, IWU, and IAF (Table 4.1) with for each catchment the associated annual mean irrigation water use ($\overline{I_w}$), irrigated area fraction (I_a), and root zone storage capacity (S_r) values. (b, d, f, h) Return level plot of annual maximum storage deficits ($S_{d,M}$) (Eq. 4.7) for the three irrigation cases NI, IWU and IAF with the dashed vertical line corresponding to a return period T of 2 years (Section 4.2.2). The locations of the catchments are shown in Fig. 4.6. Catchment identity, continent, and Köppen Geiger climate zone are from top to bottom: br_0002356, South America, temperate (Cfb); ca_0000689, North America, continental (Dfb); es_0000742, Europe, Mediterranean (Csa); in_0000252, Asia, tropical (Aw).

(NI). These overall effects of the method are illustrated by four selected example catchments in Fig. 4.5. More pronounced effects of irrigation on S_d are visible for the example catchments in Europe (Fig. 4.5e,f) and Asia (Fig. 4.5g,h), with larger $\overline{I_w}$ and I_a, than in the example catchments in South-America (Fig. 4.5a,b) and North-America (Fig. 4.5c,d). As S_d decreased, the annual maximum storage deficits $S_{d,M}$, as determined by Eq. (4.7), decreased as well. Consequently, the estimated S_r decreased for the IWU and IAF cases compared to NI, with more pronounced effects in the example catchments with larger $\overline{I_w}$ and I_a (Fig. 4.5). Globally, S_r consistently decreased for IWU and IAF (Fig. 4.6), albeit the magnitudes vary to a considerable extent. Nevertheless, relatively clear regional patterns of the effects of irrigation on S_r emerged. The most pronounced effects cluster in catchments in regions that are characterized by widespread and intense crop cultivation, and thus high irrigation water use, such as Northern Spain and France and parts of India (Fig. 4.1).
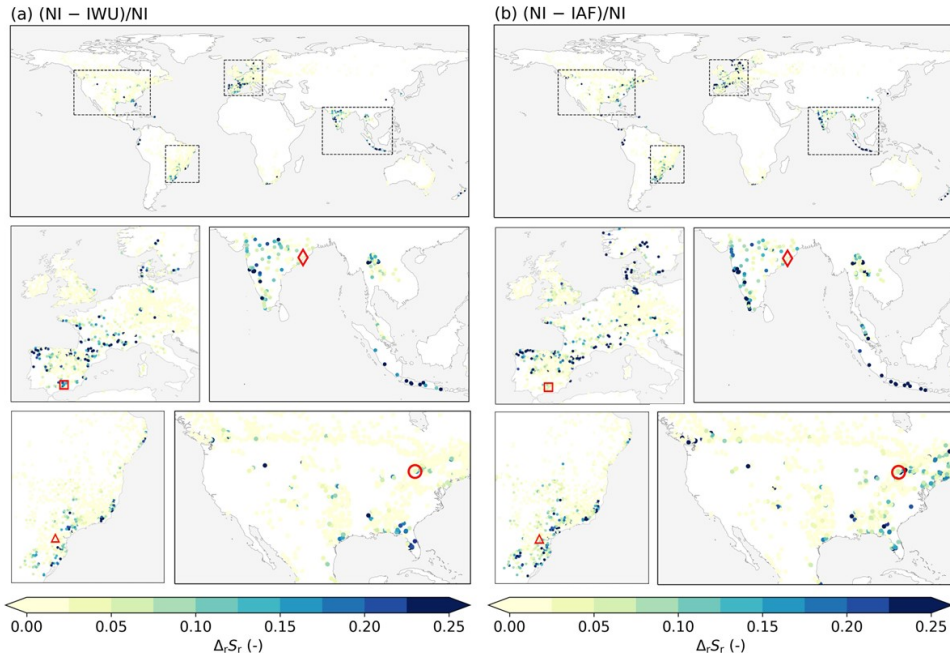
Figure 4.6: Relative difference in S_r ($\Delta_r S_r$ (-)) for (a) IWU compared to NI ((NI-IWU)/NI) and (b) IAF compared to NI ((NI-IAF)/NI). Red markers indicate the selected catchments from Fig. 4.5. See Table 4.1 for details on the irrigation cases.

4.3.2 REGIONAL DIFFERENCES OF IRRIGATION INFLUENCE ON ROOT ZONE STORAGE CAPACITY

Figure 4.7 shows that the effects of irrigation on S_r increased with increasing irrigated area fraction I_a for both IWU and IAF cases. We found the largest effects in catchments with $I_a > 0.1$, such as the example catchment in Asia (Fig. 4.5g). For these catchments, the median ΔS_r was 19 mm (IQR 10–31 mm) for IWU and 23 mm (IQR 11–42 mm) for IAF (Fig. 4.7), which correspond with decreases of 12 % and 15 %, respectively (Table 4.2). These effects were considerably larger than the effects of irrigation in catchments with $0.05 < I_a \leq 0.1$ that reached median $\Delta_r S_r$ of 6%, which corresponds to $\Delta S_r \approx 9$ mm (Fig. 4.7, Table 4.2). Although the median effects of irrigation on S_r for catchments with $I_a \leq 0.05$ were relatively small, the effects can be considerable for specific individual catchments as shown by the outliers in Fig. 4.7.
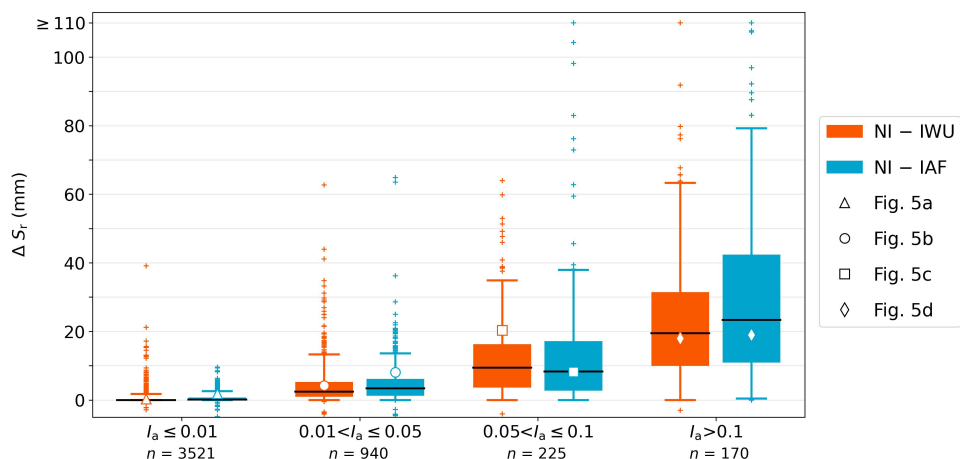
Figure 4.7: Boxplots of absolute S_r difference (ΔSr (mm)) between the irrigation cases (IWU and IAF) and the no irrigation case (NI) (Table 4.1). Catchments are stratified in four groups based on the irrigated area fraction I_a (Supplementary material Fig. S4.1), with n the number of catchments in each group. The black line represents the median, the box the interquartile range (IQR), and the whiskers the 5th and 95th percentiles. White markers represent the points presented in Fig. 4.5. Median and IQR values for relative S_r differences ($\Delta_r Sr$ (%)) are presented in Table 4.2.

The strongest irrigation influence on S_r for catchments with $I_a > 0.05$ was found in Asia, followed by South-America, North-America and Europe, for both IWU and IAF (Fig. 4.8a). For the catchments in Asia we found median values of ΔS_r for IWU of 21 mm (IQR 13–41 mm), and for IAF of 27 mm (IQR 12–56 mm). However, the relative differences in S_r were with $\Delta_r S_r$ =9–10 % smaller in Asia than in other regions, reaching up to 14 % in South America, because the initial S_r without accounting for irrigation was considerably larger in Asia than in other regions (Fig. 4.4, Table 4.2). Figure 4.8b shows that S_r decreased the most in tropical catchments with median $\Delta S_r = 19$ mm for IWU and 24 mm for IAF. These findings are in line with the results presented in Fig. 4.8a since most of the tropical catchments we evaluated were located in Asia (Supplementary material Fig. S4.2). For catchments in the arid, Mediterranean, temperate, and continental climate

zones, median ΔS_r was smaller and varied between 5 mm and 15 mm. However, catchments in temperate climates exhibited the largest relative influence of irrigation on S_r with median $\Delta_r S_r = 14\%$ for IWU and 15 % for IAF (Table 4.2).
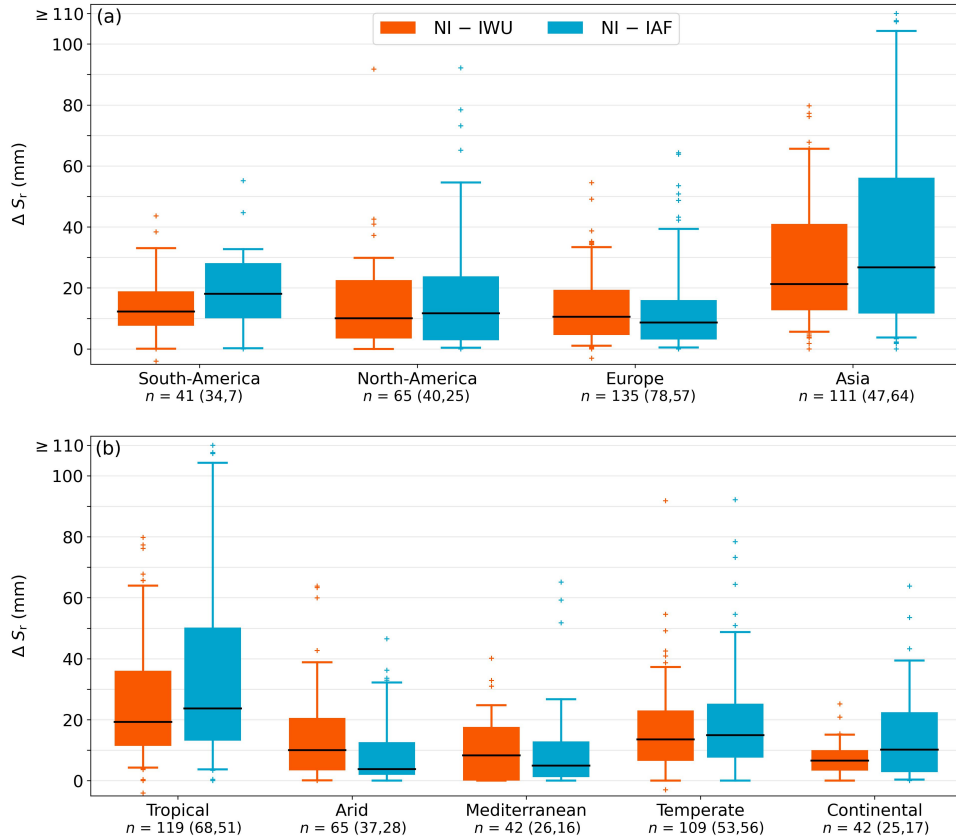
Figure 4.8: Boxplots of absolute S_r difference (ΔS_r (mm)) between the irrigation cases (IWU and IAF) and the no irrigation case (NI) (Table 4.1). In (a) catchments are stratified regionally, similar to the maps in Fig. 4.6, and in (b) catchments are stratified based on climate zone (Sect. 4.2.2, Supplementary material Fig. S4.2), with for both (a) and (b) only catchments with irrigated area fraction $I_a > 0.05$. The total number of catchments (n) in each group is given, with the numbers in brackets representing n in $0.05 < I_a \leq 0.1$, and $I_a > 0.1$, respectively. The black line represents the median, the box the interquartile range (IQR), and the whiskers the 5th and 95th percentiles. Median and IQR values for relative S_r differences ($\Delta_r Sr$ (%)) are presented in Table 4.2.

Table 4.2: Median and interquartile range (IQR) of the relative S_r difference ($\Delta_r Sr$ (%)) between the irrigation cases (IWU and IAF) and the no irrigation case (NI) with the catchments stratified for the top four rows based on irrigated area fraction (I_a) (Fig. 4.7), for the middle four rows based on region (only catchments with $I_a >$ 0.05) (Fig. 4.8a), and for the bottom five rows based on climate zones (only catchments with $I_a > 0.05$) (Fig. 4.8b). IQR is given as the 25th percentile – 75th percentile.

	(NI–IWU)/NI		(NI–IAF)/NI	
	median	IQR	median	IQR
$I_a \leq 0.01$	0	0–0	0	0–1
$0.01 < I_a \leq 0.05$	2	1–6	3	1–8
$0.05 < I_a \leq 0.1$	6	3–14	6	2–17
$I_a > 0.1$	12	7–21	15	6–33
South-America	12	7–20	14	8–29
North-America	9	3–16	11	3–23
Europe	9	4–19	7	2–26
Asia	9	5–16	10	4–21
Tropical	9	5–17	10	5–26
Arid	5	2–11	3	1–7
Mediterranean	5	0–10	3	1–8
Temperate	14	6–23	15	6–33
Continental	8	4–12	22	4–34

4.3.3 Comparison IWU and IAF methods

Figure 4.6 shows similar spatial patterns of $\Delta_r S_r$ for IWU and IAF, but the magnitudes differed. For most groups of catchments, IAF had a more pronounced effect on S_r than IWU (Table 4.2; Supplementary material Fig. S4.4). The different results for IWU and IAF can be explained by the different methodologies (Table 4.1). The IWU method directly used annual mean irrigation water use $\overline{I_w}$ from Zhang et al. (2022) as an estimate for I, if sufficient water was available in the surplus store S_s. On the other hand, in the IAF method I was defined as a fraction of S_s based on the irrigated area fraction I_a and the constant β. Therefore, the estimated I in IAF directly reflected the inter-annual variability of surplus water. Another cause for the different results for IWU and IAF lies in the estimation of β in IAF, which was based on minimization of the differences between $f_{i,IWU}$ and $f_{i,IAF}$ (Sect. 4.2.2; Fig. 4.3). In spite of this optimization, differences between $f_{i,IWU}$ and $f_{i,IAF}$ remained, which partially explain the differences in ΔS_r between the two methods.

4.4 Discussion

4.4.1 Synthesis of results

Our results showed that the effect of irrigation on S_r is discernible in all regions, but the magnitude of the effect depends on the amount of irrigation applied (Fig. 4.5–4.8). For many parts of the world the integration of irrigation in the S_r estimation did not have a large influence (Fig. 4.6). However, S_r considerably reduced for catchments with irrigated area fractions $I_a > 0.05$, and ignoring irrigation in these regions would lead to biased estimates of S_r, and, as a consequence, to inadequate modeling of vegetation

transpiration (Fig. 4.7). The reduction in S_r in catchments with irrigation was expected following that the memory method is based on the theory that vegetation will invest less in roots if sufficient water is available (Guswa, 2008). The observed changes in S_r are here attributed to changes in the vegetation roots, as they are directly related to the size of S_r. Additionally, adaptations at the plant scale associated with irrigation, such as adjustments in stomatal aperture (Chaves et al., 2016) and root hydraulic conductance (Lo Gullo et al., 1998), are also implicitly related to changes in S_r. The influence of irrigation on S_r estimates, as presented in Fig. 4.6, resembled the spatial pattern found in global assessments of irrigation water withdrawal (Huang et al., 2018), and the extent of irrigation activities (McDermid et al., 2023). This was expected since we used similar underlying irrigation data in the here developed irrigation methods. Given the ongoing irrigation expansion as presented by McDermid et al. (2023), it is expected that larger irrigation water volumes lead to further reductions of S_r at catchment scales in the near-future compared to the reductions reported in this study. At the same time, irrigation efficiency is also improving (McDermid et al., 2023), but this effect on S_r is less straight-forward. Improved irrigation efficiency (i.e., reduced soil evaporation) reduces the irrigation water volumes needed, which, at the catchment scale, leads to increased long-term mean discharge, and thus reduced long-term mean evaporation. This would result in reduced S_r in the memory method compared to a situation with lower irrigation efficiency. However, it has been shown that increased efficiency does not necessarily lead to reduced irrigation water use, as the saved water by increasing irrigation efficiency is often applied elsewhere (Grafton et al., 2018; Lankford et al., 2020).

Previous studies using the memory method did not consider irrigation in S_r estimates (e.g. De Boer-Euser et al., 2016; Stocker et al., 2023), or did not evaluate its effects (Wang-Erlandsson et al., 2016). To put our results into perspective, we looked at the effects of snow accumulation and melt on S_r estimates for the continental United States from Dralle et al. (2021), as this process alters the S_d time series in a similar way as irrigation by temporally shifting liquid water input into the system. Dralle et al. (2021) estimated that integrating snow accumulation and melt in the memory method led to an average reduction in S_r of 6 mm (2 %) for areas with >10 % winter snow coverage, and 28 mm (17 %) for areas with >80 % winter snow coverage (Dralle et al., 2020b). These magnitudes are broadly consistent with our findings for irrigation (Table 4.2). Our results indicate that the effects of snow and irrigation on S_r are comparable. In our study, 27 catchments have both considerable snowfall (snow days > 5% of the total days) and irrigation (I_a > 0.05). For these catchments, the snow model (Appendix 4.A) led on average to an S_r reduction of 7 mm (7%) for the NI case compared to a set-up without the snow model. With irrigation, S_r further reduced by 6 mm (7%), and 11 mm (12%) for IAF in these catchments.

Both the results of IWU and IAF showed considerable effects of irrigation on S_r (Figs. 4.6–4.8), and both are suitable to use in the memory method, keeping in mind the individual uncertainties related to data and methodological assumptions. We think that the IWU method is more suitable for regional application for periods with available I_w data (Zhang et al., 2022) than IAF, because I_w was derived from water balances, that strongly depend on the evaluated period. However, for spatial and temporal extrapolation the direct use of the I_w data in the IWU method is more uncertain than the simpler IAF

method, because the irrigated area fraction I_a used in IAF is expected to be temporally less variable than the water used for irrigation I_w. Therefore, we think the simpler parameterized IAF method is more suitable to use in the memory method for global applications and varying time periods. Moreover, IAF has the potential to be integrated dynamically in hydrological or land surface models used for global Earth system model studies and future predictions.

4.4.2 METHODOLOGICAL LIMITATIONS

By using several data sources, we obtained a large sample of 4856 catchments on different continents, characterized by a wide spectrum of climates, and in particular, regions with various levels of irrigation activity. However, the global coverage is not entirely balanced as Africa and large parts of Asia were undersampled. A further limitation may arise from the assumption in the memory method with irrigation methods proposed here that catchments are hydrologically closed systems. However, inter-catchment lateral flows, such as groundwater and irrigation water can significantly alter catchment water balances (e.g., Bouaziz et al., 2018; Fan, 2019; Condon et al., 2020). Moreover, the extraction of fossil groundwater for irrigation (Siebert et al., 2010; Grogan et al., 2017; de Graaf et al., 2019) can violate the assumption of closing water balances for the here developed irrigation methods in the memory method. Our methodology based on a sustainable water use assumption provides a lower boundary of S_r reduction in irrigated catchments. It is expected that irrigation exceeding sustainable use would lead to larger S_r reductions than reported here, as in this case more water is available to crops than derived from the water balance. Furthermore, the methodology assumes single succession of excess and deficit periods within a year (Fig. 4.2b), which is not necessarily representative in regions with double cropping systems or bimodal monsoons (Biradar and Xiao (2011)). Another limitation was the availability and quality of irrigation data (Sect. 4.2.1, Fig. 4.1). The annual mean $\overline{I_w}$ used in IWU was based on the 2011-2018 period, while the catchment time series varied between 1981 and 2010. Similarly, the I_a we used represented the 2005 irrigated area fraction (Siebert et al., 2015). The temporal mismatch between catchment hydrological timeseries and irrigation data may have led to an overestimation of I for the catchment specific period, as irrigated area, and irrigation techniques and efficiency have developed over the evaluated period (McDermid et al., 2023). Although this inconsistency in the temporal data influences the catchment specific outcomes, we believe that it did not have major influence the quantification of the general patterns of the effects of irrigation on S_r, which was the aim of this study.

An additional source of uncertainty in the application of the memory method, as used in this study, relates to the derivation of S_r from the S_d time series (Fig. 4.5). Given that an ecosystem has developed its S_r in a way it optimally functions and can overcome dry periods (e.g. Guswa, 2008), S_r for a specific time period would correspond to the maximum S_d value observed during that same time period ($S_r = \max(S_d)$). However, it is important to note that the memory method represents a simplified approximation of real ecosystem behavior and has inherent limitations. The most important limitation is that our application of the memory method did not account for the feedback between S_d and E_t/E_p, which likely led to an overestimation of S_d (Van Oorschot et al., 2021). In this study, we primarily focused on crops, that do not exhibit a multi-year root adaptation for

survival, as there is no remaining S_r after each year's harvest. However, the catchments used here are in no case entirely covered by crops, and, therefore, we used a return period of 2 years for the S_r estimation (following Wang-Erlandsson et al. (2016)).

4.5 Conclusions

Using a large sample of catchments globally, the presented results support the hypothesis that irrigation considerably reduces root zone storage capacity S_r estimated with the memory method. We found a median reduction of S_r by 12 % (IQR 7–21 %) for the IWU method and 15 % (IQR 6–33 %) for the IAF method for catchments with an irrigated area fraction I_a >10 %. In general, these effects were less pronounced in catchments with a smaller irrigated area, although the S_r for individual catchments could also be considerably influenced by irrigation. S_r decreased the most for catchments in tropical climates with a median decrease of 19–24 mm (for I_a >5 %). The reductions of S_r found in this study are in the same order of magnitude as the snow effects on S_r estimated by Dralle et al. (2021). Of paramount relevance for regional-to-global hydrological and climate modelling studies, this study demonstrates the relevance of irrigation for adequately estimating S_r. The irrigation water use can be expected to further increase over the next decades and so the related effects on S_r should be represented in the Earth system models that are used for the next climate projections. The methodological approach developed in this study could be profitably used in this respect.

4.A Memory method equations

These equations follow Chapter 3, who based their methods on Gao et al. (2014); De Boer-Euser et al. (2016); Nijzink et al. (2016) and Wang-Erlandsson et al. (2016). Total precipitation (P (mm day^{-1})) was split into liquid precipitation (P_l (mm day^{-1})), and precipitation falling as snow (P_{sn} (mm day^{-1})) based on temperature (Fig. 4.2). As temperature varies with altitude, we divided each catchment in elevation zones of 250 m. For each elevation zone z the daily temperature T_z was calculated by:

$$T_z(t) = T_a(t) + \lambda \Delta H \tag{4.8}$$

with T_a (°C) the catchment average temperature (GSWP3), λ the lapse rate of 0.0064 °C m^{-1}, and ΔH (m) the elevation difference between the elevation zone and the mean elevation. For each elevation zone z daily P_l and P_{sn} were defined by:

$$P_{l,z}(t) = \begin{cases} P(t) & \text{if } T_z(t) > T_t \\ 0 & \text{if } T_z(t) < T_t \end{cases} \tag{4.9}$$

$$P_{sn,z}(t) = \begin{cases} P(t) & \text{if } T_z(t) < T_t \\ 0 & \text{if } T_z(t) > T_t \end{cases} \tag{4.10}$$

The water balance of the snow storage (S_{sn}) (Fig. 4.2) for each elevation zone z was described by:

$$\frac{dS_{sn,z}}{dt} = P_{sn,z} - P_{m,z}. \tag{4.11}$$

Equation (4.11) can be solved by Eqs. (4.12) and (4.13), in which we used for the sum of fluxes between two time steps the following notation: $F_t = \int_{t-1}^{t} F \, dt$, where F is either P_{sn} or P_m. Thus, the numerical solution using daily time steps can be described as:

$$S_{sn,z,t} = S_{sn,z,t-1} + P_{sn,z,t} - P_{m,z,t} \tag{4.12}$$

$$P_{m,z,t} = \begin{cases} \max(M(T_{z,t} - T_t), \, S_{sn,z,t}) & \text{if } T_{z,t} < T_t \\ 0 & \text{if } T_{z,t} > T_t \end{cases} \tag{4.13}$$

with T_t the threshold temperature for snowfall of $0\,°C$, and M the snow melt factor of $2\,\text{mm}\,\text{d}^{-1}\,°C^{-1}$. Total catchment P_l, P_{sn}, and P_m were calculated as an area weighted sum of the values for the different elevation zones.

The calculation of effective precipitation P_e (mm day^{-1}) and transpiration E_t in Eq. (4.1) are similar as in Van Oorschot et al. (2021). The water balance of the interception store S_i (Fig. 4.2a) is described by:

$$\frac{dS_i}{dt} = P_l - P_e - E_i \tag{4.14}$$

with P_l the liquid precipitation (mm day^{-1}) and E_i the interception evaporation (mm day^{-1}). Equation (4.14) can be solved by Eqs. (4.15)-(4.17), in which we used for the sum of fluxes between two time steps the following notation: $F_t = \int_{t-1}^{t} F \, dt$, where F is either P_l, E_i, P_e or E_p (potential evaporation (mm day^{-1})). Thus, the numerical solution using daily time steps can be described as:

$$P_{e,t} = \begin{cases} 0 & \text{if } P_{l,t} + S_{i,t-1} \leq S_{i,max} \\ P_{l,t} + S_{i,t-1} - S_{i,max} & \text{if } P_{l,t} + S_{i,t-1} > S_{i,max} \end{cases} \tag{4.15}$$

$$S_{i,t}^* = S_{i,t-1} + P_{l,t} - P_{e,t} \tag{4.16}$$

$$E_{i,t} = \begin{cases} E_{p,t} & \text{if } E_{p,t} < S_{i,t}^* \\ S_{i,t}^* & \text{if } E_{p,t} \geq S_{i,t}^* \end{cases} \tag{4.17}$$

with E_p potential evaporation (mm day^{-1}) and $S_{i,max}$ the maximum interception storage (mm). The size of $S_{i,max}$ has minor influence on estimates of S_r as shown by e.g. Hrachowitz et al. (2021) and Bouaziz et al. (2020), and was, therefore, set to a constant value of 2.5 mm. Daily transpiration (E_t) in Eq. (4.1) was calculated as a fraction of daily E_p by:

$$E_t = (E_p - E_i) \frac{\overline{E_t}}{\overline{E_p} - \overline{E_i}} \tag{4.18}$$

with $\overline{E_t}$ the long-term mean E_t derived from the water balance ($\overline{E_t} = \overline{P_e} - \overline{Q}$), and $\overline{E_p}$ the long-term mean E_p.

5

THE GLOBAL VARIABILITY IN ROOT ZONE STORAGE CAPACITY EXPLAINED

In previous chapter we have shown the relevance of irrigation for root zone storage capacity estimation. Here, we will explore how different climate, landscape, and vegetation variables influence root zone storage capacity globally, and how this varies spatially. Based on these findings, we will develop an approach to obtain global estimates of root zone storage capacity.

SUMMARY

Vegetation roots play an essential role in regulating the hydrological cycle by removing water from the subsurface and releasing it to the atmosphere. However, the present understanding of the drivers of ecosystem-scale root development and their spatial variability globally is limited. This study investigates the varying roles of climate, landscape, and vegetation on the magnitude of root zone storage capacity (S_r) worldwide, which is defined as the maximum volume of subsurface moisture accessible to vegetation roots. To this aim, we quantified S_r and evaluated 21 possible climate, landscape, and vegetation controls for 3612 river catchments worldwide using a random forest machine learning model. Our findings reveal climate as primary, but spatially varying, driver of ecosystem scale S_r with landscape and vegetation characteristics playing a minor role. More specifically, we found the mean inter-storm duration as most dominant control of S_r globally, followed by mean temperature, mean precipitation, and mean topographic slope. While the inter-storm duration, temperature, and slope exhibit a consistent relation with S_r globally, the relation between precipitation and S_r varies spatially. Based on this spatial variability, we classified two different regimes: precipitation driven and energy limited. The precipitation-driven regime exhibits a positive relation between precipitation and S_r for precipitation of up to 3 mm day^{-1}, above which the relation flattens and eventually becomes negative. The energy-limited regime exhibits a strictly negative relation between precipitation and S_r. Using the random forest model based on these three dominant climate variables and the landscape variable slope, we generated a global gridded dataset of S_r, which closely resembles other global datasets of root characteristics. This suggests that our parsimonious approach based on four globally available variables to estimate S_r on a global scale has the potential to be readily and easily integrated into the parameterization of S_r in global hydrological and land surface models. This may enhance the accuracy of global predictions of land-atmosphere exchange fluxes and hydrological extremes by providing a robust representation of both spatial and temporal variability in vegetation root characteristics.

5.1 INTRODUCTION

Vegetation continuously adjusts to the prevailing climate and landscape characteristics ensuring optimal functionality (Fan et al., 2017; Gentine et al., 2012). One of the properties identified as adaptive in both space and time are vegetation root systems, that are shaped in a way to provide both anchoring in the subsurface (Read and Stokes, 2006), as well as access to sufficient nutrients and water (Zhang et al., 2019; Oldroyd and Leyser, 2020; Maan et al., 2023). Water uptake by roots of vegetation regulates vegetation transpiration, globally the largest water flux released from terrestrial systems (Schlesinger and Jasechko, 2014), and the associated latent heat flux into the atmosphere. In spite of its importance for the global water and energy budgets, direct large scale (i.e., beyond lab scale or individual plants) observations of root systems and the related water uptake do not exist.

Therefore, several indirect methods have been developed to represent vegetation root characteristics on large (here: global) scales. Schenk et al. (2009) provided global estimates of the soil depths that contain 95 % of the roots (i.e., the 95 % rooting depth), extrapolated from a sample of several hundred direct point-scale root observations of individual plants (Schenk and Jackson, 2003). Other studies followed inverse methods based on optimality principles to infer root characteristics at a global scale. For example, Kleidon (2004) maximized net primary production, while Yang et al. (2016) used balances of carbon cost and benefits, and Fan et al. (2017) derived depths of root water uptake from balances of water supply and demand. Similar water supply and demand considerations were also used by Wang-Erlandsson et al. (2016) and Stocker et al. (2023) to estimate global distributions of root zone storage capacity S_r (mm). S_r is defined as the maximum volume of subsurface moisture accessible to vegetation roots, representing all sources of water within the reach of roots, including unsaturated soil, deep and shallow groundwater (Gao et al., 2014). S_r is a fundamental characteristic of terrestrial hydrological systems as it regulates not only water budgets by partitioning precipitation into drainage and evaporation, but also energy budgets over the associated latent heat flux (Zhang et al., 2001; Donohue et al., 2012; Wang-Erlandsson et al., 2016). Many studies have suggested that, on ecosystem scale, S_r is mainly shaped by climate and in particular by the interplay of the temporal dynamics of water and energy availability, as vegetation optimizes its root system to sustain water demand (Kleidon, 2004; Laio et al., 2006; Guswa, 2008; Gentine et al., 2012; Gao et al., 2014; De Boer-Euser et al., 2016; Gao et al., 2023). Consequently, ecosystem disturbances such as climate change and human land-use change also influence the evolution of S_r, as demonstrated by multiple studies (Nijzink et al., 2016; Liu et al., 2020; Hrachowitz et al., 2021; Bouaziz et al., 2022; Tempel et al., 2024; Wang et al., 2024). Thus, insight in the specific controls of S_r is essential for predicting how different ecosystems will respond to such disturbances.

A range of other recent studies has explored how climate variables influence the extent of S_r across different regions in varying climatic zones. Gao et al. (2014) identified precipitation inter-storm duration and seasonality index as key controls of S_r in Thailand and the United States. Inter-storm duration is an indicator for the length of dry periods during which vegetation relies on its subsurface water buffer for transpiration and was linked to the size of vegetation root systems in multiple previous studies (e.g., Gentine et al., 2012; Sivandran and Bras, 2013). Conversely, de Boer-Euser et al. (2018)

observed a strong positive relationship between mean temperature and S_r in Finland, along with a positive correlation between aridity index and S_r, as also found by Zhao et al. (2016) in China. Also Gao et al. (2014) noted that, on average, drier regions have larger S_r than wetter regions in Thailand and the United States, but eco-region classes Tropical Savanna and Semi-arid Prairies deviated from this trend. Contrasting signals were also reported by Singh et al. (2020), who showed that increased aridity in tropical forests leads to decreased tree cover but increased S_r due to the remaining scarcer vegetation investing more in roots to create a water buffer for drier periods. However, in drier savanna-grasslands, S_r decreases with increased aridity (Singh et al., 2020). Yet, other studies do highlight that vegetation (de Boer-Euser et al., 2018) and landscape characteristics such as soil properties (Laio et al., 2006; Collins and Bras, 2007) and geology (Hahm et al., 2019; McCormick et al., 2021; Hahm et al., 2024) can play a relevant role at regional scales. Furthermore, vegetation and landscape characteristics in practice effectively determine S_r in most land surface models (Liu et al., 2020; Van Oorschot et al., 2021; Wang et al., 2021).

Overall, previous studies suggest that the influence of climate variables on S_r, considering both their magnitude and direction, is not consistent across different regions (Gao et al., 2014; Zhao et al., 2016; de Boer-Euser et al., 2018; Singh et al., 2020). Similarly, the spatially varying role of landscape and vegetation characteristics versus climate has not been systematically quantified and analyzed on a global scale. Thus, it remains unclear which aspects of climate, landscape and vegetation are the most important controls on S_r on global scale, and how these controls vary in space.

Here we bridge this knowledge gap by quantitatively characterizing, for the first time, how different climate, landscape and vegetation variables control the magnitude of S_r at the global scale, and how these controls vary spatially. Based on historical long-term water balance data, we estimate S_r in 3612 catchments worldwide using the memory method as in van Oorschot et al. (2024). We then test a wide range of climate, landscape, and vegetation variables to quantify their influence on S_r in different regions using a random forest model. Having identified a set of first order controls, we then use this model to extrapolate the catchment S_r estimates to a global gridded map of S_r ensuring coverage of regions where insufficient water balance data are available to directly estimate S_r. Finally, we evaluate how these estimates relate to other global datasets of root characteristics (Schenk and Jackson, 2003; Kleidon, 2004; Schenk et al., 2009; Yang et al., 2016; Wang-Erlandsson et al., 2016; Fan et al., 2017; Stocker et al., 2023).

5.2 Methods

5.2.1 Catchment data

Following the data and methods from van Oorschot et al. (2024), we estimated catchment-scale root zone storage capacity S_r in the 3612 study catchments using catchment-averaged daily precipitation data P (mm day^{-1}), daily potential evaporation E_p (mm day^{-1}), and annual mean discharge $\overline{Q}$ (mm day^{-1}) from sources documented in Table 5.1. We selected 3612 catchments based on the following four criteria: (1) at least 10 years of overlap between Q, P and E_p data; (2) catchment not exceeding the water limit, i.e., $\overline{Q} < \overline{P}$; (3) catchment not exceeding the energy limit, i.e., annual mean actual evaporation

$(\overline{E_a} = \overline{P} - \overline{Q}) < \overline{E_p}$; (4) catchment area $<10000\,\mathrm{km}^2$ to limit the heterogeneity within catchments.

To investigate the controls on S_r, we selected 21 catchment-averaged variables (Table 5.2), subdivided into three categories: climate, landscape, and vegetation. All variables were obtained from global datasets to ensure data consistency across catchments and in view of extrapolation from catchments to global scale. These variables were selected based on three main criteria: (1) globally available data that is representative for catchment scales; (2) variables with limited mutual interactions and (3) variables with limited assumptions on vegetation root characteristics (e.g., root depth) that are based on scarce observations that are not representative for ecosystems at landscape scales (Van Oorschot et al., 2021).

Table 5.1: Data sources used for the hydrological variables daily precipitation (P (mm day^{-1})), daily potential evaporation (E_p (mm day^{-1})), and annual mean discharge ($\overline{Q}$ (mm day^{-1})).

Variable	Data source
P (mm day^{-1})	Global Soil Wetness Project Phase 3 (GSWP-3) (Dirmeyer et al., 2006; Lange and Büchner, 2020)
E_p (mm day^{-1})	Global Land Evaporation Amsterdam Model version 3.5a (GLEAMv3.5a); based on the Priestley-Taylor approach (Miralles et al., 2011; Martens et al., 2017)
$\overline{Q}$ (mm day^{-1})	GSIM (Do et al., 2018; Gudmundsson et al., 2018), LamaH-CE (Klingler et al., 2021), CAMELS Australia (Fowler et al., 2021), CAMELS US (Addor et al., 2017), and EStreams (do Nascimento et al., 2024)

5.2.2 ROOT ZONE STORAGE CAPACITY ESTIMATION

Using the memory method, a term introduced in Chapter 3 and also known as water balance method and related to the mass curve technique, root zone storage capacity S_r (mm) is derived from root zone storage deficits (S_d (mm), e.g., Dralle et al., 2021; Gao et al., 2014; Wang-Erlandsson et al., 2016; Van Oorschot et al., 2021; van Oorschot et al., 2024). Based on long-term precipitation, potential evaporation and river discharge data we here computed long-term time-series of catchment S_d following the methodology described in Chapter 4 (Appendix 4.A). These time-series reflect both water supply to and water uptake by the vegetation's roots, leaving the vegetation as transpiration. Despite the inherent limitations of this method (Chapters 3 and 4) the S_r estimates it produces have been shown to closely align with those derived from hydrological model calibration, providing independent confirmation of their accuracy (Gao et al., 2014). After fitting the S_d time-series with the Gumbel distribution, S_r was estimated based on the extreme S_d values with a 20-year return period to represent the memory of vegetation to past water deficit conditions. The extreme value analysis was done to generalize the results as the time-series of the catchments have different lengths and do not necessarily overlap, and to represent the timescale of vegetation adaptation. Previous studies have shown that low vegetation adapts its S_r to droughts occurring with relatively low return periods (<10 years) and high vegetation to >40 years (Wang-Erlandsson et al., 2016).

For the aim of this study a-priori differentiation between land cover types is not desirable, and therefore a fixed 20 year return period was selected for all catchments following Singh et al. (2020) and Bouaziz et al. (2020).

5.2.3 RANDOM FOREST MODEL

We used a random forest regression model to predict catchment S_r and identify the dominant controls on S_r using the variables presented in Table 5.2. A random forest model was selected because it can represent the non-linear interactions between catchment variables and S_r which appeared during the studies of Gao et al. (2014), Zhao et al. (2016), de Boer-Euser et al. (2018), and during exploratory analyses on our dataset. The model was trained by minimizing the mean absolute difference (MAD (mm)) between root zone storage capacity from the memory method ($S_{r,M}$) and from the random forest model predictions ($S_{r,P}$). We applied a five-fold cross validation in order to fairly estimate the generalization performance. This implies that we performed model training and testing five times on a different subset of the total dataset, with for each fold 80% of the catchments (2890) were used for model training and 20% of the catchments (722) for model testing. Model performance is quantified by the mean and the standard deviation of the MAD between the $S_{r,M}$ and $S_{r,P}$ over the five cross-validation folds. Supplementary section S5.1 describes the details of the random forest model.

With the above described procedure we built a model with 21 predictor variables (21-variable model) (Table 5.2), which was used to investigate which catchment variables are a dominant control on S_r. The degree of control, i.e., the variable importance, is quantified by the permutation feature importance, which represents the decrease in model performance (ΔMAD) when the values of this single variable are randomly shuffled, while keeping the values of other variables (Breiman, 2001). Based on the variable importance of the 21-variable model and cross-correlations between individual variables, we selected a subset of four predictor variables used in a second 4-variable model. The reduced number of variables in the 4-variable model allows for in-depth model interpretation, and is simpler for future applications than the 21-variable model as it requires less data.

5.2.4 MODEL INTERPRETATION METHODS

For the 4-variable model, we used Individual Conditional Expectation (ICE) curves to analyze how individual variables influence $S_{r,P}$ in each catchment (Goldstein et al., 2015). In the ICE curves, S_r is predicted by the 4-variable model for each catchment with a range of hypothetical values for one of the variables, while keeping the original values of the other variables. This way we obtain a curve for each variable, for each catchment, that represents the dependence between the model $S_{r,P}$ and that variable for a single catchment. The 4-variable model is then also used to globally estimate $S_{r,P}$ at a 0.5° latitude × 0.5° longitude spatial resolution. This global S_r map is compared to other global datasets of root characteristics in terms of spatial patterns and Spearman rank correlations (r). Details of these global datasets are provided in Supplementary material Table S5.4.

Table 5.2: Catchment variables used for the random forest models (Sect. 5.2.3). All variables represent a single value per catchment, obtained through averaging grid cells that lie within the catchment boundary. For each catchment time series matching the available discharge data were used.

	Name	Description	Units	Data Source
Climate	$\overline{P}$	Mean precipitation	mm day^{-1}	GSWP-3 (Dirmeyer et al., 2006; Lange and Büchner, 2020)
	$\overline{E_p}$	Mean potential evaporation	mm day^{-1}	GLEAMv3.5a (Martens et al., 2017; Miralles et al., 2011)
	$\overline{T}$	Mean temperature	°C	GSWP-3
	$\overline{t_{IS}}$	Mean inter-storm duration	d	GSWP-3
	$I_{S,P}$	Seasonality index of precipitation (Gao et al., 2014)	–	GSWP-3
	I_{S,E_p}	Seasonality index of potential evaporation (Gao et al., 2014)	–	GLEAMv3.5a
	T_d	Temperature difference, defined as the difference between the monthly mean maximum and minimum temperature	°C	GSWP-3
	I_{AS}	Asynchronicity index between monthly mean precipitation and potential evaporation (Feng et al., 2019)	–	GSWP-3 and GLEAMv3.5a
	$\overline{f}_{snow}$	Mean snow cover fraction	–	MOD10A1 (Hall and Riggs, 2021)
	$f_{snow,v}$	Variability of snow cover fraction defined as $f_{snow,s}/\overline{f}_{snow}$ with $f_{snow,s}$ the standard deviation of monthly mean f_{snow}	–	MOD10A1
Landscape	e	Elevation	m	HydroSHEDS Hydrologically Conditioned DEM (Lehner et al., 2008) and Multi-Error-Removed Improved-Terrain (MERIT) DEM for latitudes $> 60°$ (Yamazaki et al., 2017)
	s	Slope	%	Same as for elevation.
	d_b	Depth to bedrock	m	SoilGrids250m (Hengl et al., 2017)
	f_{clay}	Fraction of soil clay content for 0-200 cm depth	–	SoilGrids250m
	f_{sand}	Fraction of soil sand content for 0-200 cm depth	–	SoilGrids250m
Vegetation	f_{tree}	Tree cover fraction	–	MOD44B.006 (DiMiceli et al., 2015)
	$f_{nontree}$	Non tree cover fraction	–	MOD44B.006
	f_{nonveg}	Non vegetation fraction defined as $1 - f_{tree} - f_{nontree}$	–	MOD44B.006
	$\overline{LAI}$	Mean leaf area index	–	CGLS (Verger et al., 2019)
	v_{LAI}	Variability of leaf area index defined as $LAI_s/\overline{LAI}$ with LAI_s the standard deviation of monthly mean LAI	–	CGLS
	I_a	Irrigated area fraction	–	(Siebert et al., 2015)

5

5.3 RESULTS AND DISCUSSION

5.3.1 ROOT ZONE STORAGE CAPACITY PREDICTION

The median $S_{r,M}$ estimated from the memory method in the 3612 catchments reached 120 mm (5-95th percentiles: 10–390 mm). The lower $S_{r,M}$ values are concentrated in cool-temperate humid regions while higher values are scattered around warmer, more arid regions (Fig. 5.1a). These magnitudes and pattern are broadly consistent with previous regional S_r estimates based on the memory method (Gao et al., 2014; De Boer-Euser et al., 2016; Zhao et al., 2016; Singh et al., 2020).
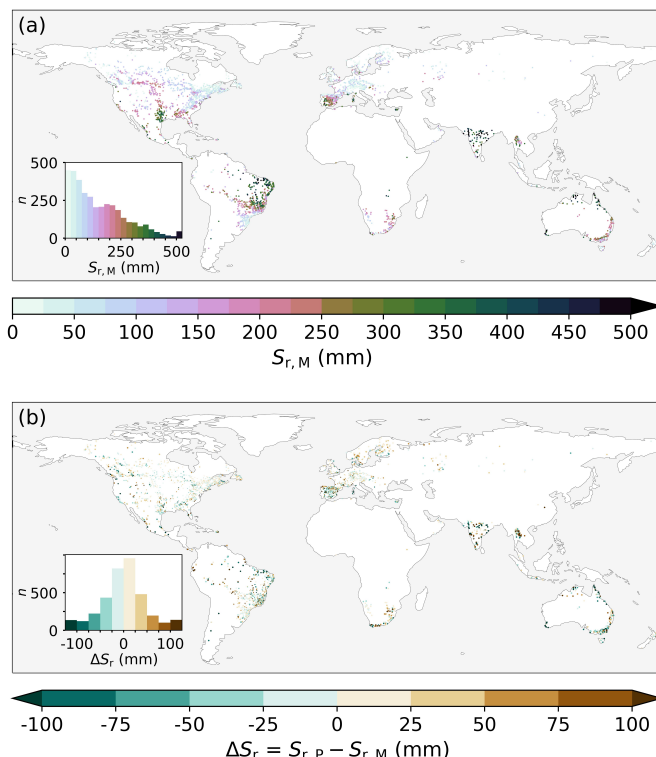
Figure 5.1: (a) Memory method root zone storage capacity ($S_{r,M}$ (mm)). (b) Difference between the 4-variable model predicted and memory method: $\Delta S_r = S_{r,P} - S_{r,M}$ of the test data, represented by the combined test results of the five-fold cross validation models. Relative differences between $S_{r,M}$ and $S_{r,P}$ are shown in Supplementary material Fig. S5.3. Dots represent the catchment outlets.

Using these estimates to train the 21-variable model then resulted in a MAD=13±0.2 mm ($R^2 = 0.97$) (Fig. 5.2a). The test sets of the cross-validation analysis exhibited with 35±2 mm ($R^2 = 0.81$) a larger scatter (Fig. 5.2b), but the limited performance fluctuations between the individual cross validation folds on the unseen test data (Supplementary material Table S5.2) indicate that the model is robust. The sequence of variable importance in the 21-variable model suggests that climate variables play by far the largest role, while landscape and vegetation variables are less important for explaining $S_{r,P}$ globally

(Fig. 5.2c). We found that the inter-storm duration ($\overline{t_{IS}}$) is the most important variable in the 21-variable model. This can be seen in Fig. 5.2c by the increase of MAD by $\approx 25\,\text{mm}$ when the catchment values of the mean inter-storm duration ($\overline{t_{IS}}$) are randomly shuffled between catchments, while keeping the other variables unchanged. The variable importance of mean inter-storm duration $\overline{t_{IS}}$ is followed by the climate variables mean snow cover $\overline{f}_{\text{snow}}$ ($\Delta\text{MAD} \approx 13\,\text{mm}$), mean temperature $\overline{T}$ ($\Delta\text{MAD} \approx 13\,\text{mm}$), and mean precipitation $\overline{P}$ ($\Delta\text{MAD} \approx 7\,\text{mm}$) (Fig. 5.2c, Table 5.2). While the most important landscape variables slope (s) and elevation (e) play a moderate role ($\Delta\text{MAD} \approx 5\,\text{mm}$), all other landscape variables and all vegetation variables are characterized by much lower $\Delta\text{MAD} < 2\,\text{mm}$. This indicates that they only have minor explanatory power for S_r.
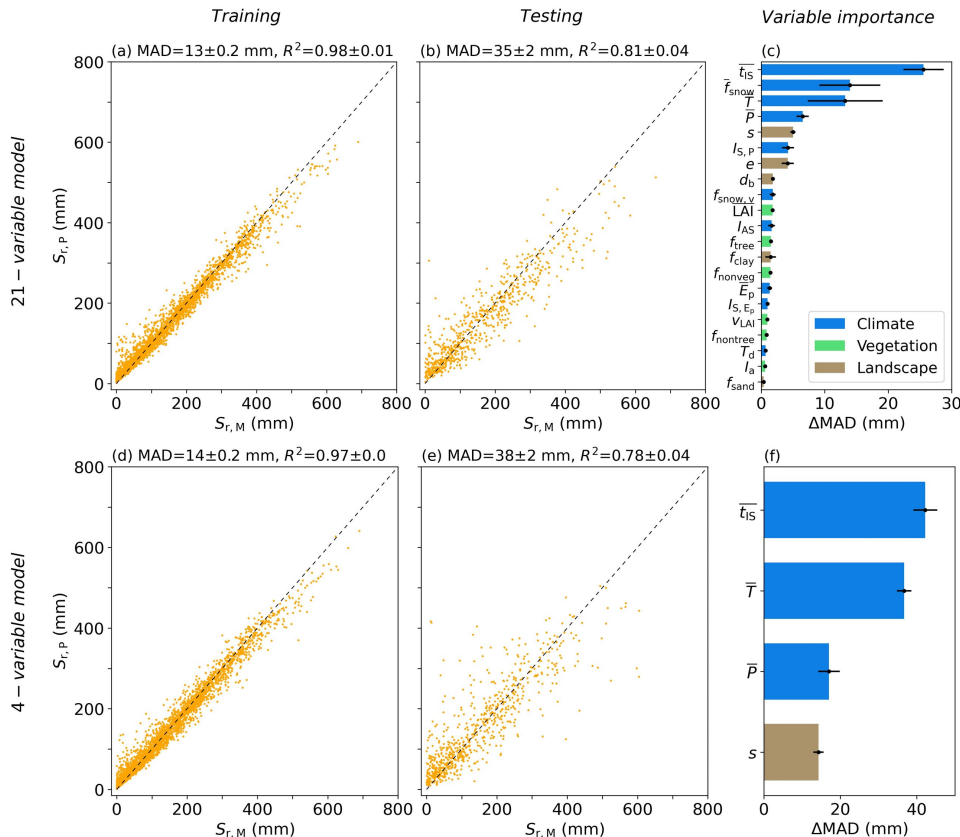
Figure 5.2: (a,b,d,e) Scatter plots of catchment memory method root zone storage capacity ($S_{r,M}$) and predicted root zone storage capacity ($S_{r,P}$) for (a, b) the 21-variable model, and (d, e) the 4-variable model. (a, d) show the training results and (b, e) the testing results of one of the cross validation folds. The mean and standard deviation of the mean absolute difference (MAD) and the R^2 in the title are based on the five-fold cross validation. (c) and (f) represent the variable importance (i.e., permutation feature importance) for the 21-variable model (c) and 4-variable model (f) expressed as an increase in MAD (ΔMAD) for each variable for the test data for the five-fold cross validation, with the bars representing the mean and the black lines the standard deviation. Table 5.2 shows the variable details and Supplementary material Fig. S5.1-5.2 shows the cross-correlation tables of the variables.

Based on these results we have then removed variables with low variable importance as well as correlated variables (see Supplementary material Fig. S5.1-5.2) to obtain an interpretable model, while maintaining high model performance. The resulting parsimonious 4-variable model uses $\overline{t_{\text{IS}}}$, $\overline{T}$ (excluding $\overline{f}_{\text{snow}}$ due to its strong correlation with $\overline{T}$), $\overline{P}$, and s (Fig. 5.3). With a training MAD=14±0.2 mm ($R^2 = 0.97$) (Fig. 5.2d), this reduced model predicts $S_{\text{r,P}}$ for the unseen test data with a MAD=38±2 mm ($R^2 = 0.78$) (Fig. 5.2e), which is very close to the test performance of the full 21-variable model (Fig. 5.2b). Here $\overline{t_{\text{IS}}}$ also emerges as the most important variable, followed by $\overline{T}$, $\overline{P}$, and s in the same hierarchy as in the full 21-variable model (Fig. 5.2f). Figure 5.1b shows that $S_{\text{r,P}}$ as predicted by the 4-variable model captures well the general pattern of $S_{\text{r,M}}$ with only rather limited deviations across all regions. Overall, ΔS_{r} remains within ±50 mm for 3173 (88%) catchments. Larger ΔS_{r}, both positive and negative, are found in regions such as India, Spain, and Northern Australia (Fig. 5.1b). However, in these regions $S_{\text{r,M}}$ is relatively large, thus resulting in relatively minor relative differences (Supplementary material Fig. S5.3).

5
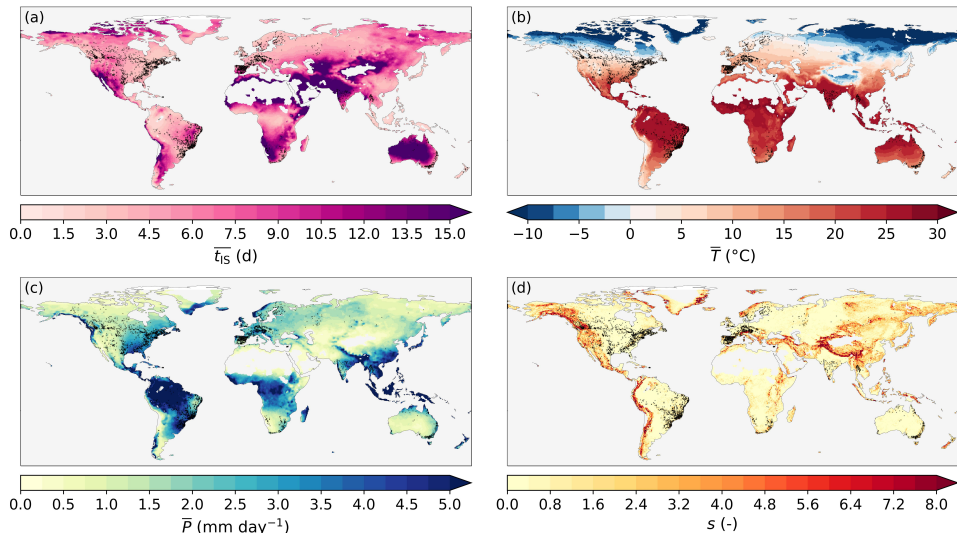
Figure 5.3: Global maps of the gridded variables that are input to the 4-variable model with (a) mean interstorm duration $\overline{t_{\text{IS}}}$ (d), (b) mean temperature $\overline{T}$ (°C), (c) mean precipitation $\overline{P}$ (mm day^{-1}), and (d) slope s (%), based on the data products described in Table 1. Black markers represent the 3612 catchment outlets. Lightgrey areas represent regions with values outside the ranges of the values in the catchments for at least one of the variables or oceans.

The dominance of climate variables as primary controls on S_{r} corresponds well with previous studies (e.g., Gao et al. (2014), De Boer-Euser et al. (2016), and Yang et al. (2016)). Our findings also show the relevance of topography, albeit to a lesser degree compared to climate, in shaping S_{r}, which was also highlighted by Fan et al. (2017). However, other studies also emphasized the importance of other landscape characteristics such as geology and soil textures for S_{r} (Laio et al., 2006; Hahm et al., 2019; McCormick et al., 2021; Hahm et al., 2024). In particular, Hahm et al. (2024) demonstrated that in regions with

limited variability in climate characteristics, geologic factors can become a stronger control on S_r. This also holds for the relevance of irrigation, that was previously found to be regionally influencing S_r (Chapter 4). Besides that, the limited impact of the degree of irrigation and other vegetation variables in shaping S_r directly results from their inherent dependence on climate conditions. The results of our analysis above are largely consistent with previous findings as they suggest that landscape characteristics are important as a secondary control at regional scales where differences of climate factors are more limited. For ecosystem scales in a global context, and thus a wide range in climates, climate is the clear first order control on S_r.

5.3.2 RELATION BETWEEN PREDICTOR VARIABLES AND ROOT ZONE STORAGE CAPACITY

The individual influences of the four variables on $S_{r,P}$ in the 4-variable model are represented by the Individual Conditional Expectation (ICE) curves in Fig. 5.4. Generally, as mean inter-storm duration $\overline{t_{IS}}$ and mean temperature $\overline{T}$ increase, $S_{r,P}$ also increases (Fig. 5.4a,b). Thus, overall, $S_{r,P}$ is higher in warmer regions with longer dry periods. However, it can also be observed that $\overline{t_{IS}}$ has more effect on $S_{r,P}$, i.e., a steeper slope in the ICE curve, for values between 3–5 days than for higher $\overline{t_{IS}}$, i.e., longer periods without rainfall (Fig. 5.4a). As $\overline{t_{IS}}$ increases, vegetation needs to invest more in roots in order to maintain transpiration during dry periods up to that value before it levels off and $S_{r,P}$ does not significantly increase anymore at higher $\overline{t_{IS}}$, which is related to lower vegetation density in drier regions with longer dry periods. The modelled $S_{r,P}$ has a stronger response to changes in $\overline{T}$ for $\overline{T}$ >10 °C than in colder regions with $\overline{T}$ <10 °C. With increasing $\overline{T}$, there is more energy available for transpiration, and, as long as water is available, vegetation will transpire more under higher temperatures, leading to larger S_r (Fig. 5.4b). On the
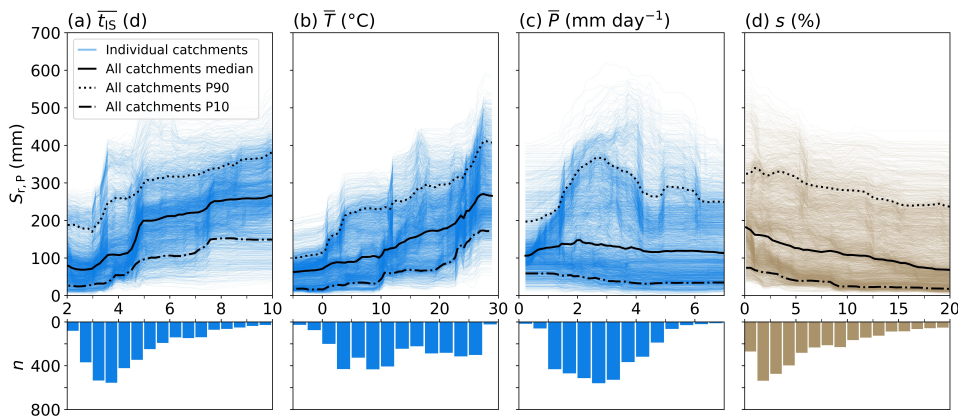
Figure 5.4: Individual Conditional Expectation (ICE) curves of the evaluation data for (a) mean inter-storm duration $\overline{t_{IS}}$ (d), (b) mean temperature $\overline{T}$ (°C), (c) mean precipitation $\overline{P}$ (mm day^{-1}), and (d) slope s (%) in the 4-variable model. The histograms represent the distribution of catchments (n) over the specific range of the variable. The curves are based on the model results of all 3612 catchments of the five-fold cross validation combined.

other hand, $S_{r,P}$ consistently decreases with increasing slope s (Fig. 5.4d). Steeper slopes are typically found in regions with higher elevations, which are associated with lower temperatures and reduced vegetation density, leading to lower S_r. In contrast with the almost monotonically increasing behaviour of $\overline{t_{IS}}$ and $\overline{T}$, and monotonically decreasing behaviour of s in relation to $S_{r,P}$ (Fig. 5.4a,b,d), the mean precipitation $\overline{P}$ exhibits a more complex relationship with $S_{r,P}$. For $\overline{P} < 2\,\mathrm{mm\,day^{-1}}$, the median relationship shows an increase in $S_{r,P}$, while for $\overline{P} > 2\,\mathrm{mm\,day^{-1}}$ this relationship is inverted and $S_{r,P}$ decreases with increasing $\overline{P}$. In addition, while for $\overline{t_{IS}}$, $\overline{T}$, and s, the general shapes of the ICE curves of the individual catchments largely resemble each other, considerable differences from the average pattern are observed for $\overline{P}$, as indicated by the curves of the 10th and 90th percentiles of the curves in Fig. 5.4c.

To further investigate these diverging patterns in the relationship between $\overline{P}$ and $S_{r,P}$, we disentangled the individual curves of Fig. 5.4c and grouped them based on their overall trajectories (considering slopes and peaks of the curves) in Fig. 5.5. This resulted in two distinct groups with each group showing similar influence of $\overline{P}$ on $S_{r,P}$, characterizing different regions globally (Fig. 5.5, Table 5.3). Overall, the precipitation-driven group shows the largest influence of changes in $\overline{P}$ on S_r (Fig. 5.5a). In these regions, $S_{r,P}$ strongly increases with increasing $\overline{P}$ up to ~3 mm day^{-1}. This is related to the lower vegetation density and thus less actively transpiring plants in these dry regions (Fig. 5.6a, Table 5.3). Here, increases in $\overline{P}$ directly lead to more vegetation activity and/or cover, and thus higher S_r. Hence, the development of S_r is mostly precipitation driven. Above $\overline{P} > 3\,\mathrm{mm\,day^{-1}}$, the systems experience transitions into systems that are not water limited anymore and where additional water input does not result in more root development and transpiration. This pattern dominates in regions that are characterized by relatively high temperatures and high rainfall seasonality (indicated by a large $\overline{t_{IS}}$), typical of tropical monsoon and (semi)-arid climates (Fig. 5.5c, Fig. 5.3, Table 5.3), for example North-Eastern Brazil, India, and Northern Australia. For the energy-limited group, an opposite signal compared to the precipitation-driven group is found, with $\overline{P}$ negatively influencing $S_{r,P}$ (Fig. 5.5b, Table 5.3). This pattern is found in energy-limited regions with year-round rainfall and relatively high tree cover, such as Europe and Canada, as well as tropical rainforests in the Amazon and Indonesia (Fig. 5.5c, Fig. 5.6b, Table 5.3). Here, sufficient water is available throughout much of the year to satisfy vegetation water demand. Therefore, an increase in water availability here does not lead to denser vegetation, and existing vegetation can reallocate resource investment into above-surface growth instead of extending its root system. As a consequence, additional water input, i.e., increase in $\overline{P}$, and thus frequent water re-supply to the root zone results in a reduced ecosystem-scale S_r (Fig. 5.5b): vegetation can access sufficient water with the need for deeper roots.

The spatial variability of the relation between $\overline{P}$ and S_r as shown in Fig. 5.5 is in line with previous regional studies by Gao et al. (2014), de Boer-Euser et al. (2018), and Singh et al. (2020). Specifically, the contrasting $\overline{P}$-S_r-relation between tropical rainforests (energy limited) and the savanna or prairie grassland regions (precipitation driven), correspond to the water stress and vegetation regimes in rainforest-savanna transitional regions found by Singh et al. (2020). Also Guswa (2008) found similar contrasting relations between wetness and rooting depth for energy-limited vs. water-limited regions. The re-

lations between our selected variables and S_r presented in Fig. 5.4 and 5.5 can represent how ecosystems can be plausibly expected to respond in terms of S_r to changes in the three climatic variables over time, resulting from internal variability and climate change. However, it should be noted that this only holds for relatively small changes in the variables, while larger changes may be accompanied by a transition of the entire ecosystem into a different state and the associated changes in vegetation composition. Furthermore, we assumed that the patterns are largely climate driven, but human influences can have major effects as well (e.g., Grill et al., 2019; Hrachowitz et al., 2021).
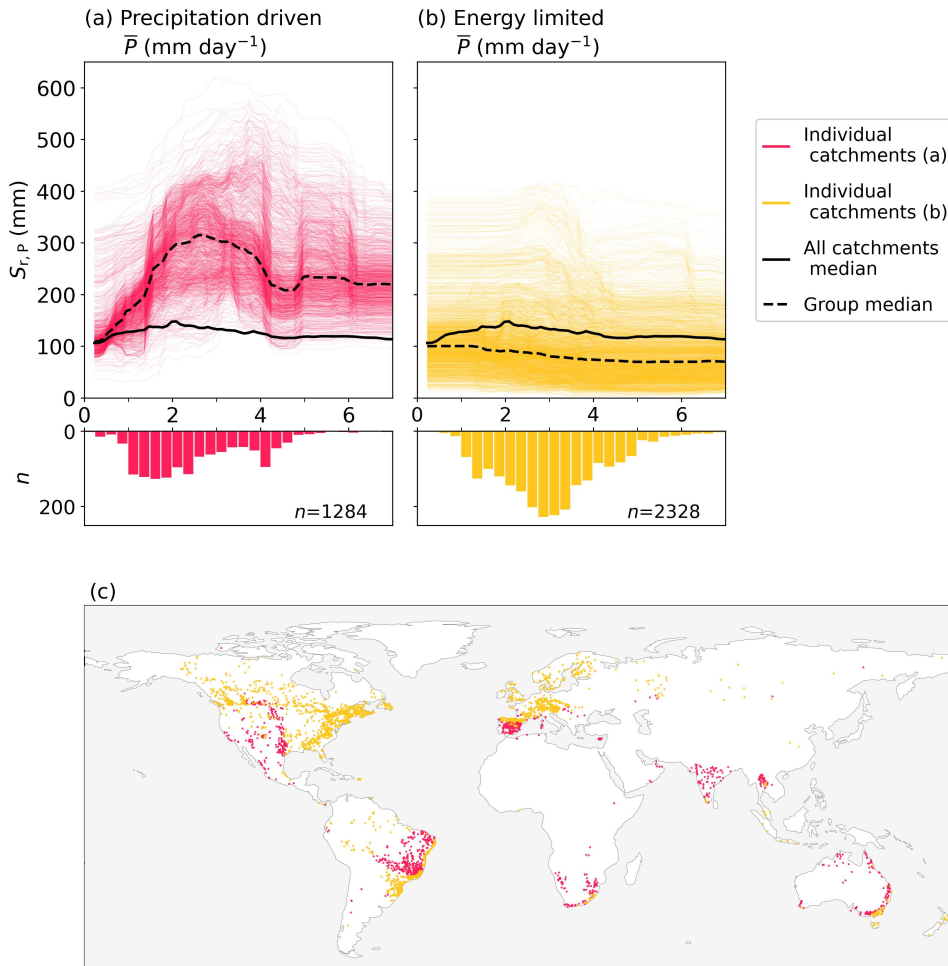
Figure 5.5: (a,b) Individual Conditional Expectation (ICE) curves for the mean precipitation $\overline{P}$ (mm day^{-1}) in the 4-variable model with the catchments categorized into two groups: (a) precipitation driven and (b) energy limited (Table 5.3). Groups are based on the patterns (slope and peaks) of the ICE curves in Fig. 5.4c. The histograms are as in Fig. 5.4. (c) Geographical location of the catchment outlets colored as the groups from (a) and (b).
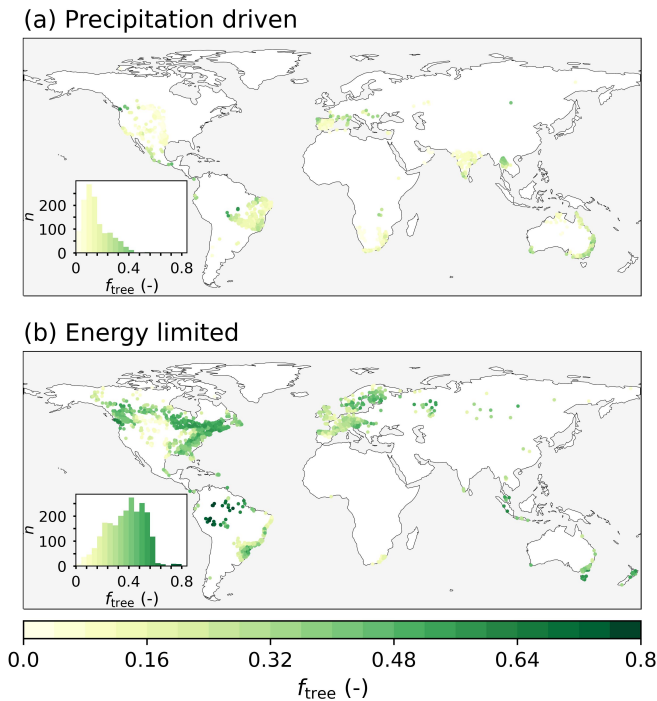
Figure 5.6: Fraction of tree cover (f_{tree} (-)) for the groups from Fig. 5.5 (Table 5.3): (a) precipitation driven and (b) energy limited. Dots represent the catchment outlets and histograms show the distribution of f_{tree} for the specific map.

Table 5.3: Characteristics of the two groups with distinct relations between mean precipitation $\overline{P}$ (mm day^{-1}) and root zone storage capacity S_r (mm) as identified in Fig. 5.5, with values for mean inter-storm duration $\overline{t_{IS}}$ (d), mean temperature $\overline{T}$ (°C), mean precipitation $\overline{P}$ (mm day^{-1}), slope s (%), and tree cover fraction f_{tree} (-) representing the median and inter quartile range (25th percentile – 75th percentile) of the catchments in the specific group (Table 5.2).

Group name	$\overline{t_{IS}}$ (d)	$\overline{T}$ (°C)	$\overline{P}$ (mm day^{-1})	s (%)	f_{tree} (-)	S_r increasing with $\overline{P}$	S_r decreasing with $\overline{P}$
Precipitation driven	7 (6–8)	20 (14–24)	2.3 (1.6–3.4)	5 (3–9)	0.13 (0.08–0.20)	$\overline{P} \approx 0-3$	$\overline{P} > 3$
Energy limited	4 (3–4)	9 (4–14)	3.0 (2.3–3.8)	6 (3–12)	0.39 (0.27–0.49)	-	$\overline{P} > 0$

5.3.3 GLOBAL COMPARISON OF ROOT CHARACTERISTICS

Here we used the 4-variable model and the data from Fig. 5.3 to create a global gridded map of $S_{r,P}$ (Fig. 5.7a), extrapolating beyond regions with available discharge observations. To place our results into a wider context, we compared them to seven other global estimates of root characteristics obtained with a wide range of different approaches (Supplementary material Table S5.4) (Schenk and Jackson, 2003; Kleidon, 2004; Schenk et al., 2009; Yang et al., 2016; Wang-Erlandsson et al., 2016; Fan et al., 2017; Stocker et al., 2023). Note that this comparison can only consider the general spatial pattern, while the absolute magnitudes are not necessarily comparable between these studies due to differences in methods, assumptions and underlying data.

Overall, the global distribution of $S_{r,P}$ broadly corresponds with the spatial patterns of other studies reflecting the hydrologically active rootzone in terms of root zone storage capacities reported by Stocker et al. (2023) (r=0.72) and Wang-Erlandsson et al. (2016) (r=0.48), and in terms of the optimized hydrologically active rooting depth by Kleidon (2004) (r=0.61) (Fig. 5.7a-d, Fig. 5.8a-d). Major differences are observed in the La Plata basin, where our $S_{r,P}$ estimates and Kleidon (2004) show relatively large values, while the S_r values from Stocker et al. (2023) and Wang-Erlandsson et al. (2016) are relatively small (Fig. 5.7a-d). Other differences are found in relatively arid regions of the Central US, and Central Asia (Fig. 5.7a-d), in which our 4-variable model $S_{r,P}$ estimates are higher compared to Stocker et al. (2023), Wang-Erlandsson et al. (2016), and Kleidon (2004) (Supplementary material Fig. S5.4).

It should be noted that the rooting depth characteristics presented in Fig. 5.7e-h are not necessarily proportional to the root zone storage capacity S_r due to the fact that rooting depth is a single plant property compared to S_r being an ecosystem property. Moreover, while rooting depth only represents the vertical extension of the roots, S_r accounts for the entire root profile, including lateral root extent and root density. Nevertheless, the rooting depth related products of Fan et al. (2017) and Schenk et al. (2009) (Fig. 5.7e,g) broadly resemble the spatial patterns of $S_{r,P}$, with r=0.70 and 0.73, respectively (Fig. 5.8a,e,g). However, considerable differences are observed between the maximum depth of root water uptake in Fig. 5.7e and our $S_{r,P}$ (Fig. 5.7a) in Australia and Southern Africa, where the maximum depth of root water uptake (Fan et al., 2017) is considerably larger than $S_{r,P}$ (Supplementary material Fig. S5.4). In these arid regions, the maximum depth of root water uptake is high because individual trees have deep roots to access sufficient water. However, the ecosystem S_r is low because of low vegetation density.

The spatial pattern of our $S_{r,P}$ in North-America with relatively low values in the Midwest US and relatively high values in the Great Plains corresponds well with the results of Fan et al. (2017) (Fig. 5.7e), Schenk et al. (2009) (Fig. 5.7g) and Gao et al. (2014), but less with the other datasets (Fig. 5.7b-d, Supplementary material Fig. S5.4). These differences arise likely from dry season/summer dormancy that is common for this C3-grass dominated part in the prairies of the Great Plains (e.g., Ke et al., 2013). In the memory method used in this study (van Oorschot et al., 2024) as well as by Gao et al. (2014), transpiration is defined as a fraction of potential evaporation based on the long-term mean actual evaporation from the water balance. During the dry season when potential evaporation is typically high and grasses go dormant, this methodological assumption likely

leads to an overestimation of transpiration, and thus S_r. The root characteristics from Kleidon (2004), Wang-Erlandsson et al. (2016), and (Stocker et al., 2023) are derived from datasets that directly represent vegetation activity, and are, therefore, less exposed to this limitation. This possibly also explains the differences in arid regions discussed before.

Our $S_{r,P}$ estimates contrast with the effective plant rooting depth values from Yang et al. (2016) in many regions, but it should be noted that Yang et al. (2016) similarly and markedly contrasts with all other datasets, with $r < 0.08$ (Fig. 5.8a,f). Also the comparison of observed rooting depths from Schenk and Jackson (2003) (Fig. 5.7h) with the other datasets reveals limited similarity. However, amongst all these global datasets our modeled $S_{r,P}$ exhibits the strongest correlation with these rooting depths, with r=0.23 (Fig. 5.8a,h).

Overall, the major features in the spatial pattern of $S_{r,P}$ in our study mirror those in the other compared seven datasets. In addition, $S_{r,P}$ correlates better with most of the other datasets than these datasets among themselves (Fig. 5.8a). This is a strong indication that using a parsimonious 4-variable model based on globally available hydroclimatic indices and the topography represented by slope, produces global pattern of $S_{r,P}$ that are at least as good as those of alternative approaches. These alternative approaches rely on higher dimensional models to estimate evaporation as compared to our 4-variable model, which is grounded in discharge observations. Furthermore, the four variables are readily represented and simulated by Earth system models (ESMs), therefore enabling the possibility of an interactive representation of S_r as a dynamically evolving variable in ESMs.

Our $S_{r,P}$ estimates contrast with the effective plant rooting depth values from Yang et al. (2016) in many regions, but it should be noted that Yang et al. (2016) contrasts with all other datasets, with r not exceeding 0.08 (Fig. 5.8a,f). Also the comparison of observed rooting depths from Schenk and Jackson (2003) (Fig. 5.7h) with the other datasets reveals limited similarity. However, the strongest correlation emerges between our modeled $S_{r,P}$ and these rooting depths, with r=0.23 (Fig. 5.8a,h).

Overall, the major features in the spatial pattern of $S_{r,P}$ in our study mirror those in the other compared datasets. In addition, $S_{r,P}$ correlates better with most of the other datasets than these datasets among themselves (Fig. 5.8a). This is a strong indication that using a simple, 4-variable model, based on readily and globally available hydroclimatic indices and the topography represented by slope, produces global pattern of $S_{r,P}$ that are at least as good as those of alternative approaches that rely on higher dimensional models and the associated assumptions.
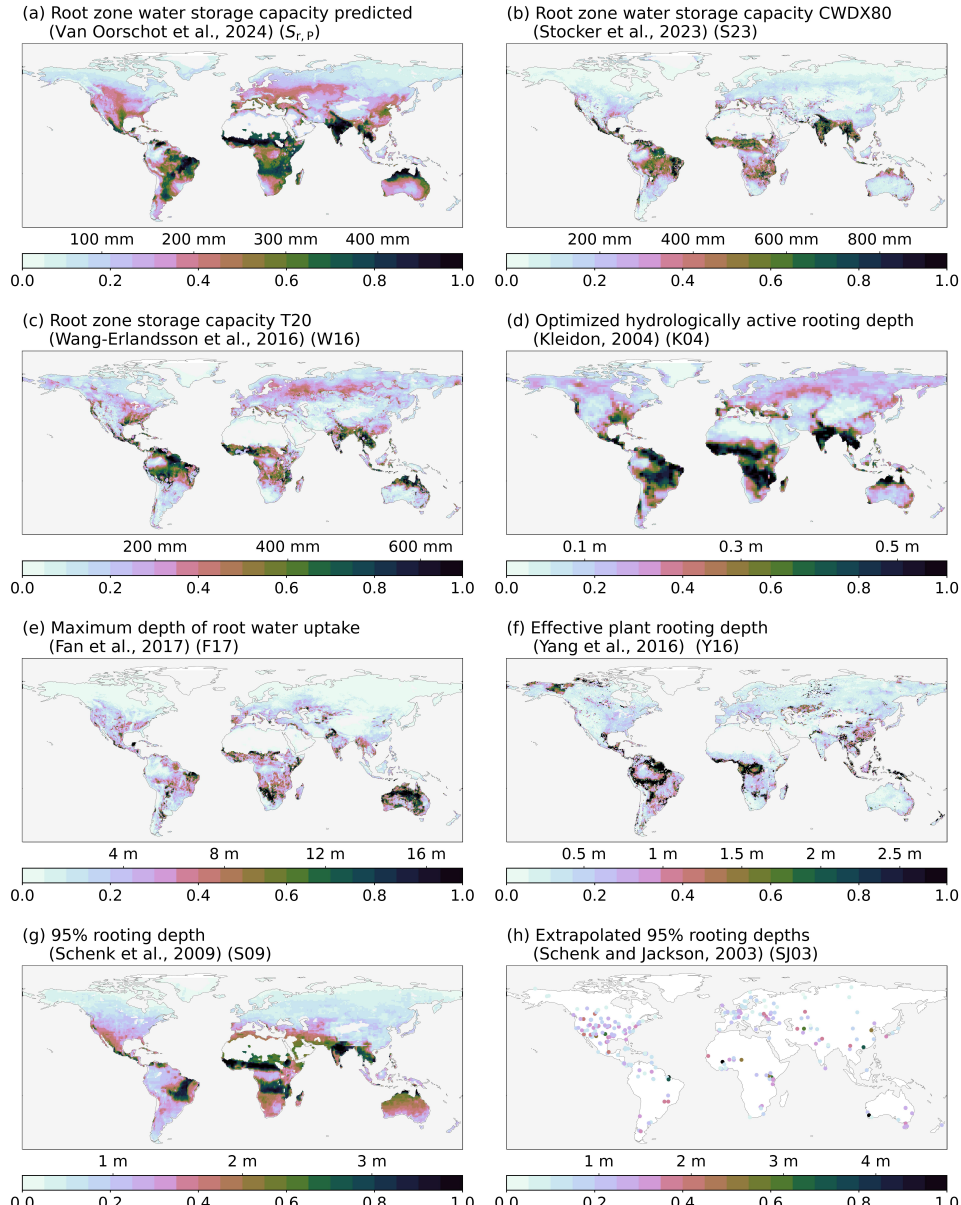
Figure 5.7: Global information on normalized vegetation root characteristics from this study and reference products. (a) Root zone storage capacity $S_{r,P}$ as predicted by the 4-variable model (average $S_{r,P}$ based on the five cross validation folds) and the data from Fig. 5.3. (b-g) The titles in all panels are corresponding with the original terminology used in the respective references. (h) Point data of measured rooting depths i.e., the depth of the 95th percentile of root mass, which may include extrapolation and at locations where several measurements have been made the average is shown (Schenk and Jackson, 2003). Note that the colorbars and bottom labels represent normalized values, with on top the corresponding original values and units. Maps of the differences are shown in Supplementary material Fig. S5.4.
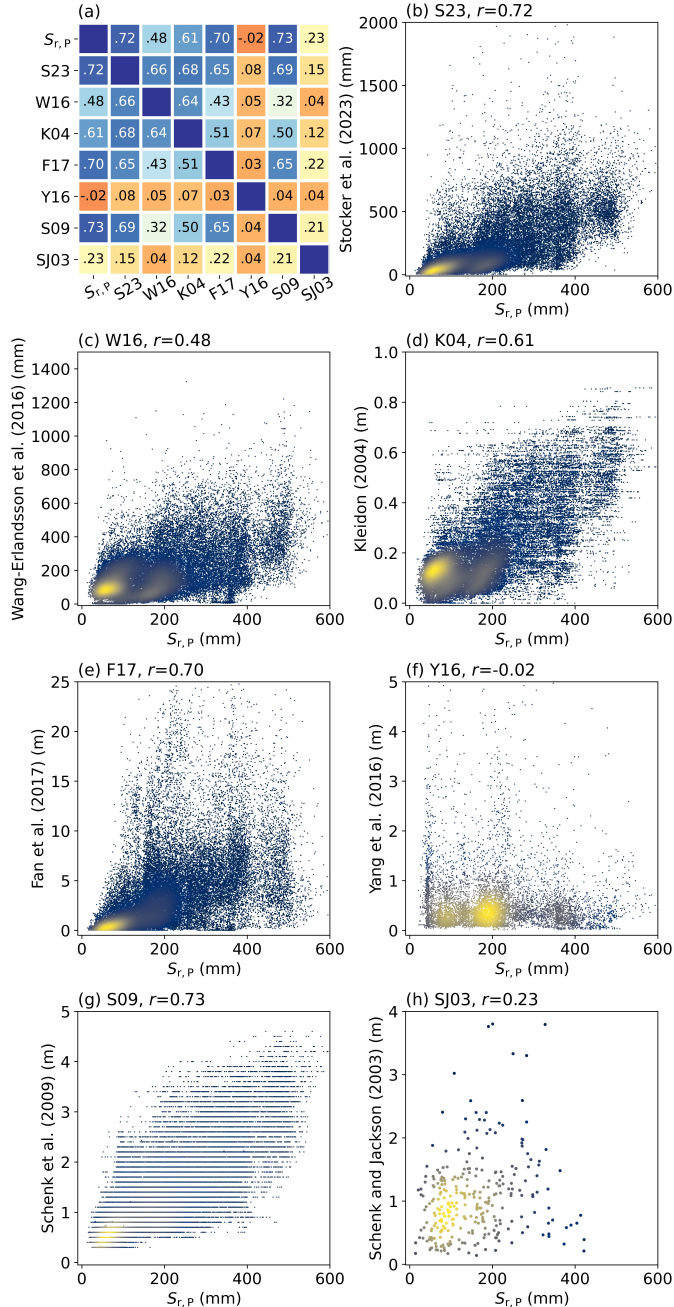
Figure 5.8: (a) Spearman rank correlation coefficients between reference root characteristics from Fig. 5.7(b-h) and the root zone storage capacity $S_{r,P}$ as predicted by the 4-variable model and the data from Fig. 5.2 (Fig. 5.7a). (b-h) Scatterplots of $S_{r,P}$ and the reference root characteristics. Note that the variables and the units are not the same for each product. The numbers in the title indicate the Spearman rank correlation coefficients, and the marker colors represent the point density. See Fig. 5.7 for the abbreviations used.

5.4 CONCLUSIONS

In our analysis we quantified for the first time the controls of ecosystem-scale root zone storage capacity S_r at the global scale using a random forest model. From this analysis, hydro-climatic variables emerged as the most dominant controls. Topographic slope also influences S_r, though to a lesser extent than climate. Other landscape and vegetation characteristics were found to play a minor role. More specifically, we found that inter-storm duration, temperature, precipitation, and topographic slope are the most dominant controls of S_r globally. We further found that inter-storm duration and temperature exhibit a near-monotonic positive relations with S_r, and that the slope is consistently negatively related to S_r. In contrast, the relation between precipitation and S_r varies in space. The emerging pattern suggests that while precipitation is strongly positively correlated with S_r in relatively dry regions with low vegetation cover, energy-limited regions are rather characterized by a negative relation. This highlights the distinct roles of precipitation for vegetation water-use in different climatic settings.

Our global S_r predictions, based on random forest models driven with the above variables, correspond closely with other global datasets of rootzone characteristics, which typically rely on more complex data sources and computations. In contrast, our model predicts S_r from the long-term means of three hydro-climatic variables ($\overline{P}$, $\overline{T}$, $\overline{t_{IS}}$), for which both historical data as well as future projections are readily available, and from topographic slope (s) that can be assumed as temporally invariant. The strength of our S_r prediction is further highlighted by its stronger correlation with most other datasets compared to the correlations observed between those datasets themselves.

For future studies, our approach opens the possibility to formulate and implement S_r as dynamically-evolving prognostic variable in large-scale land surface and hydrological models, mimicking the continuous evolution of S_r over time (Wang et al., 2024) and replacing the current static representation of this parameter in most of these models. As such, we emphasize that the methodology to estimate S_r provided here can readily be applied in land surface and hydrological models to improve their global representation of the coupling of root zone storage capacity with hydro-climatic variability (Abramowitz et al., 2024). This does not only have the potential to improve predictions of extreme river flow and seasonal water supply but, perhaps more importantly, also transpiration and thus latent heat fluxes representation (Van Oorschot et al., 2021; Giardina et al., 2024), which as a knock-on effect is expected to have major implications for climate predictions and projections.

5

6

CONCLUSIONS

In previous chapters several approaches have been explored to improve the model representations of the spatial and temporal variability of both aboveground and belowground vegetation. In this concluding chapter, we first discuss the main findings of our research in terms of model developments and the potential of these developments to improve modeled water fluxes. Then we focus on the insights and implications related to these main findings. Finally, we provide an outlook for future research activities related to large scale modeling of vegetation-water interactions.

6.1 MAIN FINDINGS

This dissertation addressed the issue of limited spatial and temporal vegetation variability in large scale hydrological and land surface models. The objective of this doctoral research was to develop more realistic model representations of spatial and temporal vegetation variability, and explore their potential for improving modeled water fluxes in these large scale models.

We presented model representations that adequately capture the spatial and temporal variability of both aboveground and belowground vegetation characteristics. These representations were based on readily available data that is representative for the scale of interest, namely large ecosystem scales (~5 to 100 km). Specifically, we included enhanced temporal variability of aboveground vegetation in the land surface model HTES-SEL by integrating interannual variability of land cover and leaf area index (LAI) based on satellite remote sensing data (Chapter 2). Furthermore, we developed a spatially and temporally varying model parameterization of effective vegetation cover using remote sensing data, which was integrated in HTESSEL (Chapter 2). Additionally, we developed an effective method to allow for more realistic spatial variability of the belowground vegetation characteristic root zone storage capacity (S_r), that is suitable to represent temporal variations as well. This S_r representation was obtained using the memory method that reflects the climate control on vegetation root development. We integrated, for the first time, climate-controlled S_r estimates based on the memory method in a land surface model, replacing inadequate lookup-table-based root zone parameters that do not reflect the spatial heterogeneity of roots (Chapter 3). Furthermore, we integrated a novel approach within the memory method to account for irrigation (Chapter 4). Finally, we established a parsimonious model to obtain adequate global estimates of S_r, that are suitable to be integrated in large scale models to accurately represent both spatial and temporal variability in S_r (Chapter 5).

We conclude that these more realistic representations of vegetation variability have potential for improving modeled water fluxes in large scale hydrological and land surface models. This outcome is supported by model simulations with the HTESSEL land surface model. Incorporating enhanced aboveground vegetation variability based on remote sensing data consistently improved the associated variability of modeled hydrology compared to simulations lacking this variability (Chapter 2). Additionally, we found that a more realistic, climate-controlled, representation of the vegetation's root zone improved the timing of modeled discharge in a regional context, and thus has potential to improve modeled water fluxes globally (Chapter 3). To achieve such improvements on a global scale, we found that our global S_r estimates based on a parsimonious model would be suitable to represent adequate spatial and temporal root zone variability, as they closely resemble other global estimates of root characteristics based on more complex data and computations (Chapter 5).

6.2 INSIGHTS AND IMPLICATIONS

In addition to the main findings, the outcomes of this dissertation also provide other valuable insights and implications for the large scale hydrological and climate modeling communities.

One of these insights emerges from the model improvements found when integrating interannual variability of aboveground vegetation characteristics (Chapter 2), emphasizing the importance of temporal vegetation variability in land modeling. Remote sensing data of vegetation characteristics is suitable to reflect realistic variability, and is directly applicable in model studies of historical periods for which data is available. This implies that, for example, the accuracy of climate reanalysis datasets such as ERA5 could be enhanced by incorporating interannual vegetation variability derived from remote sensing data. However, when modeling future periods in view of climate projections, we cannot directly rely on remote sensing data. In this case, historical data can be used to develop methodologies capable of projecting vegetation variability into the future. An example of such a methodology is provided in this research by the novel effective vegetation cover parameterization (Chapter 2).

Furthermore, our analyses emphasize the relevance of considering appropriate data and methods at the scale of interest, i.e., the model scale (~5 to 100 km). Upscaling processes and properties based on small scale observations to the coarse resolution of global models does not necessarily provide representative results. This is supported by the model improvements found when using a holistic representation of ecosystem scale S_r instead of lookup table based values that were based on point measurements (Chapter 3). Moreover, this is demonstrated by the inconsistency of these point measurements with the S_r patterns from our simple model and from other approaches based on ecosystem scales (Chapter 5; Fig. 5.7 and 5.8). This implies that adopting holistic approaches considering the scale of interest could also be beneficial for other aspects of large scale modeling, including model representations and evaluation of outputs.

Moreover, this dissertation highlights the value of analysing and understanding internal model processes in addition to the mere model outputs. This was achieved in two ways. First, we conducted thorough assessments of how internal model processes and feedbacks were influenced by the improved vegetation representations (Chapters 2 and 3). These assessments were accomplished with offline (land-only) model setups which establish a relatively controlled model environment. This additional analysis step is very valuable as it allows understanding of the underlying causes of observed changes in model outputs. As a consequence, it provides insights on how similar developments would potentially influence other models than the HTESSEL model used in this research, thus facilitating meaningful model comparisons. Furthermore, insights into the effects of model developments in an offline setup lead to enhanced understanding of how similar developments would influence model outputs in a coupled model setup used for climate predictions. Second, we zoomed in to the internal interactions in the random forest model used for predicting S_r from four simple, globally available variables (Chapter 5). These interactions revealed how different variables influence S_r across different regions, which can provide a first, quick understanding of the influence of climate changes on S_r within these regions. Thus, our efforts to develop and integrate more realistic model representations of vegetation variability contribute not only to improved outputs in the model world, but also to enhanced understanding of its connections with real-world processes.

Overall, the main implication from this research is that there is a clear potential of improved vegetation variability parameterizations to improve the modeled water fluxes

in large scale models. This would, furthermore directly imply improved predictions of global water budgets and hydrological extremes such as droughts and floods. In addition, more accurate model evaporation would also result in more accurate energy fluxes through the latent heat flux, and thus more accurate climate predictions.

6.3 Outlook

The insights and implications from this research provide a base for future research aiming to further enhance vegetation variability in large scale models. Specifically, our results call for fully adaptive modeling of root zone storage capacity. In Chapter 3 we emphasize the potential of climate-controlled root zone parameters to improve water flux simulations in land surface models. Additionally, the outcomes from Chapters 4 and 5 pave the way for application of climate-controlled root zone storage capacity in global models. Specifically, the global estimates of S_r presented in Fig. 6.1a can be integrated in global hydrological and land surface models to adequately represent the spatial variability of the vegetation's root zone. However, it should be noted that directly integrating S_r into these models is not straightforward. This is because S_r is typically not explicitly described in most models, but, instead, it results from the defined model rooting depth. Therefore, integrating S_r into these models requires careful consideration of the existing model structure.

For the specific case of HTESSEL, the theoretical S_r is solely based on soil textures and a spatially fixed model soil depth (Chapter 3). The spatial variability of the theoretical S_r, as presented in Fig. 6.1b, thus only reflects the spatial variability of the model soil texture and does not match our global S_r estimates, as quantified by a Spearman correlation between the two S_r representations of $r = 0.12$ (Fig. 6.1a, b). Additionally, the theoretical S_r values are considerably larger than our estimates (Fig. 6.1a, b). However, we found that part of this theoretical root zone storage is inactive, meaning that part of the root accessible soil water volume is not actually taken up by the model vegetation. Therefore, we also looked at the 'effective' S_r, which is here based on the amplitude of the modeled soil moisture. The HTESSEL effective S_r, presented in Fig. 6.1c, has lower values than the theoretical one which reduces the bias with respect to our S_r estimates. However, the spatial pattern of the effective S_r does also not resemble our global S_r spatial variability, with $r = 0.13$. From these findings we conclude that for any application of climate-controlled S_r in an existing model, one should carefully study how the different definitions and representations relate to each other. This also holds for application of remote sensing data of vegetation characteristics into models and for evaluation of model outputs compared with reference datasets.

The above described potential integration of global estimates of S_r in large scale models directly addresses the first three limitations concerning the spatial variability of root zone representation in land surface models, as discussed in Chapter 1. Taking it one step further, the findings from this research also support temporally dynamic and adaptive modeling of vegetation accessible soil water volumes, addressing also the fourth limitation regarding temporal root zone variability from Chapter 1. Specifically, the simple model from Chapter 5 to predict S_r based on three climate variables, that can be easily obtained from standard prognostic climate model variables, and one topographic variable, can be used to represent continuous adaptation of ecosystems in future predictions
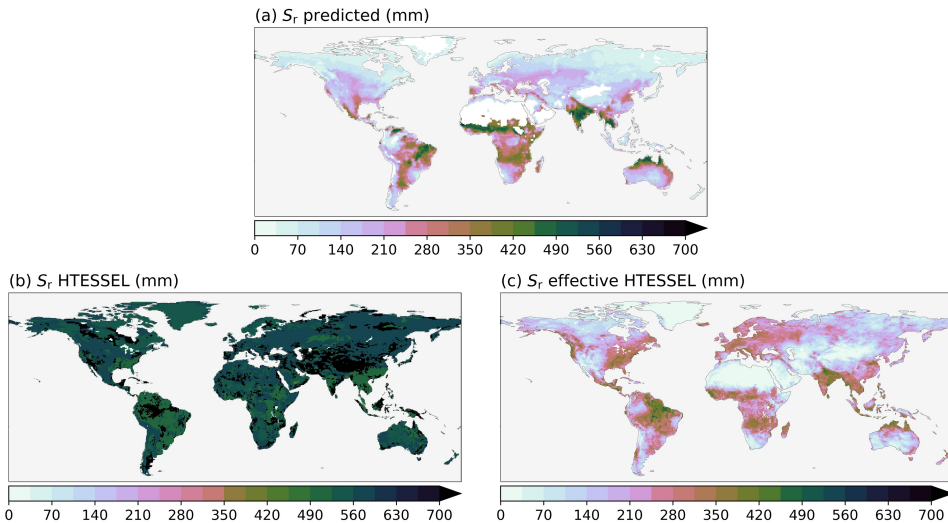
Figure 6.1: Global root zone storage capacity S_r (mm). (a) S_r estimates developed in Chapter 5 (Fig. 5.7a). (b) S_r as represented in the HTESSEL land surface model based on soil types and model soil depth (Chapter 3). (c) Effective S_r in HTESSEL ($S_r = \max(\max(SM)_{year} - \min(SM)_{year})_{years}$) based on the modeled soil moisture (SM) in model experiment IAKV from Chapter 2.

based on the modeled temporal evolution of these variables. Another option to represent the temporal variability of S_r is by directly integrating the memory method into the models. In this case, internal model computations of the root zone storage deficits based on modeled precipitation and evaporation can be translated into model S_r to represent the evolution of S_r over time. Both methods allow root systems to dynamically adapt in response to changes in rainfall and atmospheric water demand. This way we can overcome all the limitations of the representation of the vegetation's root zone presented in Chapter 1.

With a dynamic and adaptive model root zone representation in large scale hydrological and land surface models, improved modeled hydrology is expected, which would lead to higher accuracy of global climate predictions. More adequate models and predictions contribute directly to a deeper understanding of the effects of climate change on the Earth system. Moreover, beyond the scientific community, improved models facilitate more targeted climate change mitigation and adaptation strategies for both citizens and governments. In addition to further improving model representations and outputs in large scale models, future research should also focus on improving accessibility of these advancements (e.g., Hut et al., 2022). All the outcomes of this dissertation have been openly shared to promote research transparency, accessibility, and collaboration. However, the degree of reproducibility remains limited due to the lack of open access to essential research components such as the underlying models used. Improving accessibility and openness in hydrological and climate research would not only advance individual scientific progress but also create opportunities for collective progress.

REFERENCES

Abramowitz, G., Ukkola, A., Hobeichi, S., Cranko Page, J., Lipson, M., De Kauwe, M., Green, S., Brenner, C., Frame, J., Nearing, G., Clark, M., Best, M., Anthoni, P., Arduini, G., Boussetta, S., Caldararu, S., Cho, K., Cuntz, M., Fairbairn, D., Ferguson, C., Kim, H., Kim, Y., Knauer, J., Lawrence, D., Luo, X., Malyshev, S., Nitta, T., Ogee, J., Oleson, K., Ottlé, C., Peylin, P., de Rosnay, P., Rumbold, H., Su, B., Vuichard, N., Walker, A., Wang-Faivre, X., Wang, Y., and Zeng, Y.: On the predictability of turbulent fluxes from land: PLUMBER2 MIP experimental description and preliminary results, EGUsphere, 2024, 1–47, doi:10.5194/egusphere-2023-3084, 2024.

Addor, N., Newman, A. J., Mizukami, N., and Clark, M. P.: The CAMELS data set: catchment attributes and meteorology for large-sample studies, Hydrology and Earth System Sciences, 21, 5293–5313, doi:10.5194/hess-21-5293-2017, 2017.

Albergel, C., Munier, S., Jennifer Leroux, D., Dewaele, H., Fairbairn, D., Lavinia Barbu, A., Gelati, E., Dorigo, W., Faroux, S., Meurey, C., Le Moigne, P., Decharme, B., Mahfouf, J. F., and Calvet, J. C.: Sequential assimilation of satellite-derived vegetation and soil moisture products using SURFEX-v8.0: LDAS-Monde assessment over the Euro-Mediterranean area, Geoscientific Model Development, 10, 3889–3912, doi:10.5194/gmd-10-3889-2017, 2017.

Albergel, C., Munier, S., Bocher, A., Bonan, B., Zheng, Y., Draper, C., Leroux, D. J., and Calvet, J.-C.: LDAS-Monde Sequential Assimilation of Satellite Derived Observations Applied to the Contiguous US: An ERA-5 Driven Reanalysis of the Land Surface Variables, Remote Sensing, 10, doi:10.3390/rs10101627, 2018.

Alessandri, A., Gualdi, S., Polcher, J., and Navarra, A.: Effects of land surface–vegetation on the boreal summer surface climate of a GCM, Journal of climate, 20, 255–278, doi:10.1175/JCLI3983.1, 2007.

Alessandri, A., Catalano, F., De Felice, M., Van Den Hurk, B., Doblas Reyes, F., Boussetta, S., Balsamo, G., and Miller, P. A.: Multi-scale enhancement of climate prediction over land by increasing the model sensitivity to vegetation variability in EC-Earth, Climate Dynamics, 49, 1215–1237, doi:10.1007/s00382-016-3372-4, 2017.

Alexandratos, N. and Bruinsma, J.: World agriculture towards 2030/2050: the 2012 revision, Food and Agricultural Organization of the United Nation, doi:10.22004/ag.econ.288998, 2012.

Anderson, M. C., Norman, J. M., Kustas, W. P., Li, F., Prueger, J. H., and Mecikalski, J. R.: Effects of vegetation clumping on two-source model estimates of surface energy fluxes from an agricultural landscape during SMACEX, Journal of Hydrometeorology, 6, 892–909, doi:10.1175/JHM465.1, 2005.

Ardilouze, C., Batté, L., Bunzel, F., Decremer, D., Déqué, M., Doblas-Reyes, F. J., Douville, H., Fereday, D., Guemas, V., MacLachlan, C., Müller, W., and Prodhomme, C.: Multi-model assessment of the impact of soil moisture initialization on mid-latitude summer predictability, Climate Dynamics, 49, 3959–3974, doi:10.1007/s00382-017-3555-7, 2017.

Australian Government Bureau of Meteorology: Hydrologic Reference Stations, URL http://www.bom.gov.au/water/hrs/index.shtml, last access: September 2019, 2019.

Bakker, M. R., Jolicoeur, E., Trichet, P., Augusto, L., Plassard, C., Guinberteau, J., and Loustau, D.: Adaptation of fine roots to annual fertilization and irrigation in a 13-year-old Pinus pinaster stand, Tree Physiology, 29, 229–238, doi:10.1093/treephys/tpn020, 2009.

Balsamo, G., Viterbo, P., Beijaars, A., van den Hurk, B., Hirschi, M., Betts, A. K., and Scipal, K.: A revised hydrology for the ECMWF model: Verification from field site to terrestrial water storage and impact in the integrated forecast system, Journal of Hydrometeorology, 10, 623–643, doi:10.1175/2008JHM1068.1, 2009.

Balsamo, G., Pappenberger, F., Dutra, E., Viterbo, P., and van den Hurk, B.: A revised land hydrology in the ECMWF model: a step towards daily water flux prediction in a fully-closed water cycle, Hydrological Processes, 25, 1046–1054, doi:10.1002/hyp.7808, 2011.

Balsamo, G., Agusti-Panareda, A., Albergel, C., Arduini, G., Beljaars, A., Bidlot, J., Blyth, E., Bousserez, N., Boussetta, S., Brown, A., Buizza, R., Buontempo, C., Chevallier, F., Choulga, M., Cloke, H., Cronin, M. F., Dahoui, M., De Rosnay, P., Dirmeyer, P. A., Drusch, M., Dutra, E., Ek, M. B., Gentine, P., Hewitt, H., Keeley, S. P., Kerr, Y., Kumar, S., Lupu, C., Mahfouf, J.-F., McNorton, J., Mecklenburg, S., Mogensen, K., Muñoz-Sabater, J., Orth, R., Rabier, F., Reichle, R., Ruston, B., Pappenberger, F., Sandu, I., Seneviratne, S. I., Tietsche, S., Trigo, I. F., Uijlenhoet, R., Wedi, N., Woolway, R. I., and Zeng, X.: Satellite and In Situ Observations for Advancing Global Earth Surface Modelling: A Review, Remote Sensing, 10, doi:10.3390/rs10122038, 2018.

Beck, H. E., Zimmermann, N. E., McVicar, T. R., Vergopolan, N., Berg, A., and Wood, E. F.: Present and future köppen-geiger climate classification maps at 1-km resolution, Scientific Data, 5, 1–12, doi:10.1038/sdata.2018.214, 2018.

Bergstrom, S.: The development of a snow routine for the HBV-2 model, Nordic Hydrology, pp. 73–92, doi:10.2166/nh.1975.0006, 1975.

Biradar, C. M. and Xiao, X.: Quantifying the area and spatial distribution of double- and triple-cropping croplands in India with multi-temporal MODIS imagery in 2005, International Journal of Remote Sensing, 32, 367–386, doi:10.1080/01431160903464179, 2011.

Bouaziz, L., Weerts, A., Schellekens, J., Sprokkereef, E., Stam, J., Savenije, H., and Hrachowitz, M.: Redressing the balance: Quantifying net intercatchment groundwater

flows, Hydrology and Earth System Sciences, 22, 6415–6434, doi:10.5194/hess-22-6415-2018, 2018.

Bouaziz, L. J., Steele-Dunne, S. C., Schellekens, J., Weerts, A. H., Stam, J., Sprokkereef, E., Winsemius, H. H., Savenije, H. H., and Hrachowitz, M.: Improved Understanding of the Link Between Catchment-Scale Vegetation Accessible Storage and Satellite-Derived Soil Water Index, Water Resources Research, 56, 1–22, doi:10.1029/2019WR026365, 2020.

Bouaziz, L. J. E., Aalbers, E. E., Weerts, A. H., Hegnauer, M., Buiteveld, H., Lammersen, R., Stam, J., Sprokkereef, E., Savenije, H. H. G., and Hrachowitz, M.: Ecosystem adaptation to climate change: the sensitivity of hydrological predictions to time-dynamic model parameters, Hydrology and Earth System Sciences, 26, 1295–1318, doi:10.5194/hess-26-1295-2022, 2022.

Boussetta, S. and Balsamo, G.: Vegetation dataset of Land Use / Land Cover and Leaf Area Index Land Use / Land Cover and Leaf Area Index, Tech. rep., URL https://confess-h2020.eu/results/deliverables/, 2021.

Boussetta, S., Balsamo, G., Beljaars, A., Kral, T., and Jarlan, L.: Impact of a satellite-derived leaf area index monthly climatology in a global numerical weather prediction model, International Journal of Remote Sensing, 34, 3520–3542, doi:10.1080/01431161.2012.716543, 2013.

Boussetta, S., Balsamo, G., Arduini, G., Dutra, E., Choulga, M., Agustí-panareda, A., Beljaars, A., Wedi, N., Munõz-sabater, J., Rosnay, P. D., Sandu, I., Hadade, I., Mazzetti, C., Prudhomme, C., Yamazaki, D., and Zsoter, E.: ECLand : The ECMWF Land surface modelling system, doi:10.3390/atmos12060723, 2021.

Breiman, L.: Machine Learning, 45, 5–32, doi:10.1023/A:1010933404324, 2001.

Brunner, M. I., Melsen, L. A., Wood, A. W., Rakovec, O., Mizukami, N., Knoben, W. J. M., and Clark, M. P.: Flood spatial coherence, triggers, and performance in hydrological simulations: large-sample evaluation of four streamflow-calibrated models, Hydrology and Earth System Sciences, 25, 105–119, doi:10.5194/hess-25-105-2021, 2021.

Canadell, J., Jackson, R., Ehleringer, J., Mooney, H., Sala, O., and Schulze, E.: Maximum rooting depth of vegetation types at the global scale, Oecologia, 108, 583–595, doi:10.1007/BF00329030, 1996.

Chaves, M., Costa, J., Zarrouk, O., Pinheiro, C., Lopes, C., and Pereira, J.: Controlling stomatal aperture in semi-arid regions—The dilemma of saving water or being cool?, Plant Science, 251, 54–64, doi:10.1016/j.plantsci.2016.06.015, special Issue: Water-Use Efficiency in Plants, 2016.

Chen, B., Lu, X., Wang, S., Chen, J. M., Liu, Y., Fang, H., Liu, Z., Jiang, F., Arain, M. A., Chen, J., and Wang, X.: Evaluation of Clumping Effects on the Estimation of Global Terrestrial Evapotranspiration, pp. 1–24, 2021.

Chen, J. M., Menges, C. H., and Leblanc, S. G.: Global mapping of foliage clumping index using multi-angular satellite data, Remote Sensing of Environment, 97, 447–457, doi:10.1016/j.rse.2005.05.003, 2005.

Coenders-Gerrits, A. M., Van Der Ent, R. J., Bogaard, T. A., Wang-Erlandsson, L., Hrachowitz, M., and Savenije, H. H.: Uncertainties in transpiration estimates, Nature, 506, 2013–2015, doi:10.1038/nature12925, 2014.

Collins, D. B. and Bras, R. L.: Plant rooting strategies in water-limited ecosystems, Water Resources Research, 43, 1–10, doi:10.1029/2006WR005541, 2007.

Condon, L. E., Markovich, K. H., Kelleher, C. A., McDonnell, J. J., Ferguson, G., and McIntosh, J. C.: Where Is the Bottom of a Watershed?, Water Resources Research, 56, e2019WR026 010, doi:10.1029/2019WR026010, e2019WR026010 2019WR026010, 2020.

Copernicus Climate Change Service: Land cover classification gridded maps from 1992 to present derived from satellite observations, doi:10.24381/cds.006f2c9a, 2019.

Copernicus Global Land Service: Fraction of green vegetation Cover and Leaf Area Index, URL https://land.copernicus.eu/global/products/, last access: January 2022, 2022.

De Boer-Euser, T., McMillan, H. K., Hrachowitz, M., Winsemius, H. C., and Savenije, H. H.: Influence of soil and climate on root zone storage capacity, Water Resources Research, 52, 2009–2024, doi:10.1002/2015WR018115, 2016.

de Boer-Euser, T., Meriö, L.-J., and Marttila, H.: Controls on root zone storage capacity in boreal regions, Hydrology and Earth System Sciences Discussions, pp. 1–20, doi:10.5194/hess-2018-87, 2018.

de Graaf, I. E., Gleeson, T., Van Beek, L., Sutanudjaja, E. H., and Bierkens, M. F.: Environmental flow limits to global groundwater pumping, Nature, 574, 90–94, doi:10.1038/s41586-019-1594-4, 2019.

de Rosnay, P. and Polcher, J.: Modelling root water uptake in a complex land surface scheme coupled to a GCM, Hydrology and Earth System Sciences, 2, 239–255, doi:10.5194/hess-2-239-1998, 1998.

Defourny, P., Lamarche, C., Bontemps, S., de Maet, T., Van Bogaert, E., Moreau, I., Brockmann, C., Boettcher, M., Kirches, G., Wevers, J., and Santoro, M.: Land Cover CCI Product User Guide, Tech. rep., European Space Agency, URL https://maps.elie.ucl.ac.be/CCI/viewer/download/ESACCI-LC-Ph2-PUGv2_2.0.pdf, 2017.

Desborough, C. E.: The impact of root weighting on the response of transpiration to moisture stress in land surface schemes, Monthly Weather Review, 125, 1920–1930, doi:10.1175/1520-0493(1997)125<1920:TIORWO>2.0.CO;2, 1997.

Di Gregorio, A. and Jansen, L. J. M.: Land cover classification system: LCCS : Classification concepts and user manual, Food & Agriculture Organization of the United Nations, ISBN 95-5-105327-8, 2005.

DiMiceli, C., Carroll, M., Sohlberg, R., Kim, D., Kelly, M., and Townshend, J.: MOD44B MODIS/Terra Vegetation Continuous Fields Yearly L3 Global 250m SIN Grid V006, doi:10.5067/MODIS/MOD44B.006, 2015.

Dirmeyer, P. A., Koster, R. D., and Guo, Z.: Do global models properly represent the feedback between land and atmosphere?, Journal of Hydrometeorology, 7, 1177–1198, doi:10.1175/JHM532.1, 2006.

Do, H. X., Gudmundsson, L., Leonard, M., and Westra, S.: The Global Streamflow Indices and Metadata Archive (GSIM)-Part 1: The production of a daily streamflow archive and metadata, Earth System Science Data, 10, 765–785, doi:10.5194/essd-10-765-2018, 2018.

do Nascimento, T. V., Rudlang, J., Höge, M., van der Ent, R., Chappon, M., Seibert, J., Hrachowitz, M., and Fenicia, F.: EStreams: An Integrated Dataset and Catalogue of Streamflow, Hydro-Climatic Variables and Landscape Descriptors for Europe, doi:10.31223/X5M39F, 2024.

Donohue, R. J., Roderick, M. L., and McVicar, T. R.: Roots, storms and soil pores: Incorporating key ecohydrological processes into Budyko's hydrological model, Journal of Hydrology, 436-437, 35–50, doi:10.1016/j.jhydrol.2012.02.033, 2012.

Dorigo, W., Wagner, W., Albergel, C., Albrecht, F., Balsamo, G., Brocca, L., Chung, D., Ertl, M., Forkel, M., Gruber, A., Haas, E., Hamer, P. D., Hirschi, M., Ikonen, J., de Jeu, R., Kidd, R., Lahoz, W., Liu, Y. Y., Miralles, D., Mistelbauer, T., Nicolai-Shaw, N., Parinussa, R., Pratola, C., Reimer, C., van der Schalie, R., Seneviratne, S. I., Smolander, T., and Lecomte, P.: ESA CCI Soil Moisture for improved Earth system understanding: State-of-the art and future directions, Remote Sensing of Environment, 203, 185–215, doi:10.1016/j.rse.2017.07.001, 2017.

Döscher, R., Acosta, M., Alessandri, A., Anthoni, P., Arsouze, T., Bergman, T., Bernardello, R., Boussetta, S., Caron, L. P., Carver, G., Castrillo, M., Catalano, F., Cvijanovic, I., Davini, P., Dekker, E., Doblas-Reyes, F. J., Docquier, D., Echevarria, P., Fladrich, U., Fuentes-Franco, R., Gröger, M., Hardenberg, J. V., Hieronymus, J., Karami, M. P., Keskinen, J. P., Koenigk, T., Makkonen, R., Massonnet, F., Ménégoz, M., Miller, P. A., Moreno-Chamarro, E., Nieradzik, L., Van Noije, T., Nolan, P., O'donnell, D., Ollinaho, P., Van Den Oord, G., Ortega, P., Prims, O. T., Ramos, A., Reerink, T., Rousset, C., Ruprich-Robert, Y., Le Sager, P., Schmith, T., Schrödner, R., Serva, F., Sicardi, V., Sloth Madsen, M., Smith, B., Tian, T., Tourigny, E., Uotila, P., Vancoppenolle, M., Wang, S., Wårlind, D., Willén, U., Wyser, K., Yang, S., Yepes-Arbós, X., and Zhang, Q.: The EC-Earth3 Earth system model for the Coupled Model Intercomparison Project 6, Geoscientific Model Development, 15, 2973–3020, doi:10.5194/gmd-15-2973-2022, 2022.

Dralle, D. N., Hahm, W., Rempe, D. M., Karst, N., Anderegg, L. D., Thompson, S. E., Dawson, T. E., and Dietrich, W. E.: Plants as sensors: Vegetation response to rainfall predicts root-zone water storage capacity in Mediterranean-type climates, Environmental Research Letters, 15, doi:10.1088/1748-9326/abb10b, 2020a.

Dralle, D. N., Hahm, W. J., and Rempe, D. M.: Dataset for "Accounting for snow in the estimation of root-zone water storage capacity from precipitation and evapotranspiration fluxes", HydroShare, URL http://www.hydroshare.org/resource/ee45c2f5f13042ca85bcb86bbfc9dd37, 2020b.

Dralle, D. N., Hahm, W. J., Chadwick, K. D., McCormick, E., and Rempe, D. M.: Technical note: Accounting for snow in the estimation of root zone water storage capacity from precipitation and evapotranspiration fluxes, Hydrology and Earth System Sciences, 25, 2861–2867, doi:10.5194/hess-25-2861-2021, 2021.

Dümenil, L. and Todini, E.: A rainfall–runoff scheme for use in the Hamburg climate model, in: Advances in Theoretical Hydrology, edited by O'Kane, J. P, European Geophysical Society Series on Hydrological Sciences, pp. 129–157, Elsevier, Amsterdam, doi:10.1016/B978-0-444-89831-9.50016-8, 1992.

ECMWF: Part IV: Physical Processes, IFS Documentation, URL https://www.ecmwf.int/node/17117, last access: September 2019, 2016.

Engels, C., Mollenkopf, M., and Marschner, H.: Effect of drying and rewetting the topsoil on root growth of maize and rape in different soil depths, Zeitschrift für Pflanzenernährung und Bodenkunde, 157, 139–144, doi:10.1002/jpln.19941570213, 1994.

European Space Agency: Soil Moisture CCI Data v07.1, URL https://www.esa-soilmoisture-cci.org/data, 2022.

Euser, T., Hrachowitz, M., Winsemius, H. C., and Savenije, H. H.: The effect of forcing and landscape distribution on performance and consistency of model structures, Hydrological Processes, 29, 3727–3743, doi:10.1002/hyp.10445, 2015.

Fan, Y.: Are catchments leaky?, WIREs Water, 6, e1386, doi:10.1002/wat2.1386, 2019.

Fan, Y., Miguez-Macho, G., Jobbágy, E. G., Jackson, R. B., and Otero-Casal, C.: Hydrologic regulation of plant rooting depth, Proceedings of the National Academy of Sciences, 114, 10 572–10 577, doi:10.1073/pnas.1712381114, 2017.

FAO: Digital Soil Map of the World (DSMW), Tech. rep., Food and Agricultural Organization of the United Nations, re-issued version, 2003.

FAO: World Food and Agriculture - Statistical Yearbook 2022, FAO, doi:10.4060/cc2211en, 2022.

Faroux, S., Kaptué Tchuenté, A. T., Roujean, J.-L., Masson, V., Martin, E., and Le Moigne, P.: ECOCLIMAP-II/Europe: a twofold database of ecosystems and surface parameters at 1 km resolution based on satellite information for use in land surface, meteorological and climate models, Geoscientific Model Development, 6, 563–582, doi:10.5194/gmd-6-563-2013, 2013.

Feddes, R. A., Hoff, H., Bruen, M., Dawson, T., De Rosnay, P, Dirmeyer, P, Jackson, R. B., Kabat, P., Kleidon, A., Lilly, A., and Pitman, A. J.: Modeling root water uptake in hydrological and climate models, Bulletin of the American Meteorological Society, 82, 2797–2809, doi:10.1175/1520-0477(2001)082<2797:MRWUIH>2.3.CO;2, 2001.

Feng, X., Thompson, S. E., Woods, R., and Porporato, A.: Quantifying Asynchronicity of Precipitation and Potential Evapotranspiration in Mediterranean Climates, Geophysical Research Letters, 46, 14 692–14 701, doi:10.1029/2019GL085653, 2019.

Ferguson, I. M., Jefferson, J. L., Maxwell, R. M., and Kollet, S. J.: Effects of root water uptake formulation on simulated water and energy budgets at local and basin scales, Environmental Earth Sciences, 75, 1–15, doi:10.1007/s12665-015-5041-z, 2016.

Fisher, R. A. and Koven, C. D.: Perspectives on the Future of Land Surface Models and the Challenges of Representing Complex Terrestrial Systems, Journal of Advances in Modeling Earth Systems, 12, doi:10.1029/2018MS001453, 2020.

Fowler, K. J., Acharya, S. C., Addor, N., Chou, C., and Peel, M. C.: CAMELS-AUS: Hydrometeorological time series and landscape attributes for 222 catchments in Australia, Earth System Science Data, 13, 3847–3867, doi:10.5194/essd-13-3847-2021, 2021.

Gao, H., Hrachowitz, M., Schymanski, S. J., Fenicia, F., Sriwongsitanon, N., and Savenije, H.: Climate controls how ecosystems size the root zone storage capacity at catchment scale, Geophysical Research Letters, 41, 7916–7923, doi:10.1002/2014GL061668, 2014.

Gao, H., Ding, Y., Zhao, Q., Hrachowitz, M., and Savenije, H. H.: The importance of aspect for modelling the hydrological response in a glacier catchment in Central Asia, Hydrological Processes, 31, 2842–2859, doi:10.1002/hyp.11224, 2017.

Gao, H., Fenicia, F., and Savenije, H. H. G.: HESS Opinions: Are soils overrated in hydrology?, Hydrology and Earth System Sciences, 27, 2607–2620, doi:10.5194/hess-27-2607-2023, 2023.

Gentine, P., D'Odorico, P., Lintner, B. R., Sivandran, G., and Salvucci, G.: Interdependence of climate, soil, and vegetation as constrained by the Budyko curve, Geophysical Research Letters, 39, 2–7, doi:10.1029/2012GL053492, 2012.

Gerrits, A. M., Pfister, L., and Savenije, H. H.: Spatial and temporal variability of canopy and forest floor interception in a beech forest, Hydrological Processes, 24, 3011–3025, doi:10.1002/hyp.7712, 2010.

Gharari, S., Clark, M. P., Mizukami, N., Wong, J. S., Pietroniro, A., and Wheater, H. S.: Improving the Representation of Subsurface Water Movement in Land Models, Journal of Hydrometeorology, 20, 2401 – 2418, doi:10.1175/JHM-D-19-0108.1, 2019.

Giardina, F., Padrón, R., Stocker, B. D., Schumacher, D., and Seneviratne, S.: Dry biases in land water storage and excessive soil moisture limitation in CMIP6 models, doi:10.21203/rs.3.rs-4086740/v1, 2024.

Goldstein, A., Kapelner, A., Bleich, J., and Pitkin, E.: Peeking Inside the Black Box: Visualizing Statistical Learning With Plots of Individual Conditional Expectation, Journal of Computational and Graphical Statistics, 24, 44–65, doi:10.1080/10618600.2014.907095, 2015.

Grafton, R. Q., Williams, J., Perry, C. J., Molle, F., Ringler, C., Steduto, P., Udall, B., Wheeler, S. A., Wang, Y., Garrick, D., and Allen, R. G.: The paradox of irrigation efficiency, Science, 361, 748–750, doi:10.1126/science.aat9314, 2018.

Grill, G., Lehner, B., Thieme, M., Geenen, B., Tickner, D., Antonelli, F., Babu, S., Borrelli, P., Cheng, L., Crochetiere, H., et al.: Mapping the world's free-flowing rivers, Nature, 569, 215–221, doi:10.1038/s41586-019-1111-9, 2019.

Grogan, D. S., Wisser, D., Prusevich, A., Lammers, R. B., and Frolking, S.: The use and re-use of unsustainable groundwater for irrigation: a global budget, Environmental Research Letters, 12, 034 017, doi:10.1088/1748-9326/aa5fb2, 2017.

Gruber, A., Dorigo, W. A., Crow, W., and Wagner, W.: Triple Collocation-Based Merging of Satellite Soil Moisture Retrievals, IEEE Transactions on Geoscience and Remote Sensing, 55, 6780–6792, doi:10.1109/TGRS.2017.2734070, 2017.

Gudmundsson, L., Do, H. X., Leonard, M., and Westra, S.: The Global Streamflow Indices and Metadata Archive (GSIM)-Part 2: Quality control, time-series indices and homogeneity assessment, Earth System Science Data, 10, 787–804, doi:10.5194/essd-10-787-2018, 2018.

Gumbel, E. J.: Les valeurs extrêmes des distributions statistiques, Annales de l'institut Henri Poincaré, 5, 115–158, 1935.

Guswa, A. J.: The influence of climate on root depth: A carbon cost-benefit analysis, Water Resources Research, 44, 1–11, doi:10.1029/2007WR006384, 2008.

Hagemann, S. and Stacke, T.: Impact of the soil hydrology scheme on simulated soil moisture memory, Climate Dynamics, 44, 1731–1750, doi:10.1007/s00382-014-2221-6, 2015.

Hahm, W. J., Rempe, D. M., Dralle, D. N., Dawson, T. E., Lovill, S. M., Bryk, A. B., Bish, D. L., Schieber, J., and Dietrich, W. E.: Lithologically Controlled Subsurface Critical Zone Thickness and Water Storage Capacity Determine Regional Plant Community Composition, Water Resources Research, 55, 3028–3055, doi:10.1029/2018WR023760, 2019.

Hahm, W. J., Dralle, D. N., Lapides, D. A., Ehlert, R. S., and Rempe, D. M.: Geologic Controls on Apparent Root-Zone Storage Capacity, Water Resources Research, 60, e2023WR035 362, doi:https://doi.org/10.1029/2023WR035362, e2023WR035362 2023WR035362, 2024.

Hargreaves, G. H. and Samani, Z. A.: Estimating potential evapotranspiration, Journal of the irrigation and Drainage Division, 108, 225–230, 1982.

Hengl, T., Mendes de Jesus, J., Heuvelink, G. B. M., Ruiperez Gonzalez, M., Kilibarda, M., Blagotić, A., Shangguan, W., Wright, M. N., Geng, X., Bauer-Marschallinger, B., Guevara, M. A., Vargas, R., MacMillan, R. A., Batjes, N. H., Leenaars, J. G. B., Ribeiro, E., Wheeler, I., Mantel, S., and Kempen, B.: SoilGrids250m:

Global gridded soil information based on machine learning, PLOS ONE, 12, 1–40, doi:10.1371/journal.pone.0169748, 2017.

Hersbach, H., Bell, B., Berrisford, P., Hirahara, S., Horányi, A., Muñoz-Sabater, J., Nicolas, J., Peubey, C., Radu, R., Schepers, D., Simmons, A., Soci, C., Abdalla, S., Abellan, X., Balsamo, G., Bechtold, P., Biavati, G., Bidlot, J., Bonavita, M., De Chiara, G., Dahlgren, P., Dee, D., Diamantakis, M., Dragani, R., Flemming, J., Forbes, R., Fuentes, M., Geer, A., Haimberger, L., Healy, S., Hogan, R. J., Hólm, E., Janisková, M., Keeley, S., Laloyaux, P., Lopez, P., Lupu, C., Radnoti, G., de Rosnay, P., Rozum, I., Vamborg, F., Villaume, S., and Thépaut, J. N.: The ERA5 global reanalysis, Quarterly Journal of the Royal Meteorological Society, 146, 1999–2049, doi:10.1002/qj.3803, 2020.

Herwitz, S. R.: Interception storage capacities of tropical rainforest canopy trees, Journal of Hydrology, 77, 237–252, doi:10.1016/0022-1694(85)90209-4, 1985.

Hobeichi, S., Abramowitz, G., Evans, J., and Ukkola, A.: Derived Optimal Linear Combination Evapotranspiration (DOLCE): A global gridded synthesis et estimate, Hydrology and Earth System Sciences, 22, 1317–1336, doi:10.5194/hess-22-1317-2018, 2018.

Hobeichi, S., Abramowitz, G., and Evans, J. P.: Robust historical evapotranspiration trends across climate regimes, Hydrology and Earth System Sciences, 25, 3855–3874, doi:10.5194/hess-25-3855-2021, 2021.

Holsinger, L., Parks, S. A., Parisien, M.-A., Miller, C., Batllori, E., and Moritz, M. A.: Climate change likely to reshape vegetation in North America's largest protected areas, Conservation Science and Practice, 1, e50, doi:10.1111/csp2.50, 2019.

Hrachowitz, M., Stockinger, M., Coenders-Gerrits, M., Van Der Ent, R., Bogena, H., Lücke, A., and Stumpp, C.: Reduction of vegetation-accessible water storage capacity after deforestation affects catchment travel time distributions and increases young water fractions in a headwater catchment, Hydrology and Earth System Sciences, 25, 4887–4915, doi:10.5194/hess-25-4887-2021, 2021.

Huang, Z., Hejazi, M., Li, X., Tang, Q., Vernon, C., Leng, G., Liu, Y., Döll, P., Eisner, S., Gerten, D., Hanasaki, N., and Wada, Y.: Reconstruction of global gridded monthly sectoral water withdrawals for 1971-2010 and analysis of their spatiotemporal patterns, Hydrology and Earth System Sciences, 22, 2117–2133, doi:10.5194/hess-22-2117-2018, 2018.

Hut, R., Drost, N., van de Giesen, N., van Werkhoven, B., Abdollahi, B., Aerts, J., Albers, T., Alidoost, F., Andela, B., Camphuijsen, J., Dzigan, Y., van Haren, R., Hutton, E., Kalverla, P., van Meersbergen, M., van den Oord, G., Pelupessy, I., Smeets, S., Verhoeven, S., de Vos, M., and Weel, B.: The eWaterCycle platform for open and FAIR hydrological collaboration, Geoscientific Model Development, 15, 5371–5390, doi:10.5194/gmd-15-5371-2022, 2022.

Jackson, R. B., Canadell, J., Ehleringer, J. R., Mooney, H. A., Sala, O. E., and Schulze, E. D.: A global analysis of root distributions for terrestrial biomes, Oecologia, 108, 389–411, doi:10.1007/BF00333714, 1996.

Jägermeyr, J., Gerten, D., Heinke, J., Schaphoff, S., Kummu, M., and Lucht, W.: Water savings potentials of irrigation systems: global simulation of processes and linkages, Hydrology and Earth System Sciences, 19, 3073–3091, doi:10.5194/hess-19-3073-2015, 2015.

Jeffrey, S. J., Carter, J. O., Moodie, K. B., and Beswick, A. R.: Using spatial interpolation to construct a comprehensive archive of Australian climate data, Environmental Modelling and Software, 16, 309 – 330, doi:10.1016/S1364-8152(01)00008-1, 2001.

Jha, S. K., Gao, Y., Liu, H., Huang, Z., Wang, G., Liang, Y., and Duan, A.: Root development and water uptake in winter wheat under different irrigation methods and scheduling for North China, Agricultural Water Management, 182, 139–150, doi:10.1016/j.agwat.2016.12.015, 2017.

Johannsen, F., Ermida, S., Martins, J. P., Trigo, I. F., Nogueira, M., and Dutra, E.: Cold bias of ERA5 summertime daily maximum land surface temperature over Iberian Peninsula, Remote Sensing, 11, doi:10.3390/rs11212570, 2019.

Jung, M., Koirala, S., Weber, U., Ichii, K., Gans, F., Camps-Valls, G., Papale, D., Schwalm, C., Tramontana, G., and Reichstein, M.: The FLUXCOM ensemble of global land-atmosphere energy fluxes, Scientific data, 6, 74, doi:10.1038/s41597-019-0076-8, 2019.

Ke, Y., Leung, L. R., Huang, M., and Li, H.: Enhancing the representation of subgrid land surface characteristics in land surface models, Geoscientific Model Development, 6, 1609–1622, doi:10.5194/gmd-6-1609-2013, 2013.

Kim, H.: Global Soil Wetness Project Phase 3 Atmospheric Boundary Conditions (Experiment 1) [Data set], Data Integration and Analysis System (DIAS), doi:10.20783/DIAS.501, 2017.

Kleidon, A.: Global datasets of rooting zone depth inferred from inverse methods, Journal of Climate, 17, 2714–2722, doi:10.1175/1520-0442(2004)017<2714:GDORZD>2.0.CO;2, 2004.

Kleidon, A. and Heimann, M.: A method of determining rooting depth from a terrestrial biosphere model and its impacts on the global water and carbon cycle, Global Change Biology, 4, 275–286, doi:10.1046/j.1365-2486.1998.00152.x, 1998.

Klein Goldewijk, K., Beusen, A., van Drecht, G., and de Vos, M.: The HYDE 3.1 spatially explicit database of human-induced global land-use change over the past 12,000 years, Global Ecology and Biogeography, 20, 73–86, doi:10.1111/j.1466-8238.2010.00587.x, 2011.

Klepper, B.: Crop root system response to irrigation, Irrigation Science, 12, 105–108, doi:10.1007/BF00192280, 1991.

Klingler, C., Schulz, K., and Herrnegger, M.: LamaH-CE: LArge-SaMple DAta for Hydrology and Environmental Sciences for Central Europe, Earth System Science Data, 13, 4529–4565, doi:10.5194/essd-13-4529-2021, 2021.

Krinner, G., Viovy, N., de Noblet-Ducoudré, N., Ogée, J., Polcher, J., Friedlingstein, P., Ciais, P., Sitch, S., and Prentice, I. C.: A dynamic global vegetation model for studies of the coupled atmosphere-biosphere system, Global Biogeochemical Cycles, 19, 1–33, doi:10.1029/2003GB002199, 2005.

Kumar, S. V., Mocko, D. M., Wang, S., Peters-Lidard, C. D., and Borak, J.: Assimilation of remotely sensed leaf area index into the noah-mp land surface model: Impacts on water and carbon fluxes and states over the continental United States, Journal of Hydrometeorology, 20, 1359–1377, doi:10.1175/JHM-D-18-0237.1, 2019.

Kuppel, S., Fan, Y., and Jobbágy, E. G.: Seasonal hydrologic buffer on continents: Patterns, drivers and ecological benefits, Advances in Water Resources, 102, 178–187, doi:10.1016/j.advwatres.2017.01.004, 2017.

Laio, F., D'Odorico, P., and Ridolfi, L.: An analytical model to relate the vertical root distribution to climate and soil properties, Geophysical Research Letters, 33, doi:10.1029/2006GL027331, 2006.

Lange, S. and Büchner, M.: ISIMIP2a atmospheric climate input data, doi:10.48364/ISIMIP.886955, 2020.

Lankford, B., Closas, A., Dalton, J., López Gunn, E., Hess, T., Knox, J. W., van der Kooij, S., Lautze, J., Molden, D., Orr, S., Pittock, J., Richter, B., Riddell, P. J., Scott, C. A., philippe Venot, J., Vos, J., and Zwarteveen, M.: A scale-based framework to understand the promises, pitfalls and paradoxes of irrigation efficiency to meet major water challenges, Global Environmental Change, 65, 102 182, doi:10.1016/j.gloenvcha.2020.102182, 2020.

Le Moigne, P.: SURFEX scientific documentation, Groupe de météorologie a moyenne échelle, p. 237, URL http://www.cnrm.meteo.fr/surfex/IMG/pdf/surfex_scidoc_v2.pdf, 2012.

Lehner, B., Verdin, K., and Jarvis, A.: New Global Hydrography Derived From Spaceborne Elevation Data, Eos, Transactions American Geophysical Union, 89, 93–94, doi:https://doi.org/10.1029/2008EO100001, 2008.

Lendvai, A.: Portale dei dati idrologici italiani, URL http://meteoniardo.altervista.org/, last access: August 2023, 2020.

Ling, X. L., Fu, C. B., Guo, W. D., and Yang, Z. L.: Assimilation of Remotely Sensed LAI Into CLM4CN Using DART, Journal of Advances in Modeling Earth Systems, 11, 2768–2786, doi:10.1029/2019MS001634, 2019.

Liu, X., Chen, F., Barlage, M., and Niyogi, D.: Implementing Dynamic Rooting Depth for Improved Simulation of Soil Moisture and Land Surface Feedbacks in Noah-MP-Crop, Journal of Advances in Modeling Earth Systems, 12, e2019MS001 786, doi:10.1029/2019MS001786, 2020.

Liu, Y., Dorigo, W., Parinussa, R., de Jeu, R., Wagner, W., McCabe, M., Evans, J., and van Dijk, A.: Trend-preserving blending of passive and active microwave soil moisture retrievals, Remote Sensing of Environment, 123, 280–297, doi:10.1016/j.rse.2012.03.014, 2012.

Lo Gullo, M. A., Nardini, A., Salleo, S., and Tyree, M. T.: Changes in root hydraulic conductance (KR) of Olea oleaster seedlings following drought stress and irrigation, New Phytologist, 140, 25–31, doi:10.1046/j.1469-8137.1998.00258.x, 1998.

Loveland, T. R., Reed, B. C., Ohlen, D. O., Brown, J. F., Zhu, Z., Yang, L., and Merchant, J. W.: Development of a global land cover characteristics database and IGBP DIS-Cover from 1 km AVHRR data, International Journal of Remote Sensing, 21, 1303–1330, doi:10.1080/014311600210191, 2000.

Lv, G., Kang, Y., Li, L., and Wan, S.: Effect of irrigation methods on root development and profile soil water uptake in winter wheat, Irrigation Science, 28, 387–398, doi:10.1007/s00271-009-0200-1, 2010.

Ma, N., Szilagyi, J., and Jozsa, J.: Benchmarking large-scale evapotranspiration estimates: A perspective from acalibration-freecomplementary relationship approach and FLUXCOM, Journal of Hydrology, 590, 125–221, doi:10.1016/j.jhydrol.2020.125221, 2020.

Maan, C., ten Veldhuis, M.-C., and van de Wiel, B. J. H.: Dynamic root growth in response to depth-varying soil moisture availability: a rhizobox study, Hydrology and Earth System Sciences, 27, 2341–2355, doi:10.5194/hess-27-2341-2023, 2023.

Mahfouf, J. F., Ciret, C., Ducharne, A., Irannejad, P., Noilhan, J., Shao, Y., Thornton, P., Xue, Y., and Yang, Z. L.: Analysis of transpiration results from the RICE and PILPS workshop, Global and Planetary Change, 13, 73–88, doi:10.1016/0921-8181(95)00039-9, 1996.

Martens, B., Miralles, D. G., Lievens, H., Van Der Schalie, R., De Jeu, R. A., Fernández-Prieto, D., Beck, H. E., Dorigo, W. A., and Verhoest, N. E.: GLEAM v3: Satellite-based land evaporation and root-zone soil moisture, Geoscientific Model Development, 10, 1903–1925, doi:10.5194/gmd-10-1903-2017, 2017.

McCormick, E. L., Dralle, D. N., Hahm, W. J., Tune, A. K., Schmidt, L. M., Chadwick, K. D., and Rempe, D. M.: Widespread woody plant use of water stored in bedrock, Nature, 597, 225–229, doi:10.1038/s41586-021-03761-3, 2021.

McDermid, S., Nocco, M., Lawston-Parker, P., Keune, J., Pokhrel, Y., Jain, M., Jägermeyr, J., Brocca, L., Massari, C., Jones, A. D., Vahmani, P., Thiery, W., Yao, Y., Bell, A., Chen, L., Dorigo, W., Hanasaki, N., Jasechko, S., Lo, M.-H., Mahmood, R., Mishra, V., Mueller, N. D., Niyogi, D., Rabin, S. S., Sloat, L., Wada, Y., Zappa, L., Chen, F., Cook, B. I., Kim, H., Lombardozzi, D., Polcher, J., Ryu, D., Santanello, J., Satoh, Y., Seneviratne, S., Singh, D., and Yokohata, T.: Irrigation in the Earth system, Nature Reviews Earth & Environment, doi:10.1038/s43017-023-00438-5, 2023.

Meier, J., Zabel, F., and Mauser, W.: A global approach to estimate irrigated areas - A comparison between different data and statistics, Hydrology and Earth System Sciences, 22, 1119–1133, doi:10.5194/hess-22-1119-2018, 2018.

Mines ParisTech Solar radiation Data: Extraterrestrial irradiance (e0) and top of atmosphere (toa) radiation, URL http://www.soda-pro.com/web-services/radiation/extraterrestrial-irradiance-and-toa, last access: September 2019, 2016.

Miralles, D. G., De Jeu, R. A., Gash, J. H., Holmes, T. R., and Dolman, A. J.: Magnitude and variability of land evaporation and its components at the global scale, Hydrology and Earth System Sciences, 15, 967–981, doi:10.5194/hess-15-967-2011, 2011.

Miralles, D. G., Brutsaert, W., Dolman, A. J., and Gash, J. H.: On the Use of the Term "Evapotranspiration", Water Resources Research, 56, e2020WR028 055, doi:10.1029/2020WR028055, 2020.

Méndez-Barroso, L. A., Vivoni, E. R., Watts, C. J., and Rodríguez, J. C.: Seasonal and interannual relations between precipitation, surface soil moisture and vegetation dynamics in the North American monsoon region, Journal of Hydrology, 377, 59–70, doi:10.1016/j.jhydrol.2009.08.009, 2009.

Nelson, J. A., Pérez-Priego, O., Zhou, S., Poyatos, R., Zhang, Y., Blanken, P. D., Gimeno, T. E., Wohlfahrt, G., Desai, A. R., Gioli, B., Limousin, J. M., Bonal, D., Paul-Limoges, E., Scott, R. L., Varlagin, A., Fuchs, K., Montagnani, L., Wolf, S., Delpierre, N., Berveiller, D., Gharun, M., Belelli Marchesini, L., Gianelle, D., Šigut, L., Mammarella, I., Siebicke, L., Andrew Black, T., Knohl, A., Hörtnagl, L., Magliulo, V., Besnard, S., Weber, U., Carvalhais, N., Migliavacca, M., Reichstein, M., and Jung, M.: Ecosystem transpiration and evaporation: Insights from three water flux partitioning methods across FLUXNET sites, Global Change Biology, 26, 6916–6930, doi:10.1111/gcb.15314, 2020.

Nijzink, R., Hutton, C., Pechlivanidis, I., Capell, R., Arheimer, B., Freer, J., Han, D., Wagener, T., McGuire, K., Savenije, H., and Hrachowitz, M.: The evolution of root-zone moisture capacities after deforestation: a step towards hydrological predictions under change?, Hydrology and Earth System Sciences, 20, 4775–4799, doi:10.5194/hess-20-4775-2016, 2016.

Nogueira, M., Albergel, C., Boussetta, S., Johannsen, F., Trigo, I. F., Ermida, S. L., Martins, J. P., and Dutra, E.: Role of vegetation in representing land surface temperature in the CHTESSEL (CY45R1) and SURFEX-ISBA (v8.1) land surface models: A case study over Iberia, Geoscientific Model Development, 13, 3975–3993, doi:10.5194/gmd-13-3975-2020, 2020.

Nogueira, M., Boussetta, S., Balsamo, G., Albergel, C., Trigo, I. F., Johannsen, F., Miralles, D. G., and Dutra, E.: Upgrading Land-Cover and Vegetation Seasonality in the ECMWF Coupled System: Verification With FLUXNET Sites, METEOSAT Satellite Land Surface Temperatures, and ERA5 Atmospheric Reanalysis, Journal of Geophysical Research: Atmospheres, 126, 1–26, doi:10.1029/2020JD034163, 2021.

Norby, R. and Jackson, R.: Root dynamics and global change: seeking an ecosystem perspective, New Phytologist, 147, 1–2, doi:10.1046/j.1469-8137.2000.00674.x, 2000.

Oldroyd, G. E. D. and Leyser, O.: A plant's diet, surviving in a variable nutrient environment, Science, 368, eaba0196, doi:10.1126/science.aba0196, 2020.

Oudin, L., Andréassian, V., Perrin, C., and Anctil, F.: Locating the sources of low-pass behavior within rainfall-runoff models, Water Resources Research, 40, W11101, doi:10.1029/2004WR003291, 2004.

Pacholczyk, P. and Verger, A.: GEOV2 AVHRR Product User Manual, Tech. rep., URL https://www.theia-land.fr/wp-content/uploads/2020/11/THEIA-MU-44-0369-CNES-GEOV2-AVHRR-Product-User-Manual-V2.pdf, 2020.

Pan, N., Feng, X., Fu, B., Wang, S., Ji, F., and Pan, S.: Increasing global vegetation browning hidden in overall vegetation greening: Insights from time-varying trends, Remote Sensing of Environment, 214, 59–72, doi:10.1016/j.rse.2018.05.018, 2018.

Pan, S., Pan, N., Tian, H., Friedlingstein, P., Sitch, S., Shi, H., Arora, V. K., Haverd, V., Jain, A. K., Kato, E., Lienert, S., Lombardozzi, D., Ottle, C., Poulter, B., and Zaehle, S.: Evaluation of global terrestrial evapotranspiration by state-of-the-art approaches in remote sensing, machine learning, and land surface models, Hydrology and Earth System Sciences, 24, 1485–1509, doi:10.5194/hess-2019-409, 2020.

Pastorello, G., Trotta, C., Canfora, E., et al.: The FLUXNET2015 dataset and the ONEFlux processing pipeline for eddy covariance data, Scientific Data, 7, 225, doi:10.1038/s41597-020-0534-3, 2020.

Pitman, A. J.: The evolution of, and revolution in, land surface schemes designed for climate models, International Journal of Climatology, 23, 479–510, doi:10.1002/joc.893, 2003.

Poulter, B., MacBean, N., Hartley, A., Khlystova, I., Arino, O., Betts, R., Bontemps, S., Boettcher, M., Brockmann, C., Defourny, P., Hagemann, S., Herold, M., Kirches, G., Lamarche, C., Lederer, D., Ottlé, C., Peters, M., and Peylin, P.: Plant functional type classification for earth system models: Results from the European Space Agency's Land Cover Climate Change Initiative, Geoscientific Model Development, 8, 2315–2328, doi:10.5194/gmd-8-2315-2015, 2015.

Rahman, A., Zhang, X., Xue, Y., Houser, P., Sauer, T., Kumar, S., Mocko, D., and Maggioni, V.: A synthetic experiment to investigate the potential of assimilating LAI through direct insertion in a land surface model, Journal of Hydrology X, 9, 100 063, doi:10.1016/j.hydroa.2020.100063, 2020.

Rahman, A., Zhang, X., Houser, P., Sauer, T., and Maggioni, V.: Global Assimilation of Remotely Sensed Leaf Area Index: The Impact of Updating More State Variables Within a Land Surface Model, Frontiers in Water, 3, 1–15, doi:10.3389/frwa.2021.789352, 2022.

Raoult, N., Ruscica, R. C., Salvia, M. M., and Sörensson, A. A.: Soil Moisture Drydown Detection Is Hindered by Model-Based Rescaling, IEEE Geoscience and Remote Sensing Letters, 19, doi:10.1109/LGRS.2022.3178685, 2022.

Read, J. and Stokes, A.: Plant biomechanics in an ecological context, American Journal of Botany, 93, 1546–1565, doi:10.3732/ajb.93.10.1546, 2006.

Roodari, A., Hrachowitz, M., Hassanpour, F., and Yaghoobzadeh, M.: Signatures of human intervention-or not? Downstream intensification of hydrological drought along a large Central Asian river: The individual roles of climate variability and land use change, Hydrology and Earth System Sciences, 25, 1943–1967, doi:10.5194/hess-25-1943-2021, 2021.

Ryu, Y., Nilson, T., Kobayashi, H., Sonnentag, O., Law, B. E., and Baldocchi, D. D.: On the correct estimation of effective leaf area index: Does it reveal information on clumping effects?, Agricultural and Forest Meteorology, 150, 463–472, doi:10.1016/j.agrformet.2010.01.009, 2010.

Sakschewski, B., von Bloh, W., Drüke, M., Sörensson, A., Ruscica, R., Langerwisch, F., Billing, M., Bereswill, S., Hirota, M., Oliveira, R., Heinke, J., and Thonicke, K.: Variable tree rooting strategies improve tropical productivity and evapotranspiration in a dynamic global vegetation model, Biogeosciences Discussions, pp. 1–35, doi:10.5194/bg-2020-97, 2020.

Savenije, H. H.: The importance of interception and why we should delete the term evapotranspiration from our vocabulary, Hydrological processes, 18, 1507–1511, doi:10.1002/hyp.5563, 2004.

Savenije, H. H. and Hrachowitz, M.: HESS Opinions "catchments as meta-organisms - A new blueprint for hydrological modelling", Hydrology and Earth System Sciences, 21, 1107–1116, doi:10.5194/hess-21-1107-2017, 2017.

Schenk, H. and Jackson, R.: Global Distribution of Root Profiles in Terrestrial Ecosystems, doi:10.3334/ORNLDAAC/660, 2003.

Schenk, H., Jackson, R., Hall, F., Collatz, G., Meeson, B., Los, S., Colstoun, E. D., and Landis, D.: ISLSCP II Ecosystem Rooting Depths, doi:10.3334/ORNLDAAC/929, 2009.

Schenk, H. J. and Jackson, R. B.: Rooting depths, lateral root spreads and belowground/above-ground allometries of plants in water-limited ecosystems, Journal of Ecology, 90, 480–494, doi:10.1046/j.1365-2745.2002.00682.x, 2002a.

Schenk, H. J. and Jackson, R. B.: The Global Biogeography of Roots, Ecological Monographs, 72, 311–328, doi:10.1890/0012-9615(2002)072[0311:TGBOR]2.0.CO;2, 2002b.

Schlesinger, W. H. and Jasechko, S.: Transpiration in the global water cycle, Agricultural and Forest Meteorology, 189-190, 115 – 117, doi:10.1016/j.agrformet.2014.01.011, 2014.

Schulzweida, U.: CDO User Guide, Max Planck Institute for Meteorology, doi:10.5281/zenodo.3539275, 2022.

Seneviratne, S. I., Koster, R. D., Guo, Z., Dirmeyer, P. A., Kowalczyk, E., Lawrence, D., Liu, P., Lu, C. H., Mocko, D., Oleson, K. W., and Verseghy, D.: Soil moisture memory in AGCM simulations: Analysis of global land-atmosphere coupling experiment (GLACE) data, Journal of Hydrometeorology, 7, 1090–1112, doi:10.1175/JHM533.1, 2006.

Seneviratne, S. I., Corti, T., Davin, E. L., Hirschi, M., Jaeger, E. B., Lehner, I., Orlowsky, B., and Teuling, A. J.: Investigating soil moisture-climate interactions in a changing climate: A review, Earth-Science Reviews, 99, 125–161, doi:10.1016/j.earscirev.2010.02.004, 2010.

Siebert, S., Burke, J., Faures, J. M., Frenken, K., Hoogeveen, J., Döll, P., and Portmann, F. T.: Groundwater use for irrigation - A global inventory, Hydrology and Earth System Sciences, 14, 1863–1880, doi:10.5194/hess-14-1863-2010, 2010.

Siebert, S., Kummu, M., Porkka, M., Döll, P., Ramankutty, N., and Scanlon, B. R.: A global data set of the extent of irrigated land from 1900 to 2005, Hydrology and Earth System Sciences, 19, 1521–1545, doi:10.5194/hess-19-1521-2015, 2015.

Singh, C., Wang-Erlandsson, L., Fetzer, I., Rockström, J., and Van Der Ent, R.: Rootzone storage capacity reveals drought coping strategies along rainforest-savanna transitions, Environmental Research Letters, 15, doi:10.1088/1748-9326/abc377, 2020.

Sivandran, G. and Bras, R. L.: Dynamic root distributions in ecohydrological modeling: A case study at Walnut Gulch Experimental Watershed, Water Resources Research, 49, 3292–3305, doi:10.1002/wrcr.20245, 2013.

Speich, M. J., Lischke, H., and Zappa, M.: Testing an optimality-based model of rooting zone water storage capacity in temperate forests, Hydrology and Earth System Sciences, 22, 4097–4124, doi:10.5194/hess-22-4097-2018, 2018.

Stocker, B. D., Tumber-Dávila, S. J., Konings, A. G., Anderson, M. C., Hain, C., and Jackson, R. B.: Global patterns of water storage in the rooting zones of vegetation, Nature geoscience, 16, 250–256, doi:10.1038/s41561-023-01125-2, 2023.

Tempel, N. T., Bouaziz, L., Taormina, R., van Noppen, E., Stam, J., Sprokkereef, E., and Hrachowitz, M.: Vegetation Response to Climatic Variability: Implications for Root Zone Storage and Streamflow Predictions, EGUsphere, 2024, 1–42, doi:10.5194/egusphere-2024-115, 2024.

Teuling, A. J., Seneviratne, S. I., Williams, C., and Troch, P. A.: Observed timescales of evapotranspiration response to soil moisture, Geophysical Research Letters, 33, L23403, doi:10.1029/2006GL028178, 2006a.

Teuling, A. J., Uijlenhoet, R., Hupet, F., and Troch, P. A.: Impact of plant water uptake strategy on soil moisture and evapotranspiration dynamics during drydown, Geophysical Research Letters, 33, doi:10.1029/2005GL025019, 2006b.

Teuling, A. J., Hirschi, M., Ohmura, A., Wild, M., Reichstein, M., Ciais, P., Buchmann, N., Ammann, C., Montagnani, L., Richardson, A. D., Wohlfahrt, G., and Seneviratne, S. I.: A regional perspective on trends in continental evaporation, Geophysical Research Letters, 36, doi:10.1029/2008GL036584, 2009.

Ukkola, A. M., De Kauwe, M. G., Pitman, A. J., Best, M. J., Abramowitz, G., Haverd, V., Decker, M., and Haughton, N.: Land surface models systematically overestimate the intensity, duration and magnitude of seasonal-scale evaporative droughts, Environmental Research Letters, 11, doi:10.1088/1748-9326/11/10/104012, 2016.

van den Hurk, B. and Viterbo, P.: The Torne-Kalix PILPS 2(e) experiment as a test bed for modifications to the ECMWF land surface scheme, Global and Planetary Change, 38, 165–173, doi:10.1016/S0921-8181(03)00027-4, 2003.

van den Hurk, B., Viterbo, P., Beljaars, A., and Betts, A.: Offline validation of the ERA40 surface scheme, doi:10.21957/9aoaspz8, 2000.

van den Hurk, B., Kim, H., Krinner, G., Seneviratne, S. I., Derksen, C., Oki, T., Douville, H., Colin, J., Ducharne, A., Cheruy, F., Viovy, N., Puma, M. J., Wada, Y., Li, W., Jia, B., Alessandri, A., Lawrence, D. M., Weedon, G. P., Ellis, R., Hagemann, S., Mao, J., Flanner, M. G., Zampieri, M., Materia, S., Law, R. M., and Sheffield, J.: LS3MIP (v1.0) contribution to CMIP6: the Land Surface, Snow and Soil moisture Model Intercomparison Project – aims, setup and expected outcome, Geoscientific Model Development, 9, 2809–2832, doi:10.5194/gmd-9-2809-2016, 2016.

Van Genuchten, M. T.: A closed-form equation for predicting the hydraulic conductivity of unsaturated soils 1, Soil science society of America journal, 44, 892–898, doi:10.2136/sssaj1980.03615995004400050002x, 1980.

Van Oorschot, F., Van Der Ent, R. J., Hrachowitz, M., and Alessandri, A.: Climate-controlled root zone parameters show potential to improve water flux simulations by land surface models, Earth System Dynamics, 12, 725–743, doi:10.5194/esd-12-725-2021, 2021.

van Oorschot, F., van der Ent, R. J., Alessandri, A., and Hrachowitz, M.: Influence of irrigation on root zone storage capacity estimation, Hydrology and Earth System Sciences, 28, 2313–2328, doi:10.5194/hess-28-2313-2024, 2024.

Verger, A., Baret, F., and Weiss, M.: Near real-time vegetation monitoring at global scale, IEEE Journal of Selected Topics in Applied Earth Observations and Remote Sensing, 7, 3473–3481, doi:10.1109/JSTARS.2014.2328632, 2014.

Verger, A., Baret, F., and Weiss, M.: Vegetation and Energy Algorithm Theoretical Basis Document, Copernicus Global Land Operations, pp. 1–93, URL https://land.copernicus.eu/global/sites/cgls.vito.be/files/products/CGLOPS1_ATBD_LAI1km-V2_I1.41.pdf, 2019.

Wang, J., Du, G., Tian, J., Zhang, Y., Jiang, C., and Zhang, W.: Effect of irrigation methods on root growth, root-shoot ratio and yield components of cotton by regulating the

growth redundancy of root and shoot, Agricultural Water Management, 234, 106 120, doi:10.1016/j.agwat.2020.106120, 2020.

Wang, S., Hrachowitz, M., and Schoups, G.: Multi-decadal fluctuations in root zone storage capacity through vegetation adaptation to hydro-climatic variability has minor effects on the hydrological response in the Neckar basin, Germany, Hydrology and Earth System Sciences Discussions, 2024, 1–34, doi:10.5194/hess-2024-62, 2024.

Wang, Y., Zeng, Y., Yu, L., Yang, P., Van der Tol, C., Yu, Q., Lü, X., Cai, H., and Su, Z.: Integrated modeling of canopy photosynthesis, fluorescence, and the transfer of energy, mass, and momentum in the soil–plant–atmosphere continuum (STEMMUS–SCOPE v1.0.0), Geoscientific Model Development, 14, 1379–1407, doi:10.5194/gmd-14-1379-2021, 2021.

Wang-Erlandsson, L., Bastiaanssen, W. G., Gao, H., Jagermeyr, J., Senay, G. B., Van Dijk, A. I., Guerschman, J. P., Keys, P. W., Gordon, L. J., and Savenije, H. H.: Global root zone storage capacity from satellite-based evaporation, Hydrology and Earth System Sciences, 20, 1459–1481, doi:10.5194/hess-20-1459-2016, 2016.

Wartenburger, R., Seneviratne, S. I., Hirschi, M., Chang, J., Ciais, P., Deryng, D., Elliott, J., Folberth, C., Gosling, S. N., Gudmundsson, L., Henrot, A.-J., Hickler, T., Ito, A., Khabarov, N., Kim, H., Leng, G., Liu, J., Liu, X., Masaki, Y., Morfopoulos, C., Müller, C., Schmied, H. M., Nishina, K., Orth, R., Pokhrel, Y., Pugh, T. A. M., Satoh, Y., Schaphoff, S., Schmid, E., Sheffield, J., Stacke, T., Steinkamp, J., Tang, Q., Thiery, W., Wada, Y., Wang, X., Weedon, G. P., Yang, H., and Zhou, T.: Evapotranspiration simulations in ISIMIP2a—Evaluation of spatio-temporal characteristics with a comprehensive ensemble of independent datasets, Environmental Research Letters, 13, 075 001, doi:10.1088/1748-9326/aac4bb, 2018.

Wei, Z., Yoshimura, K., Wang, L., Miralles, D. G., Jasechko, S., and Lee, X.: Revisiting the contribution of transpiration to global terrestrial evapotranspiration, Geophysical Research Letters, 44, 2792–2801, doi:10.1002/2016GL072235, 2017.

Yamazaki, D., Ikeshima, D., Tawatari, R., Yamaguchi, T., O'Loughlin, F., Neal, J. C., Sampson, C. C., Kanae, S., and Bates, P. D.: A high-accuracy map of global terrain elevations, Geophysical Research Letters, 44, 5844–5853, doi:10.1002/2017GL072874, 2017.

Yang, Y., Donohue, R. J., and McVicar, T. R.: Global estimation of effective plant rooting depth: Implications for hydrological modeling, Water Resources Research, 52, 8260–8276, doi:10.1002/2016WR019392, 2016.

Zeng, X., Dai, Y. J., Dickinson, R. E., and Shaikh, M.: The role of root distribution for climate simulation over land, Geophysical Research Letters, 25, 4533–4536, doi:10.1029/1998GL900216, 1998.

Zhang, J., Wang, J., Chen, J., Song, H., Li, S., Zhao, Y., Tao, J., and Liu, J.: Soil Moisture Determines Horizontal and Vertical Root Extension in the Perennial Grass Lolium perenne L. Growing in Karst Soil, Frontiers in Plant Science, 10, doi:10.3389/fpls.2019.00629, 2019.

Zhang, K., Li, X., Zheng, D., Zhang, L., and Zhu, G.: Estimation of Global Irrigation Water Use by the Integration of Multiple Satellite Observations, Water Resources Research, 58, 1–23, doi:10.1029/2021WR030031, 2022.

Zhang, L., Dawes, W. R., and Walker, G. R.: Response of mean annual evapotranspiration to vegetation changes at catchment scale, Water Resources Research, 37, 701–708, doi:10.1029/2000WR900325, 2001.

Zhang, L., Hu, Z., Fan, J., Zhou, D., and Tang, F.: A meta-analysis of the canopy light extinction coefficient in terrestrial ecosystems, Frontiers of earth science, 8, 599–609, doi:10.1007/s11707-014-0446-7, 2014.

Zhang, Y., Chiew, F. H. S., Peña-Arancibia, J., Sun, F., Li, H., and Leuning, R.: Global variation of transpiration and soil evaporation and the role of their major climate drivers, Journal of Geophysical Research: Atmospheres, 122, 6868–6881, doi:10.1002/2017JD027025, 2017.

Zhao, J., Xu, Z., and Singh, V. P.: Estimation of root zone storage capacity at the catchment scale using improved Mass Curve Technique, Journal of Hydrology, doi:10.1016/j.jhydrol.2016.07.013, 2016.

SUPPORTING INFORMATION OVERVIEW

The supporting information of chapter 2, 3, 4, 5, and 6 can be accessed on the TU Delft repository.

SUPPORTING CONTENTS

LIST OF SUPPORTING FIGURES

LIST OF SUPPORTING TABLES

SUMMARY

Vegetation strongly influences evaporation from land by transporting water from the subsurface to the atmosphere through root water uptake. The amount and timing of this water flux depends on the aboveground (e.g., the amount of leaves) and belowground (e.g., the root extent) characteristics of the vegetation. Although these vegetation characteristics vary strongly both in space and time, there is lack of adequate representation of this vegetation variability in large scale hydrological and land surface models. This causes deficiencies in representing the associated variability in modeled water and energy states and fluxes, which introduces uncertainties in future predictions of the hydrological cycle, including hydrological extremes such as droughts and floods. To address this issue, this research aims to develop more realistic model representations of spatial and temporal vegetation variability, and explore their potential for improving modeled water fluxes in large scale hydrological and land surface models.

Chapter 2 focuses on model representations of spatial and temporal variability of aboveground vegetation characteristics based on satellite remote sensing data. Interannual variability of land cover and leaf area index (LAI) from latest global remote sensing datasets are integrated into the land surface model Hydrology Tiled ECMWF Scheme for Surface Exchanges over Land (HTESSEL). Furthermore, datasets of LAI and the fraction of green vegetation cover are used to develop and integrate a spatially and temporally varying model parameterization of the effective vegetation cover. The effects of these three implementations on simulated hydrology are evaluated using offline (land-only) model simulations. The results show that the enhanced variability of aboveground vegetation characteristics considerably improves the simulated variability of evaporation and near-surface soil moisture. These improvements are connected to a framework that describes how the implemented vegetation variability influences internal model interactions between vegetation, soil moisture, and evaporation.

Chapter 3 evaluates how climate-controlled root zone parameters influence water flux simulations with the land surface model HTESSEL. To this aim catchment scale root zone storage capacity S_r (mm), defined as the maximum volume of subsurface moisture that can be accessed by the vegetation roots, is estimated using the memory method. In this method S_r is derived from soil water deficits, reflecting the ability of vegetation to adapt to the local climate conditions by sizing their roots in such a way to guarantee continuous access to water, keeping memory of past water deficit conditions. Climate-controlled S_r is estimated with the memory method for 15 catchments in Australia to adequately represent the spatial variability of the vegetation roots. These estimates are integrated into HTESSEL, replacing the static root representation based on soil types and uniform soil depth. The results of offline model simulations show that climate-controlled S_r representation significantly improves the timing of modeled discharge in the study regions. This suggests that a climate-controlled representation of the model S_r has potential for improving water flux simulations by land surface models in a global

context.

Chapter 4 presents the influence of irrigation on the estimation of S_r with the memory method. The memory method S_r is derived from the seasonal patterns of root zone water input and output. Besides precipitation as input, irrigation supplies additional water to the root zone in irrigated agricultural fields. However, the influence of irrigation on the memory method S_r estimates has not been assessed previously. In this study two methods based on different globally available irrigation datasets are developed to account for irrigation in the memory method for estimating S_r. The S_r estimates from these two methods are compared to a case without considering irrigation for a large sample of catchments globally. The results show, for the first time, that irrigation considerably reduces S_r in regions with extensive irrigation, highlighting the relevance of irrigation for adequately estimating ecosystem scale S_r.

Chapter 5 investigates the influence of climate, landscape, and vegetation variables on S_r globally. So far, there is limited insight on the controls of global-scale root development and their spatial variation. A random forest model is used to predict S_r as estimated with the memory method based on 21 variables for a large sample of catchments globally. The results indicate that hydro-climatic variables are the dominant, but spatially varying, driver of ecosystem scale S_r, while landscape and vegetation play a minor role. Based on the importance of the various drivers, a reduced parsimonious model using four variables is used to predict S_r on a global scale. These predictions largely resemble other global estimates of root characteristics based on more complex methods and datasets. This indicates that the here developed parsimonious model to estimate global scale S_r based on four simple globally available variables adequately represents the spatial variability of S_r globally. Together with the results from Chapter 2, it can be concluded that integration of these estimates into large scale hydrological and land surface models has potential to improve model water fluxes.

The findings of this dissertation directly contribute to the large scale hydrological and climate model communities by providing methods to adequately represent spatial and temporal vegetation variability. The results demonstrate the potential of these methods to improve modeled water fluxes by large scale hydrological and land surface models, with major implications for the accuracy of hydrological and climate predictions. This dissertation lays the foundation for future research aimed at further improving the realism of model vegetation variability.

SAMENVATTING

Vegetatie beïnvloedt de verdamping op land door water vanuit de ondergrond te verplaatsen naar de atmosfeer via het opnemen van water door wortels. De hoeveelheid en timing van deze waterflux hangt af van de bovengrondse (bijv. de hoeveelheid bladeren) en ondergrondse (bijv. de omvang van wortels) kenmerken van de vegetatie. Hoewel deze vegetatiekenmerken sterk variëren zowel in ruimte als in tijd, ontbreekt het aan een adequate representatie van deze vegetatievariabiliteit in grootschalige hydrologische en landoppervlakte modellen. Dit leidt tot tekortkomingen in het weergeven van de bijbehorende variabiliteit in gemodelleerde water- en energietoestanden en -fluxen. Dit introduceert onzekerheden in toekomstige voorspellingen van de hydrologische cyclus, inclusief hydrologische extremen zoals droogtes en overstromingen. Om dit probleem aan te pakken, is het doel van dit onderzoek om realistischere modelrepresentaties van ruimtelijke en temporele vegetatievariabiliteit te ontwikkelen, en hun potentieel te verkennen voor het verbeteren van gemodelleerde waterfluxen in grootschalige hydrologische en landoppervlakte modellen.

Hoofdstuk 2 richt zich op modelrepresentaties van ruimtelijke en temporele variabiliteit van bovengrondse vegetatiekenmerken op basis van remote sensing gegevens van satellieten. Interjaarlijkse variabiliteit van landbedekking en bladoppervlakte-index (*leaf area index*; LAI) uit de nieuwste wereldwijde remote sensing datasets worden geïntegreerd in het landoppervlakte model *Hydrology Tiled ECMWF Scheme for Surface Exchanges over Land* (HTESSEL). Daarnaast worden datasets van LAI en de fractie van groene vegetatiebedekking gebruikt om een ruimtelijk en temporeel variërende modelparameterisatie van de effectieve vegetatiebedekking te ontwikkelen en te integreren. De effecten van deze drie implementaties op gesimuleerde hydrologie worden geëvalueerd met behulp van offline (alleen land) modelsimulaties. De resultaten laten zien dat de verbeterde variabiliteit van bovengrondse vegetatiekenmerken de gesimuleerde variabiliteit van verdamping en vochtgehalte in de bovenste bodemlagen aanzienlijk verbetert. Deze verbeteringen zijn gekoppeld aan een kader dat beschrijft hoe de geïmplementeerde vegetatievariabiliteit de interne modelinteracties tussen vegetatie, bodemvocht en verdamping beïnvloedt.

Hoofdstuk 3 evalueert hoe klimaat-gereguleerde wortelzoneparameters simulaties van water fluxen beïnvloeden in het landoppervlakte model HTESSEL. Daartoe wordt de opslagcapaciteit van de wortelzone op schaal van een stroomgebied (*root zone storage capacity*) S_r (mm), gedefinieerd als het maximale volume van ondergronds vocht dat door de wortels van de vegetatie kan worden bereikt, geschat met de *memory method*. In deze methode wordt S_r afgeleid van bodemvochttekorten. Dit weerspiegelt het vermogen van vegetatie om zich aan te passen aan de lokale klimaatomstandigheden door hun wortels zodanig te dimensioneren dat ze continu toegang tot water garanderen, door het 'herinneren' van watertekorten uit het verleden. Klimaat-gereguleerde S_r wordt met de *memory method* geschat voor 15 stroomgebieden in Australië om de ruimtelijke varia-

127

biliteit van de wortels van vegetatie adequaat te weergeven. Deze schattingen worden geïntegreerd in HTESSEL, waarbij de statische wortelrepresentatie op basis van bodemtypen en uniforme bodemdiepte wordt vervangen. De resultaten van offline modelsimulaties tonen aan dat de representatie van klimaat-gereguleerde S_r de timing van gemodelleerde rivierafvoer in de onderzoeksgebieden aanzienlijk verbetert. Dit suggereert dat een klimaat-gereguleerde modelrepresentatie van S_r potentieel heeft om waterflux-simulaties door landoppervlakte modellen in een mondiale context te verbeteren.

Hoofdstuk 4 presenteert de invloed van irrigatie op de schatting van S_r met de *memory method*. De *memory method* S_r is gebaseerd op de seizoenspatronen van de watertoevoer en -afvoer in de wortelzone. Naast neerslag als toevoer, levert irrigatie extra water aan de wortelzone in geïrrigeerde landbouwvelden. Echter, de invloed van irrigatie op de schattingen van S_r met de *memory method* is nog niet eerder beoordeeld. In deze studie worden twee methoden ontwikkeld, gebaseerd op verschillende wereldwijd beschikbare irrigatiedatasets, om rekening te houden met irrigatie in de *memory method* voor het schatten van S_r. De S_r-schattingen van deze twee methoden worden vergeleken met een situatie zonder irrigatie voor een groot aantal stroomgebieden wereldwijd. De resultaten laten voor het eerst zien dat irrigatie S_r aanzienlijk vermindert in regio's met uitgebreide irrigatie, wat de relevantie van irrigatie benadrukt voor het adequaat schatten van S_r op ecosysteemniveau.

Hoofdstuk 5 onderzoekt de invloed van klimaat-, landschap- en vegetatievariabelen op S_r wereldwijd. Tot nu toe is er beperkt inzicht in de factoren die de ontwikkeling van wortels op mondiale schaal beïnvloeden en hoe deze factoren ruimtelijke variëren. Een *random forest* model wordt gebruikt om S_r te voorspellen zoals geschat met de *memory method*, gebaseerd op 21 variabelen voor een groot aantal stroomgebieden wereldwijd. De resultaten geven aan dat hydro-klimatologische variabelen de dominante, maar ruimtelijk variërende, drijfveer zijn van S_r op ecosysteemniveau, terwijl landschap en vegetatie een ondergeschikte rol spelen. Op basis van het belang van de verschillende drijfveren wordt een gereduceerd, eenvoudig model met vier variabelen gebruikt om S_r op mondiale schaal te voorspellen. Deze voorspellingen vertonen veel gelijkenis met andere mondiale schattingen van wortelkenmerken die gebaseerd zijn op complexere methoden en datasets. Dit geeft aan dat het in deze studie ontwikkelde eenvoudige model om S_r op mondiale schaal te schatten, gebaseerd op vier eenvoudige en wereldwijd beschikbare variabelen, de ruimtelijke variabiliteit van S_r wereldwijd adequaat weergeeft. Samen met de resultaten uit Hoofdstuk 2 kan worden geconcludeerd dat integratie van deze schattingen in grootschalige hydrologische en landoppervlakte modellen potentieel heeft om waterfluxen in modellen te verbeteren.

De bevindingen van dit proefschrift dragen direct bij aan de grootschalige hydrologische en klimaatmodellen gemeenschappen door methoden te bieden om ruimtelijke en temporele vegetatievariabiliteit adequaat weer te geven. De resultaten tonen het potentieel van deze methoden aan om gemodelleerde waterfluxen te verbeteren in grootschalige hydrologische en landoppervlakte modellen, wat grote gevolgen heeft voor de nauwkeurigheid van hydrologische en klimaatvoorspellingen. Dit proefschrift legt de basis voor toekomstig onderzoek dat gericht is op het verder verbeteren van de realiteit van vegetatievariabiliteit in modellen.

ACKNOWLEDGEMENTS

This PhD journey has brought me much more than I initially expected. More people have contributed to this than I can thank here. First of all, there are people who are inextricably linked to this research, who made it possible for me to learn so much over the past years.

Ruud and Markus, thank you for giving me the opportunity to start this PhD trajectory, and for your endless support, guidance and advice so that I could also successfully finish it. Ruud, your critical view on both research and non-research topics helped me to develop my own critical thinking skills. Our meetings were always highly productive, thanks to your ability to pinpoint essential points and guide me back on track when I felt lost in my work. Moreover, your kindness and calmness have been of great support to me throughout this journey. Markus, your enthusiasm for hydrology is contagious, it has made me excited about everything from waterfalls and melting snow to preferential flow paths. This enthusiasm always led to (too) many ideas, which challenged me to think critically about the research direction I wanted to take. Besides, your ability to recognize how your PhD candidates are actually doing is extremely valuable and admirable.

Andrea, grazie mille per la tua supervisione. Thank you for welcoming me at CNR and for introducing me in the CONFESS project and the EC-Earth community. These opportunities allowed me to expand my knowledge of Earth system modeling, collaborative work, and, of course, Italian cuisine. Additionally, your expertise in land surface modeling and your insightful, and critical feedback have elevated the quality of my work to a higher level.

I would also like to acknowledge all my coauthors for your expertise, input and feedback. Furthermore, I thank my committee members for your time and dedication to my dissertation, and I look forward to our discussions during the defence.

In particular, I owe a special note of thanks to all my PhD and non-PhD colleagues for sharing experiences, knowledge, and providing endless support from various locations: from office 4.88 to the rest of the watermanagement fourth floor, and two staircases down to the second floor; from TU Delft to universities of Wageningen, Utrecht, Amsterdam, and Nijmegen; and from the Netherlands, to Italy, Sweden and Canada. You made my workdays enjoyable by sharing coffee, cakes, bad jokes, and both laughter and tears.

Lastly, a special thanks to all those close to me who have no idea about the details of my research. Your presence allowed me to disconnect outside of working hours, to put my work into perspective and, most importantly, to have fun.

Curriculum vitæ

Fransje van **Oorschot**

04-09-1996	Born in Roosendaal, the Netherlands.

Education

2020 – 2024	PhD Water Resources Delft University of Technology, Delft, the Netherlands
2017 – 2020	MSc Civil Engineering, Watermanagement Delft University of Technology, Delft, the Netherlands
2014 – 2017	BSc Civil Engineering Delft University of Technology, Delft, the Netherlands

EXPERIENCE

2020 – 2024	PhD Water Resources
	Delft University of Technology, Delft, the Netherlands
2021 – 2023	Researcher in the CONFESS project
	National Research Council of Italy, Bologna, Italy
2019	MSc Thesis Researcher
	KNMI, De Bilt, the Netherlands
2018	Intern
	Tauw, Utrecht, the Netherlands

ACADEMIC ROLES

2021 – 2022	Board member of Watermanagement PhD council
2021 – 2023	Board member and chair of the Dutch branch of the Young Hydrologic Society (YHS-NL)

LIST OF PUBLICATIONS

4. **van Oorschot, F.**, Hrachowitz, M., Viering, T., Alessandri, A., and van der Ent, R. J.: *Global patterns in vegetation accessible subsurface water storage emerge from spatially varying importance of individual drivers,* Environmental Research Letters, in review.

3. **van Oorschot, F.**, van der Ent, R. J., and Alessandri, A., Hrachowitz, M.: *Influence of irrigation on root zone storage capacity estimation,* Hydrol. Earth Syst. Sci., 28, 2313–2328, 2024.

2. **van Oorschot, F.**, van der Ent, R. J., Hrachowitz, M., Di Carlo, E., Catalano, F., Boussetta, S., Balsamo, G., and Alessandri, A.: *Interannual land cover and vegetation variability based on remote sensing data in the HTESSEL land surface model: implementation and effects on simulated water dynamics,* Earth Syst. Dynam., 14, 1239–1259, 2023.

1. **van Oorschot, F.**, van der Ent, R. J., Hrachowitz, M., and Alessandri, A.: *Climate-controlled root zone parameters show potential to improve water flux simulations by land surface models,* Earth Syst. Dynam., 12, 725–743, 2021.